2013

A THREE-DIMENSIONAL QUANTITATIVE UNDERSTANDING OF SHORT FATIGUE CRACK GROWTH IN HIGH STRENGTH ALUMINUM ALLOYS

Wei Wen
University of Kentucky, ustbwenwei@hotmail.com

A THREE-DIMENSIONAL QUANTITATIVE UNDERSTANDING OF SHORT
FATIGUE CRACK GROWTH IN HIGH STRENGTH ALUMINUM ALLOYS

DISSERTATION

A dissertation submitted in partial fulfillment of the requirements for the degree of
Doctor of Philosophy in the College of Engineering at the University of Kentucky

By

Wei Wen

Lexington, Kentucky

Director: Dr. Tongguang Zhai, Associate Professor of Materials Engineering

Lexington, Kentucky

2013

ABSTRACT OF DISSERTATION

A THREE-DIMENSIONAL QUANTITATIVE UNDERSTANDING OF SHORT
FATIGUE CRACK GROWTH IN HIGH STRENGTH ALUMINUM ALLOYS

The behaviors of short fatigue crack (SFC) propagation through grain boundaries (GBs) were monitored during high cycle fatigue in an Al-Li alloy AA8090. The growth behaviors of SFCs were found to be mainly controlled by the twist components (α) of crack plane deflection across each of up to first 20 GBs along the crack path. The crack plane twist at the GB can result in a resistance against SFC growth; therefore SFC propagation preferred to follow a path with minimum α at each GB. In addition to the grain orientation, the tilting of GB could also affect α.

An experiment focusing on quantifying GB-resistance was conducted on an Al-Cu alloy AA2024-T351. With a focused ion beam (FIB) and electron backscatter diffraction (EBSD), the micro-notches were made in front of the selected GBs which had a wide range of α, followed by monitoring the interaction of crack propagation from the notches with the GBs during fatigue. The crack growth rate was observed to decrease at each GB it had passed; and such growth-rate decrease was proportional to α. The resistance of the GB was determined to vary as a Weibull-type function of α.

Based on these discoveries, a microstructure-based 3-D model was developed to quantify the SFC growth in high-strength Al alloys, allowing the prediction of crack front advancement in 3-D and the quantification of growth rate along the crack front. The simulation results yielded a good agreement with the experimental results about the SFC growth rate on the surface of the AA8090 Al alloy. The model was also used to predict the life of SFC growth statistically in different textures, showing potential application to texture design of alloys.

Fatigue crack initiation at constituent particles (β-phase) was preliminarily studied in the AA2024-T351 Al alloy. Cross-sectioning with the FIB revealed that the 3-D geometry, especially the thickness, of fractured constituent particles (β-phase) was the key factor controlling the driving force for micro-crack growth. The resistance to micro-crack growth, mainly associated with crack plane twist at the particle/matrix interface, also

influenced the growth behaviors of the micro-cracks at the particles on the surface.

Wei Wen
05/01/2013

A THREE-DIMENSIONAL QUANTITATIVE UNDERSTANDING OF SHORT
FATIGUE CRACK GROWTH IN HIGH STRENGTH ALUMINUM ALLOYS

By

Wei Wen

Dr. Tongguang Zhai
_____
Director of Dissertation

Dr. Fuqian Yang
_____
Director of Graduate Studies

_____

ACKNOWLEDGMENTS

TABLE OF CONTENTS

LIST OF TABLES

LIST OF FIGURES

Chapter 1 Introduction

The word fatigue, originated from the Latin expression, *fatigare*, which means 'to tire', is commonly associated with physical and mental weariness in people. Since Industrial Revolution in 19th century, it has become a widely accepted engineering terminology standing for the damage and failure of materials under cyclic loads [1]. In a narrow sense, fatigue of materials means the damage and fracture due to cyclic loading, while in a general sense it comprises the delayed damage and fracture under cyclic loads and different environment conditions [2]. In 1964, a descriptive definition of fatigue was given in the report entitled "General Principles for Fatigue Testing of Metals" by The International Organization for Standardizations in Geneva. The term of fatigue was defined as "applies to change in properties which can occur in a metallic material due to the repeated application of stresses or strains, though usually this term applies specially to those changes which lead to cracking or failure".

Fatigue of materials and component is taking place almost at every corner in engineering field and industries every day, and is always associated with loss of capital and even human lives. It has been estimated that the cost directly caused by fatigue failure and corrosion failure reached $276 billion, ~3.1% of GDP of US in 1998 [3, 4]. This number was estimated to be over $1 trillion in 2012 [5]. Therefore, since people started to realize the importance of fatigue damage, it has drawn numerous interests of research on fatigue of materials.

1.1 History of the Research on Fatigue

Although fatigue damage of engineering materials and structures had first been noticed and recorded in early 19th century, the interest in the study of fatigue began to expand until 1850s with the rise of industrial revolution [6]. At the beginning, fatigue failures were frequently observed in pumps, steam engines and locomotives, and it was considered merely as an engineering phenomenon at that time. A new understanding in

fatigue damage was then explored through systematic fatigue tests by Wöhler [7]. His studies covered cyclic bending, torsion and axial loading on railroad axles, leading to the characterization of fatigue behavior in terms of stress amplitude-life (S-N) curve and to the concept of fatigue "endurance limit". Like Wöhler, many other researchers conducted similar fatigue tests and research on different materials, but the interpretation of fatigue mechanism in this period was based on a so-called recrystallization theory [8] which was laid to rest by pioneering work of Ewing et al in early 1900s. Ewing *et al.* [9] carried out microscopic investigations and found that during cyclic loading the slip bands formed on the sample surface, and further developed into "extrusions" and "intrusions" which resulted in the nucleation of fatigue cracks. With the development of fracture mechanics concepts, a large number of quantitative models were proposed and used to analyze the experimentally observed fatigue crack growth behavior in engineering materials around 1950s. Irwin [10] proposed the concept of linear elastic fracture mechanics (LEFM) approach to characterize the amplitude of the stress singularity ahead of a crack with the stress intensity factor, *K*. Later on, Paris *et al.'s* [11] suggested that the increment of fatigue crack advance per loading cycle, da/dN, can be quantified by the range of stress intensity factor, ΔK, during constant amplitude cyclic loading. With the application of fracture mechanics concepts to fatigue failure, increasingly more attention was paid to the mechanism of subcritical crack growth. It was noticed that the stress intensity factor range could be altered by the history of crack advance. In 1970s, Elber [12, 13] initialized the concept of crack closure during fatigue crack growth. Plasticity-induced crack closure mechanism was first proposed, followed by other crack closure mechanisms, such as fracture surface oxidation induced [14], fluid induced [15] and roughness induced [16]. The crack closure effect, attributed as an extrinsic factor, had been utilized to explain the influence of loading condition (e.g. load ration, overloading) on crack growth rate for a long period since then. However, the discrepancies of the opening/closure loads inferred from compliance measurements could vary significantly between different methods or

laboratories [17-20]. In 2000s, a unified approach considering K_{max} and ΔK as the two required parameters in controlling fatigue crack growth was proposed by Kujawski and Sadananda et al [18-23]. It develops the overall crack rate prediction methodology regarding load ratio effects for both long- and short-crack growth behavior.

With the development of microscopy techniques and increasingly more interests in the mechanism of early fatigue crack growth, many experiments and research targeting the short crack regime have been carried out in the last four decades. It was first identified by Pearson in 1975 that short fatigue crack demonstrated an abnormal growth behavior, compared with long cracks, making the conventional LEFM break down in quantifying short fatigue crack growth [24]. Unlike the long cracks, a short fatigue crack is very sensitive to local microstructure, usually deflects at a GB or phase boundary, grows with a scattering growth rate, forms an irregular crack-front and so forth. Although the present knowledge about short fatigue cracks has been greatly enriched, many details of crack nucleation and short crack propagation mechanism are far from being clearly understood. The development of a reliable quantitative model for short fatigue crack initiation and propagation remains a challenging task. Insufficient knowledge regarding the crack behavior in the early stage not only severely affects the development of design methodology for large structural components on the basis of experimental data gathered from smaller-sized laboratory test specimens, but also obstacles the design of new generation engineering alloys.

1.2 Fatigue Properties of Materials

Fatigue is a process of damage accumulation which starts at the scale of the crystal lattice and ends up to the scale of structural component. Theoretically, the fatigue process consists of cyclic slip, crack initiation, short crack growth, long crack growth and final failure, as shown in Figure 1.1 [2]. Crack nucleation usually takes place along the slip bands on surface or subsurface defect due to the less material constraint. In the early

stage of fatigue crack growth, the sizes of the cracks are at the same scale of one or a few grains. Most of them stop growing upon encountering some obstacles, such as grain/phase boundary and large particle, but one or several cracks can developed into long one. In the long crack regime, the crack grows steadily until entering into the final growth regime where the growth is accelerated to a much faster speed, followed by the final failure. Generally, the first three phases, i.e. cyclic slip, crack initiation and short crack growth, are referred to as crack initiation period, and the long crack growth is defined as crack growth period. In engineering field, fatigue life, which is defined as the total number of loading cycles spent on from initiating a fatigue crack to crack propagating to the final crack size, is one of the most important fatigue properties of an engineering material [1].

Differentiated by fatigue life and loading condition, there are two types of fatigue processes, namely, low-cycle fatigue (LCF) and high-cycle fatigue (HCF), which show different behaviors in crack initiation and propagation [6]. LCF is the fatigue at high stress amplitudes, typically over the yield strength, in which the cycle loading is always accompanied by elasto-plastic deformation in the fatigue material. Commonly, the fatigue in which the cycle number to form a visible crack or to final failure is less than 10^4 or 5×10^4 is categorized as LCF. Unlikely, HCF is more related to elastic behavior of the material on a macro scale, in which the applied cyclic stress is just above the fatigue limit, resulting in the fatigue life being up to 10^5 cycles or more. The evaluation of fatigue life generally has two approaches, i.e. total-life approach and damage-tolerant approach.

1.2.1 Total-life Approach

The total-life approach, usually called fatigue limit approach and expressed by S-N curve, adapts the assumption that the materials are flawless before fatigue. The fatigue life covers from the very beginning of crack initiation to the visible crack or final failure. Wöhler [7], who carried out experiments on railroad axles and characterized the fatigue

life in terms of nominal stress amplitudes in the 19th century, introduced the S-N curve for the first time in 1860s. The modern method of S-N curve measurement is established in details in ASTM Standards E466-E468 [25]. In a typical S-N curve, the stress amplitude, σ_a, is plotted on a linear scale in the vertical axis, and the fatigue life, N, on a logarithmic scale in the horizontal axis, as demonstrated in Figure 1.2 [6]. Under a stress level, there exists a plateau beyond $\sim 10^6$ fatigue cycles for mild steel and other materials which can be strain hardened during the fatigue testing. Below this plateau level, the specimen may be loaded to an indefinitely number of cycle without failure. This stress amplitude is known as the fatigue limit or endurance limit. It is noteworthy to mention that the fatigue limit is recognized as the threshold below which short cracks will not grow, but not as a threshold for short crack initiation [26]. Also, many materials, such as high strength steels and Al alloys, do not exhibit a stress threshold in high cycle fatigues. For these materials, the stress amplitude continues to decrease with increasing number of cycles. Instead, the fatigue limit for such materials is defined as the stress amplitude at which the sample can stand for at least 10^7 fatigue cycles [1].

1.2.2 Damage-tolerant Approach

Unlike the total-life approach, the damage-tolerant approach assumes that all engineering materials are inherently flawed before fatigue. Then the fatigue life is defined as the number of fatigue cycles spent on the crack to develop from the initial flaw to a certain critical length. Since the short crack (flaw) has already existed in the sample, the damage-tolerant approach deals primarily with the resistance to fatigue crack growth [1].

For most of engineering alloys, the crack growth rate, *da/dN*, under a certain stress level can be given by a plot of *da/dN* against ΔK, as shown in Figure 1.3 [1, 27]. Such a relationship of *da/dN=f(ΔK)*, namely Paris law, can be empirically derived by fitting the linear parts (Paris region) of the plots of most engineering alloys based on the linear elastic fracture mechanics (will be introduced in details later). In the engineering

applications where HCF is adapted in design, the crack growth period, being able to satisfactorily quantified by Paris law or its derivatives, covers a very small portion (10~20%) of total fatigue life, while the crack initiation period occupies up to 90% of the total fatigue life [1]. Since the damage-tolerant approach count with an initial flaw, thus is more conservative compared to total-life approach, and has been widely used in fatigue-critical applications, like aerospace, aviation and nuclear industries.

1.3 Literature Review on High Cycle Fatigue

1.3.1 Fatigue Crack Initiation Mechanism

As mentioned earlier, fatigue process consists of two stages, fatigue crack initiation and fatigue crack growth. The crack initiation is easily affected by the materials surface conditions, such as surface roughness, grain structure, residual stress, and so on. Normally, the crack initiation period dominate the fatigue life of a material under HCF. A large numbers of papers have been published on the mechanism of crack initiation.

Fatigue damage can take place in a polycrystalline material under dynamic loading at stress levels below its yield strength. The plastic deformation usually occurs in the "soft-orientated" grains or at the stress concentrator on the surface of the materials, because the dislocation slip is less constrained by the surrounding materials in the surface than deep inside the material[28]. Such a localized plastic deformation is accommodated by forming slip bands on the sample surface, as indicated in the early studies by Barrett [28]. After the cyclic slip bands extrude out of the sample surface, the slip step forms and this slip is generally irreversible[29, 30]. The slip irreversibility is mainly account for by two main mechanisms [31, 32]. One is that a thin oxide layer is formed on the freshly surface of slip steps in a non-vacuum environment. Such an oxide layer cannot be simply removed from the slip step surface in the reverse part of a load cycle, thus effectively prevents the reversible slip. The other mechanism is that the stain hardening taking place

in slip bands makes it difficult to fully reverse cyclic slip. As a result, extrusions and intrusions (Figure 1.4) may occur when plastic strain becomes more concentrated in localized slip bands. As a consequence of cyclic slip, the permanent slip band (PSB) forms on the sample surface, acting as the precursor of micro-crack imitation [33, 34]. Forsyth [27, 35] reported thin ribbons of the metal (0.1 μm thick and 10 μm long) 'extruded' on the specimen surface from the PSBs in an Al-Cu alloy and acted as a micro-crack initiation site. Crack initiation from a slip band has also been confirmed in pure Cu [35]. Cheng and Laird revealed that crack nucleation occurred preferentially at PSBs with the highest slip offset or the largest strain localization [36]. Metallographic observation showed that fatigue-induced surface changes corresponded to a period of cyclic strain adjustment in which slip saturation and micro-cracking occur [37, 38]. Boyce [39] revealed that thickening of the oxide on the freshly formed surface of the PSBs was the mechanism for crack initiation. PSBs are the nucleation sites of the fatigue cracks on the surface in many ductile materials.

Another surface feature called protrusion has also been found to be responsible for fatigue crack initiation in some materials [33, 40]. It is a macro-PSB with several micrometers in height and tens of micrometers in width. A protrusion may contain several intrusions and extrusions and extend all the way through the cross-section of the specimen.

In addition to the PSBs, fatigue cracks were also found to initiate at other stress concentrators, such as constituent particles, the particle/matrix interfaces, inclusions and pores in the surface or subsurface [37, 41-44]. In the precipitation hardened alloys (such as 2xxx and 7xxx series Al alloys), the precipitation free zones adjacent to the GBs, especially in an overage temper condition commonly act as crack initiation sites [45, 46]. Sometimes, fatigue crack initiation was also found to occur in the matrix where surface roughness could promote crack initiation on the materials surface as well [47]. As a fact, crack initiation is a complex function of many factors including, but not limited to,

materials mechanical properties, strengthening mechanism, loading condition, environmental condition and so forth.

1.3.2 Crack Propagation and Driving Force

As introduced earlier, fatigue crack propagation consists of short fatigue crack propagation and long crack propagation. While the growth of a long crack can be satisfactorily quantified by the existing fracture mechanics theories, the growth behavior of a short crack is still far from being quantitatively understood. For convenient understanding, the growth of long crack will be introduced first in the following paragraphs, followed by the introduction of short crack growth.

1.3.2.1 Long Crack Propagation

Since the concept of stress intensity factor was introduced in 1960s, the fracture mechanics based theories for fatigue crack growth received a significant development. It was found that the crack growth rate, da/dN can be associated with stress intensity factor range, ΔK. Paris and Erdogan [48] suggested that, for a cyclic variation of applied stress field, the stress intensity factor range, ΔK, should determine the rate of fatigue crack growth and act as the driving force for crack growth.

$$\Delta K = K_{max} - K_{min} \tag{1.2}$$

$$K_{max} = Y\sigma_{max}\sqrt{\pi a}, \quad K_{max} = Y\sigma_{max}\sqrt{\pi a} \tag{1.3}$$

$$R = \frac{\sigma_{min}}{\sigma_{max}} = \frac{K_{min}}{K_{max}} \tag{1.4}$$

In the Equation 1.2 and 1.3, K_{max} and K_{min} are the maximum and minimum stress intensity factor during fatigue a fatigue loading cycle, respectively. Y is a geometrical factor that depends on the ratio of crack length a and specimen geometry. The value of Y for most specimen geometry and crack size can be obtained from literatures and fracture

mechanics handbook. σ_{max} and σ_{min} are the maximum and minimum the fatigue stress in cyclic loading cycle, respectively. The ratio of the minimum stress over the maximum stress is defined as the stress ratio R.

Based on Paris' systematic experimental work, it was found that the relation of crack growth rate, da/dN, and crack growth driving force, ΔK, can be quantified through Equation 1.5.

$$\frac{da}{dN} = C(\Delta K)^m \tag{1.5}$$

where C and m are material-based coefficients and depend on microstructure of material, temperature, environment, cyclic loading frequency, waveform, and load ratio, R, etc. Practically, they are experimentally determined by fitting long crack growth curve plotted in logarithm-logarithm scale.

In the case of crack closure, the crack will not propagate when the crack is closed during the compression or unloaded phase, which is more prone to happen in a low stress ratio condition. Therefore, the effective driving force ΔK_{eff} for crack growth is smaller than $K_{max} - K_{min}$, and is amended to be

$$\Delta K_{eff} = K_{max} - K_{Cl} \tag{1.6}$$

where K_{Cl} is the stress intensity factor at crack closure, as demonstrated in Figure 1.5 [12, 13]. The crack closure effect has been utilized to explain the why da/dN decreases quickly when ΔK is approaching threshold, rather than following Paris law relation. It was found that, if the driving force ΔK at the near-threshold region is corrected by $K_{max} - K_{Cl}$, the da/dN vs. $\Delta K(\Delta K_{eff})$ is still able to be quantified by Paris law. Since the crack closure arises as a result of premature contact of the two conjunct crack faces behind the advancing crack tip, thus the crack closure effect is less pronounced as the crack length decreases due to limited crack wake.

The "crack closure" based approach (Equation 1.6) has been widely adopted as a main mechanism responsible for R-ratio effects in metals in the past 30 years, however, it is often found difficult to correlate the crack closure measurements with crack growth behavior consistently [20, 23]. These difficulties mainly arise from that K_{Cl} depends on measurement location and technique, geometry and length of crack, and environmental factor. Sadananda and Kujawski argued that closure effect on fatigue crack growth have been greatly exaggerated, and they suggested a unified approach to handle R-effect in fatigue crack growth [18, 20-23]. In this approach, the driving force for fatigue crack growth is defined by two required parameters, K_{max} and ΔK, as expressed by Equation 1.1.

$$\overline{K} = (K_{max})^{\alpha}(\Delta K^{+})^{1-\alpha} \tag{1.1}$$

where K_{max} is the corresponding maximum value of the applied stress intensity factor, and ΔK^{+} is the positive part of the range of the applied stress intensity factor. The exponent α is a materials-based constant which can be determined by fatigue experiments conducted at least two different loading conditions, as expressed by Equation 1.2.

$$\alpha = \frac{log(\Delta K_1^{+}/\Delta K_2^{+})}{log((1-R_1)/(1-R_2))} \tag{1.2}$$

With a large body of experimental data of fatigue crack growth, the average α (α_{ave}) of many main metallic materials have been obtained so far. For Al alloys tested in ambient environment, α was found to be 0.5 [23], therefore Equation 1.2 for Al alloys is transformed to

$$\overline{K} = (K_{max}\Delta K^{+})^{0.5} \tag{1.3}$$

1.3.2.2 Short Crack Propagation

Short fatigue crack can be defined by several ways, as described in references [1, 27]: "(1) microstructurally short crack: fatigue cracks for which the crack size is comparable to the

10

scale of the characteristic microstructure dimension (e.g. grain size, phase size) short crack; (2) mechanical short crack: cracks with a length comparable to the scale of local plasticity (e.g. small cracks embedded in the plastic zone of a notch or of a length comparable with their own crack tip plastic zones, typically $\leq 10^{-2}$mm in ultrahigh strength materials and ≤ 0.1-1mm in low strength materials); (3) physically short crack: cracks which are simply physically small (e.g. ≤ 0.5-1mm); and (4) environmentally short crack: fatigue cracks which are nominally amenable to linear elastic fracture mechanics analyses, but exhibit apparent anomalies in propagation rates below a certain crack size as a consequence of the dependence of environmental stress corrosion fatigue effects on crack dimensions".

The abnormality of short fatigue crack growth was noticed when LEFM failed to quantify the short crack growth. The abnormality arises due to: (1) the short fatigue crack can propagate with a stress intensity range well below the driving force threshold (ΔK_{th}) below which the long cracks are arrested or grow at a experimentally undetectable rates [49, 50]; (2) the short fatigue crack propagates at a scattering growth rate which is unable to be predicted or quantified by existing Paris law and its derivations [51, 52]; (3) short crack propagates at a higher growth rate than long crack under the same ΔK resulted by far-field loading [41, 49, 53-60].

The behavior of short fatigue crack growth is intimately dominated by their forming mechanism. After being initiated from a PSB or stress concentrator, the crack will initially propagate in a crystallographic mode (i.e. stage I crack) [61], in which the micro-crack will grow along a favorable single slip plane in a single grain. The non-continuity of the microstructure, resulted in by grain/phase boundary, grain orientation, inclusion, constituent particle, etc., plays a significant role in affecting the growth behavior of the short cracks in stage I. The local microstructure can promote non-continuum plastic deformation, leading to rapid growth of the short crack, severe retardation of crack growth, or deflect the crack propagation path. These effects can be

considerable and highly stochastic because of the random of microstructure features. Among different types of microstructures, GB has been recognized as the most major obstacle to short fatigue crack growth [62-68] [69, 70]. It was found that growth of short cracks was impeded by the presence of GBs due to blocking of slip bands ahead of the crack tip by the GBs, containment of the plastic zone within the grain, reorientation and re-initiation of the crack as it propagate across the boundary, or simply cessation of the growth at the boundary. The traditional LEFM theory for long crack is developed based on the condition of homogenous solid continuum, where the intrinsic resistance of local microstructure against crack growth has been treated as an average constant of the material. However, when the crack length decreases down to the scale of microstructure features, such an "intrinsic" resistance of microstructure can not still be dealt with by the traditional LEFM, because the crack propagation mode has changed from multi-slip to single slip in a single grain, where the GB resistance has to be handled extrinsically with a modification of LEFM or elastic-plastic fracture mechanics (EPFM). The factors controlling short crack growth and modeling work will be introduced in the following sections.

1.4 Factors Controlling Early Stage of Fatigue Damage in High Strength Al Alloys
Since 1920s, Al alloys have been widely used in aircraft structural applications, because of their high strength-density ratio, durability, tolerance to damage, and economical efficiency in fabrication, compared with other materials such as steels and polymers. In recent decades, the application of Al alloy has expanded broadly into many other fields, such as automotive industries and construction industries, where fatigue emerges out as a critical issue. It has always been desired, by consumers, to predict the fatigue life of Al components accurately and reliably; and by Al alloy manufacturer, to develop new Al alloys with better strength and fatigue limit based on a deeper understanding of mechanism for fatigue process. Driven by such demands, extensive research work has been carried out, with interest more inclined to mechanism of the initiation and early

growth of the fatigue cracks in the last 30 years. Many factors have been found to influence the initiation and propagation of a short fatigue crack, i.e., the behavior of short fatigue crack is complex function of many variables. They can generally be categorized by the following aspects: (1) microstructural effects, e.g. grain size and geometry, texture, precipitation, second phase particles; (2) geometrical effects, e.g. stress concentration, crack length, depth and aspect ratio; (3) loading condition, e.g. the level, range and ratio and waveform of loading stress; (4) surface effects, e.g. surface roughness, damage or treatment; (5) environmental effects, e.g. vacuum level, humidity, corrosion media and temperature. However, it is still far away from quantitatively understanding the mechanism for early growth of fatigue cracks. Therefore, it is of both academic and industrial interests to study the fatigue behaviors of Al alloys. Among the above factors, the microstructure is most important for the design of a material for the improved fatigue properties, thus the following discussion will focus on the effects of the microstructure and texture.

1.4.1 Effect of Microstructure on Crack Initiation

1.4.1.1 Intermetallic Particles

Constituent intermetallic particles are the most common sites for the naturally occurring fatigue cracks in engineering materials [24, 41, 43, 44, 46, 71, 72], mainly because (1) the particles themselves are already fractured during manufacturing process (e.g. extrusion, rolling), (2) the matrix/particle interface is weak in some alloy systems, (3) the particles act as the stress concentrator due to the stiffness difference between particle and matrix.

The direct observation of particle cracking in Al-Zn alloy AA7075 [71, 73, 74] showed that the fracture of constituent particle happens suddenly within first few cycles during fatigue and the fractography confirms that the fracture is in a cleavage manner. The particle fracture is due to an excessive critical tensile stress. Goodier [75] found that the

tensile stress across spherical particles may reach up to twice of the principal stress in the matrix, assuming the particle had infinite stiffness. The investigation by Patton et al. [76] indicates that most of the fatigue cracks in Al alloy AA7010 are initiated at constituent Al_7Cu_2Fe and Mg_2Si particles whose Young's modulus has been measured to be 2 and 1.3 times of the Al matrix, respectively [77]. Recently, Ingraffea and co-workers [73, 74] conducted a detailed finite element analysis (FEA) on the effect of constituent particle geometry and surrounding micro-texture on the efficiency of fatigue crack initiation in AA7075-T6 alloy. Similar studies were also carried out in 2xxx series Al-Cu alloys, showing the strong effect of particle size, aspect ratio and density in dominating crack initiation [71]. Based on the experimental work, some empirical models were developed to take into account the effect of large particles on the fracture toughness or fatigue life. For example, a model was developed by Van [71] to correlate K_{IC} and particle population (Equation 1.4)

$$K_{IC} = CD^{1/2}f^{-1/6m}$$
(1.4)

where *C* and *m* are material-based constants, *D* is the average particle distance and *f* is the particle volume fraction and K_{IC} is the critical stress intensity factor for mode I crack.

However, these early understandings are obtained mainly based on 2-D observation on the sample surface, ignoring the effect of 3-D geometry of the particle, thus the many abnormal findings (e.g. crack initiation being associated with small particles or even no surface defects) can not be interpreted with them. Recently, with the developed of the characterization techniques, such as EBSD and FIB, preliminary work has been performed on exploring how the particle 3-D geometry and micro-texture affect the fatigue crack initiation [78-80]. Still, the quantitative understand in 3-D on this topic remains unclear.

1.4.1.2 Voids and Pores

Similar to particles, voids and pores in the surface or subsurface acting as the stress concentrators are also potential crack initiation during fatigue[81]. In wrought materials, these defects are formed mainly due to large particles being broken into fragments, while in castings they are basically gas pores or shrinkage pores [82]. When these voids/pores are located in the subsurface or just touching the surface, a significant stress concentration can be yielded around the defect region, thus initiate the fatigue cracks [82].

1.4.1.3 Grain boundaries (GBs)

GBs is also a preferred type of crack initiation sites in Al alloys. Crack initiation at GBs is generally associated with two types of GBs, i.e. GBs normal to the loading axis and GBs with precipitation free zone (PFZ).

Although the occurrence of debonding of GBs during high cycle fatigue has been significantly reduced or even eliminated in most modern materials, the probability of crack inanition at GBs increases with the loading stress level. Sigler et al [37] found that density of crack initiation at GBs was very low in the early stage of fatigue at a low stress level, but increased dramatically with loading cycles at a high stress level in Al alloy AA2024. It was suggested that the local strain caused by the sufficient irreversible slip could open up the microcracks along the GBs. It was found by Srivatsan and co-works [46] that the preferential plastic deformation throughout the favorably orientated grains resulted in a highly localized stress/strain concentration at GB triple junctions, leading to nucleation of microcracks.

Investigation with the aid of TEM showed that crack initiation at GBs is more prone to happen in the materials with PFZ along the GBs [83-86]. In the precipitation hardened Al alloys, occurrence of a PFZ is due to that the formation of second phase at the GBs

consumes supersaturated solution atoms in the vicinity along the GBs. The GBs therefore becomes a weakest link in fatigue process because no hardening precipitates were formed in GB regions close to GBs. In the case of a synergy of PFZ and high stress level, the crack initiation at GBs becomes a predominant mechanism for nucleating fatigue damage. The comparison work by Mulvihill and co-worker [83] demonstrated that the crack initiation invariably took place at GBs in peak-aged Al-Cu alloys at a maximum stress of 80% of yield strength while the crack initiation at GBs were not observed in the natural-aged counterpart samples. The TEM observation confirmed that densely populated θ precipitates were formed along the GBs surrounded by PFZ in peak-aged samples, which weakened the GBs during the fatigue.

1.4.1.4 Micro-texture

Taylor et al studied the effect of texture in dominating crack initiation site in an Al-Li alloy AA8090 [87]. The plastically soft grains, i.e. the ones with high Schmid factors, are likely to become the preferential sites for the crack initiation. The cracks were predominately initiated in grains that had <100> being orientated to the loading axis. Patton et al [76] measured the crystal orientation of the crack-initiation grains in Al alloy AA7010, which showed that the grains exhibiting R-cube texture with respect to the loading axis are more prone to initiate crack by intermetallic rupture.

Similarly, the similar dependence of crack initiation on texture also prevails in other engineering alloys. In steels, the crack nucleation was found to preferably happen in the favored grains. Mineur et al. [88] studied the texture effects over the fatigue behavior of 316L austenitic stainless steel, in which the micro-texture of crack initiation sites was observed with EBSD. Their results indicated a strong effect of texture on the crack initiation. Soft grains (i.e. grains with high Schmid factors) with close-<110> directions were characterized by high crack densities while hard grains (i.e. grains with low Schmid factors) with close-<111> directions by very low crack densities.

Studies on Ni-based superalloys showed that the PSB zones were preferably formed in the near-cubic orientated grains [38, 89-91]. The connection between the tendency of activation of independent slip and the ease of formation of extensive PSB deformation has been explained by the Taylor factor criterion. Recent investigations by Sangid [91, 92] also showed that the micro-texture of neighboring grains surrounding the PSB-initiation one also played an important role in the crack initiation. If a neighboring grain has a low misorientation, i.e., the GB is a low angle GB (LAGB), the PSBs can usually transverse across the GBs into the next grain. In the case that the PSB occurs in one grain of grain-clusters, PSBs can transmission across the GBs along the clusters, since they are connected by LAGBs. As a result, such a grain cluster is considered as a super-grain and represents a preferred site for crack initiation. Oppositely, if the GBs are of high angle, the PSBs will be blocked by the high angle GBs, the dislocations will pile-up against at the GBs, leading to discontinuity of strain gradient at the GBs and thus crack initiation at the GBs [91-93].

1.4.2 Effect of Microstructure on Short Crack Propagation

Microstructural features, such as GBs, grain geometry, grain orientation, constituent particles, inclusions, plays a somewhat minimal part in affecting the growth behavior of long cracks, because their growth behavior is dominated by the average bulk properties and can be satisfactorily quantified by Paris law and its derivatives. However, these microstructure features govern the crack growth in stage I regime.

1.4.2.1 Grain Boundary and Grain Size

Supported by a great number of experiments, the grain boundary, among different microstructure features, has been recognized as the most significant barrier for the short fatigue crack growth [51, 54, 94, 95]. For example, a large portion of the secondary cracks in Al-Li alloy have been observed with their tips being ceased at the GBs. Some of

these crack tips can cross one or two grains before be arrested, indicating that GBs had resistance against the short crack growth and such GB-resistance varied among different GBs [96]. The resistance of GB against crack growth was also proved by Sarioglu's work on fatigue experiments on Al alloy AA2024 [85]. It was found that the crack length in natural-aged samples was determined by the grain size because the crack tips usually stopped at the GBs. It was suggested that the formation of large plastic deformation zone lead to crack retardation until a new crack is formed in the neighboring grains. Taylor and co-workers' [57, 87] investigation indicated that the crack propagation, which was a process of cyclic plasticity and deformation, is relatively easy within the first grain, but the GB can act as a barrier to such cyclic plasticity during fatigue. The GB showed stronger obstacle effect in high cycle fatigue, where many short crack never grow beyond the first grain while any those growing beyond the microstructural size finally developed into long cracks. In addition, the crack growth retardation at GB triple junctions was also observed occasionally in [97, 98].

Since the resistance against the short crack growth mainly comes from the GBs, thus the grain size also play an important role in controlling short crack growth because it represents the density of GBs. It is considered that smaller grains should render a larger resistance to crack growth because of higher density of GB. The plastic strain generated by the pre-mature cracks is more prone to be blocked by the GBs. Zurek [99] et al, however, also found that the surface short fatigue crack grew markedly slower in coarse grained samples than their fine grained counterparts. Zurek attributed the decrease in growth rates with increasing grains size to grain-size-dependent plasticity-induced closure. So far, the grain size effect on short crack growth remains unclear and under debates.

1.4.2.2 Micro-texture

Crystallographic orientation (micro-texture) of grains influences the growth behavior of stage I crack within an individual grain. In stage I, the short fatigue cracks prefer to propagate following particular crystallographic planes within individual grains, especially in planar slip type alloys which either are hardened by shareable precipitations or have high stacking fault energy. In these materials, the texture has a significant influence of the crack plane orientation, Schimd factor and crack growth driving force, thus affect the crack growth rate considerably.

In typical precipitation hardened alloys, like Al-Li alloy 8090, Al-Si-Mg alloy 6061, the research work discovered that the fatigue cracking along {111} in vacuum and moist air[95, 100-102]. The EBSD results indicated that the fatigue crack propagation was progressed by microcracking nearly parallel to {111} for over 80% of the facets analyzed in both recrystallized and unrecrystallized grains. The fatigue facets being parallel to {111} planes were also observed in an unrecrystallized Al alloy plate with copper texture in a vacuum test condition. Similar observations were reported in Goss textured grains in recrystallized sheet and in recrystallized region with more random crystallographic orientation. The research by Wu et al indicates that the directionality of the fatigue fracture behavior is related to the strong {110}<112> texture [103].

More importantly, the micro-texture exhibits a considerable influence on controlling short crack path and the resistance of GB to crack growth. When a crack tip approaches a GB, it tends to reorient itself in the neighboring grain to progress by the localized shear mechanism. The extent of crack deflection at a GB depends on the grain orientation in a global coordinate system and relative orientation of the most favorable slip system in the adjacent grains. Traditionally, the misorientation of the two adjoining grains was considered as the key factor controlling growth behavior of a crack passing a GB. It was believed that large misorientation (large angle GB) yielded higher resistance against

crack growth while small misorientation (low angle GB) exhibits minimum effect. This hypothesis was later adopted in modeling the process of either slip band blocking or slip blocking by a GB. By introducing a misorientation-based function $K(\Phi)$ with respect to resolved shear stress in cracked grain and its neighboring grain in front of the crack tip, Chan and Lankford [104] reconsidered the crack tip plastic strain range and modified the LEFM equation to accommodate the GB effect. Wu et al. developed a mechanical model for transgranular fatigue crack growth in high textured materials. In their model, the effect of texture on fatigue crack growth rate is related via a geometric factor $cos^2\varphi$ (φ defined as the angle between the load axis and the normal of the favorable slip plane). The model predicts that fatigue crack growth will grow slower in many textured materials than texture free materials.

In recently years, the development of advanced characterization techniques allowed a deeper understanding of the GB effect on crack growth, especially providing a 3-D perspective. Zhai et al, with EBSD and acoustic microscope, revealed that the twist and tile angles of the crack plane deflection at a GB are the key factors controlling the path and growth rate of a short crack in Al-Li alloy AA8090. As shown in Figure 1.6 is the schematic diagram of his model for crack propagation through a GB from grain 1 into the adjacent grain 2 along the favorable slip plane. α=$|\psi_1 - \psi_2|$, defined as the angle between the two intersecting lines (**ab** and **ac**) of the two favored slip planes on the GB plane, represents the major resistance to crack propagation from one grain to another because the wedge shaped area (**abc**) described by α on the GB plane has to be fractured for the crack to pass through the GB. The larger the α, the higher the resistance from the GB. The angle between the intersection lines of the two favored slip planes on the sample surface is $\beta = |\theta_2 - \theta_1|$ which can also contribute to the total resistance of the GB to crack growth by reducing the driving force at the crack tip. For a short crack to cross the GB from grain 1 into grain 2, it has to overcome the resistance from the GB. As a result, at the GB, the crack will select the slip plane that offers the minimum α angle, i.e.

minimum resistance, among the four slip planes in grain 2. Among all the microstructural factors such as α, β, and Schmidt factor, α is the most dominant one that control the short crack growth [95, 105]. This minimum-α criterion has been verified in AA8090 Al-Li alloys [95, 106], Ni-based alloys [107-109], Ti-based alloys [110-112] and zinc [113], etc.

With the focused ion beam (FIB), Schaef and Marx [107-109] studied the interaction of short fatigue crack with GB in 3-D in Ni-based super alloy. Utilizing a technique combining synchrotron imaging and phase-contrast X-ray tomography, Ludwig et al [110-112] was able to observe the crack front evolution in a Ti-based alloy in-site, and obtain the information of grain geometry and crystal orientation simultaneously. Takahashi et al [102] characterized the interaction behavior of GB and the short crack emanated from micro-notches, with the aid of FIB and TEM. All of these recent works not only further confirmed Zhai's model with the 3-D point of view, but enriched the knowledge about the GB effects. However, many more details, especially the quantitative understanding of the mechanism has not achieved yet.

1.4.2.3 Constituent Particles and Voids

Compared to GB and texture, constituent particles and voids play a relatively minor role in short crack growth. Debartolo and co-workers [44] observed that the interaction of the crack tip and constituent particles depended on the state of the particle. When the particles were debonded with matrix or already fractured during deformation process, the fatigue crack were prone to propagate through them, which sped up the crack growth rate effectively. When the particles were well bonded with the matrix, the crack tended to deviate from straight path to avoid the particle, slowing down the crack growth rate.

The fatigue studies of the high strength Al alloy and casting alloys showed that the voids acted equivalently as the second-phase particles which had "zero" stiffness or been fully debonded with matrix [46]. The experiments on Al alloy AA2524 revealed that the strain

in the region surrounding the voids was greater than that in the matrix, facilitating a gradual increase of both the size and relatively volume fraction of voids during fatigue damage. Also, the coalescence of micro voids to form void sheets were observed in the materials during fatigue [114, 115].

1.4.3 Previous Attempts to Quantify Short Crack Growth

Several models have been developed in an attempt to quantify the process of short fatigue crack growth [116-118]. Most of them are based on Bilby, Cottrell and Swinden's theory which describes the crack and the plastic deformation zone in the vicinity of the crack tip as an array of continuously distributed dislocations [119]. The process of either slip band blocking or slip blocking by a GB is considered in these models. The effects of the GB constraint on the size of the crack tip plastic zone and the crack closure stress have also been discussed [120]. However, these models do not directly take into account the local texture and its change across a GB ahead of the crack tip, though Navarro and De los Rio (NR) et al [108, 117, 118, 121, 122] have incorporated the average Sachs factor of the grains along the crack front into their model for short crack growth simulation. Wilkinson adopted the BSC approach and modified NR model, with an attempt to study the effect of macro-texture on short fatigue crack growth in Al-Li alloy [123]. However, these models are 2-D in essential, leading to lack of consideration in the effect of really microstructure, especially the GB geometry and orientation. Recently, Ravichandran and Li [124] have studied the effects of variation in elastic moduli of the grains covered by a short crack on the stress intensity factor (K). Using the weight function technique and numerical analysis, K is calculated and found to vary along the crack front due to the variation of grain orientation. Although with the grain geometry and crack growth in 3-D being considered, they are able to explain the observed changes in the shape of a surface short fatigue crack due to grain orientation, the effect of GBs has not been considered. In a near

isotropic material such as Al, the anisotropic effect due to grain orientation variation is neglectable and GBs become the dominant barriers to crack growth.

Finite element method, especially the crystal plasticity based approach, was also utilized to quantify the plastic strain in front of crack tip and crack advancement [125-128]. Molecular dynamics modeling was adapted to investigate the crack initiation and early growth [90-92]. These approaches, however, are still pre-mature so far, causing conflicting results among different materials system and research group. And also, these approaches currently face the limitation of computation capability of computers, thus is not difficult, even impossible, for statistically study of short fatigue crack growth behavior for design of engineering alloys.

1.5 Rationale and Purpose of the Study

Extensive efforts have been made over the last few decades, attempting to understand the mechanisms of the early stage of fatigue damage in Al alloys, however, the fatigue crack initiation and short crack growth are still far from been understood thoroughly, let alone the microstructurally-based model to quantify the process of the fatigue damage. This raises a huge challenge for the materials scientist and engineers to develop the new generation Al alloys with both enhanced tensile strength and superior fatigue properties.

The purpose of the present research work is mainly to further study the growth behavior of short fatigue crack, especially the interaction of crack tip with GBs, in high strength Al alloys. It is attempted, based on the experimental discoveries, to develop a microstructurally-based numerical model to quantify the short crack behavior, for a more reliable lifetime prediction and design of new engineering alloys. Also, the micro-crack extension from constituent particles into matrix, counted as a part of crack initiation, in high strength Al alloy was reexamined to offer a better understanding of crack initiation behavior, maybe being of value in modifying existing model of fatigue crack initiation.

1.6 Selection of Materials

Fatigue problem is one of the most important concerns in selection and design of materials used in aviation and modern automotive applications. To achieve a superior balance of tensile strength and fatigue properties, as well as formability, precipitation hardened high strength Al alloys (e.g. 2000 series and 7000 series) and medium-high strength Al alloy (e.g. 6000 series) are widely selected as the materials for the key components, such as fuselage, wing, chassis [129]. Al-Cu alloy AA2024 and Al-Li alloy AA8090, being the typical representatives of precipitation hardened high strength Al alloy, were selected as the experimental materials in this study, and their chemical compositions are shown in Table 1.1. These two alloys were selected because they share many similarities with other precipitation hardened high strength Al alloys, thus are appropriate to serve as a platform in understanding this type of alloys. These similarities mainly include:

(1) Similar metallurgical processing. These three types of Al alloys are generally produced through the same key metallurgical processing, e.g. smelting→ingot by direct chill (some 6000 series alloys are produced by continuous casting)→homogenization→thermomechanical processing (hot rolling, cold rolling and associated annealing)→solid solution→quenching→cold working→ageing (natural or artificial ageing).

(2) Similar strengthening mechanism. Precipitation hardening is the most important strengthening mechanism shared commonly by these three types of Al alloys. During the ageing, the alloying elements precipitate to form fine shearable and ordered dispersoids in the matrix (s'-Al_2CuMg phase in 2000 series, β'-Mg_2Si phase, in 6000 series, η-$MgZn_2$ phase and T'-$Mg_{32}(Al,Zn)_{49}$ phase in 7000 series), which effectively resists or even pins the slip of dislocations and minimize grain growth [130].

(3) Similar high tendency of planar slip. To illustrate this point, it is noteworthy to introduce the mechanism of planar slip. Usually, planar slip takes place in pure metals with a low stacking fault energy (SFE), where a full dislocation may reduce its energy by dissociating into a pair of partial dislocations separated by a stacking fault [131, 132]. The dissociation of a full dislocation in a face centered cubic (FCC) crystal can be expressed by

$$\frac{1}{2}[\bar{1}10] = \frac{1}{6}[\bar{1}2\bar{1}] + \frac{1}{6}[\bar{2}11] \qquad (1.5)$$

Thus the move of a full dislocation is replaced by the moves of the two partial ones. As the first partial dislocation slips, it changes the stacking order by producing an anti-phase boundary (APB) which has a very high energy, thus the second partial dislocation will glide on the exactly same lattice plane glided along by the first to restore the stacking order to its proper sequence (i.e. low energy ordering). After both partial dislocations glide through the same lattice plane, it results in the crystal being sheared at the slip plane by an amount equal to the Burgers vector b of the full dislocation. The lower the SFE, the wider the stacking fault between the extended dislocations in the metal, thereby the stronger tendency for planar slip [133].

In pure aluminum, although the dislocations are almost unextended and have a very low tendency for planar slip because of high SFE, the decrease of SFE and the tendency of planar slip can be facilitated by alloying, especially by the presence of large volume fractions of shearable and ordered second-phase precipitates, e.g. in the case of high strength Al alloys [134, 135]. As shown in Figure 1.7, the glide of a unit dislocation through the ordered lattice of a precipitate will result in a disordering in the form of APB. To minimize the APB-associated energy increase, dislocations tend to move in pairs, like a super-dislocation, similar to the extended dislocation [135, 136]. This leads to planar slip along close packed {111} planes and a crystallographic faceted mode of crack extension [137-141].

(4) Similar crack initiation site. In most of these alloys, the fatigue cracks are originated from the constituent particles during high-cycle fatigue. These constituent particles are mainly β-phase ($AlCu_2Fe$) with higher stiffness than matrix and irregular shape [74, 78, 129, 142].

It is apparent that the investigation with AA2024 and AA8090 will enrich the knowledge about the fatigue behavior for the whole family of high strength Al alloys.

1.7 Key Results Obtained

The short fatigue crack behavior in alloy AA8090 was analyzed. It was qualitatively found that the twist angle (α) has a significant effect on determining the crack deflection at a GB and thus the whole crack path. The short crack tended to grow in the alloy following a minimum-α path. In addition to crystallographic orientation, the GB tilting was also found to play a part in determining the GB-resistance via affecting the value of α. A minimum-α map for a vertical micro-crack was calculated to evaluate the resistance to crack growth into a neighboring grain with a random orientation. Some of the results from this part of the work, entitled "*Three-dimensional Effects of Microstructures on Short Fatigue Crack Growth in an Al–Li 8090 Alloy*", has been published in *Philosophy Magazine[143]*.

Based on the qualitative discovery of α effect on short crack growth behavior, a delicate experiment was carried out in alloy AA2024, as an attempt to establish the quantitative relationship of α and GB-resistance. With the aid of FIB and EBSD, short fatigue cracks were successfully initiated within the selected grain and before the selected grain boundaries which had a wide range of α. The initiation and growth of the short cracks, especially their interactions with the GBs, were carefully observed and analyzed. It was found that the GB-resistance is a function of α, and can be fitted by a two-parameter Weibul function. This finding would be the first time to experimentally quantify the GB-resistance in planar slip materials. A part of the results from this work, entitled "*An*

Experimental Quantification of Grain Boundary to Short Fatigue Crack Propagation in 3-D", has been drafted and will be submitted to *Acta Materialia* soon.

With the established relationship of GB-resistance and α, a 3-D microstructurally-based model, which incorporated GB-resistance and modified Paris law, was developed to quantify the short fatigue crack growth in engineering alloys. The baseline model demonstrated its capability in simulating the behavior of short cracks in engineering alloy. The model was further validated by comparing the simulation with the experimental results, which showed a good agreement between the model and the experiments. With this model, the short crack growth in a textured engineering alloy could be statistically predicted, showing potential value for more reliable life prediction and engineering alloy design in terms of texture optimization. The concept and development of the model, entitled "*Quantification of Resistance of Grain Boundaries to Short-Fatigue Crack Growth in Three Dimensions in High-Strength Al Alloys*", has been published in *Metallurgical and Materials Transaction A[106]*. And the part regarding validation and application of the model will be submitted to *Acta Materialia* soon.

As a preliminary study, the extension of micro-crack from constituent particle into matrix, in high cycle fatigue was reexamined with the aid of FIB and EBSD. The traditional 2-D size and aspect ratio of particles were found to be unnecessarily correlated with the crack initiation. Instead, the particle 3-D geometry and surrounding crystallographic orientation played a synergic role in dominating effective crack initiation. This part of work, entitled "*A Study of the Effects of Particle 3-Dimensional Geometry and Micro-texture on Fatigue Crack Initiation Behaviors in an Al-Cu Alloy using Focused Ion Beam and Electron Backscatter Diffraction*", has been recently published in *Materials Science and Engineering A[142]*.

Table 1.1 Chemical composition of Al alloys AA2024 and AA8090 (wt %).

	Si	Fe	Cu	Mn	Mg	Zn	Ti	Cr	Zr	Li	Balan
AA2024	0.5	0.5	3.8-4.9	0.3-0.9	1.2-1.8	0.25	0.15	0.1	0.25	-	Al
AA8090	0.2	0.3	1.0-1.6	0.1	0.6-1.3	0.25	0.1	0.1	0.04-0.16	2.2-2.7	Al
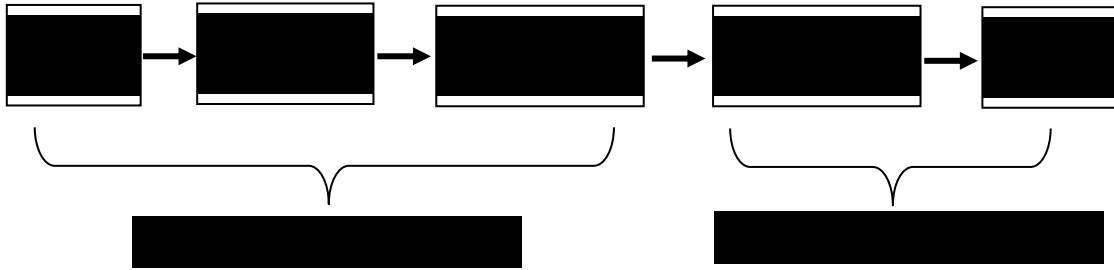
Figure 1.1 Different phases in the fatigue process.
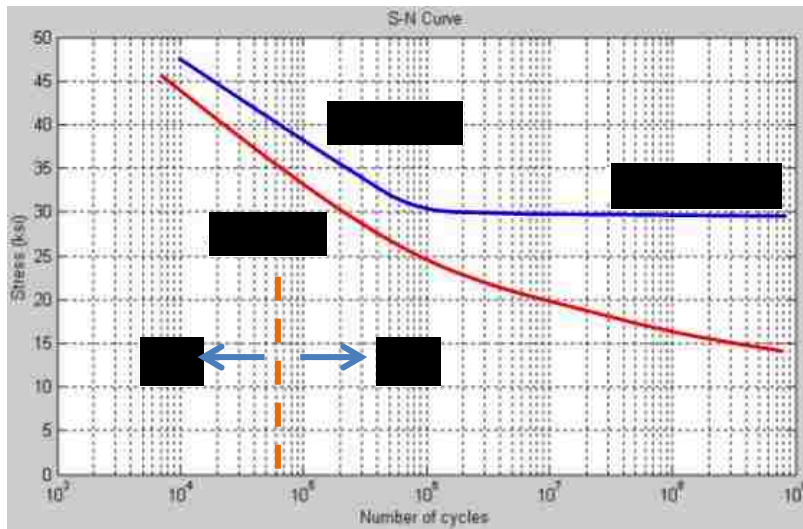
Figure 1.2 Typical S-N curves for materials with and without fatigue limit.
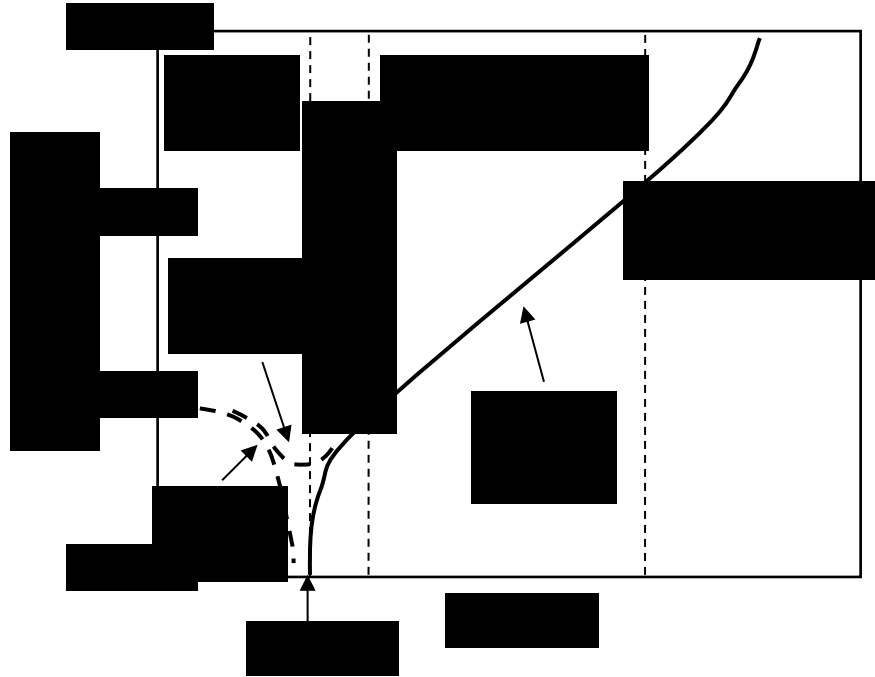
Figure 1.3 Schematic diagram showing a crack growth rate da /dN vs. ΔK curve [1, 8].
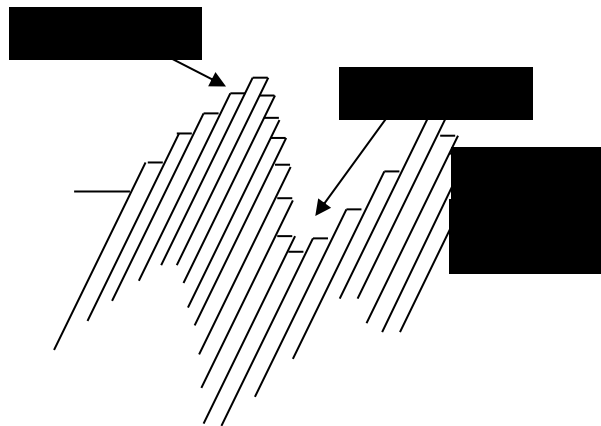
Figure 1.4 Sketch diagram showing geometry of slip at the material surface according to Forsyth [27, 35].
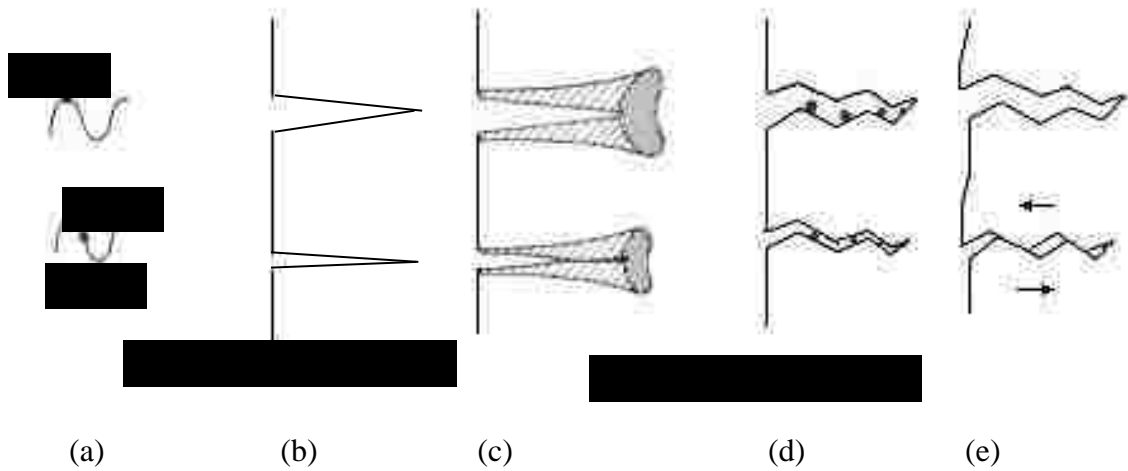
Figure 1.5 (a) Applied stress in a load cycle, (b) crack tip and mechanisms of fatigue crack closure due to (c) plasticity, (d) corrosion debris, and (e) surface roughness [12, 13].
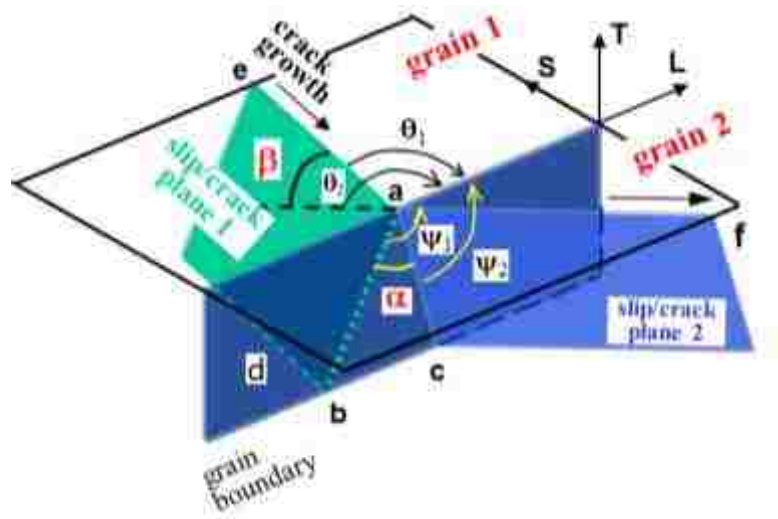
Figure 1.6 Schematic diagram showing a crystallographic mechanism for crack growth along slip plane 1 in grain 1 onto slip plane 2 in grain 2. The crack growth across the GB is controlled by α and β (after [95]). **ad** is the intercept line of crack planes 1 and 2.
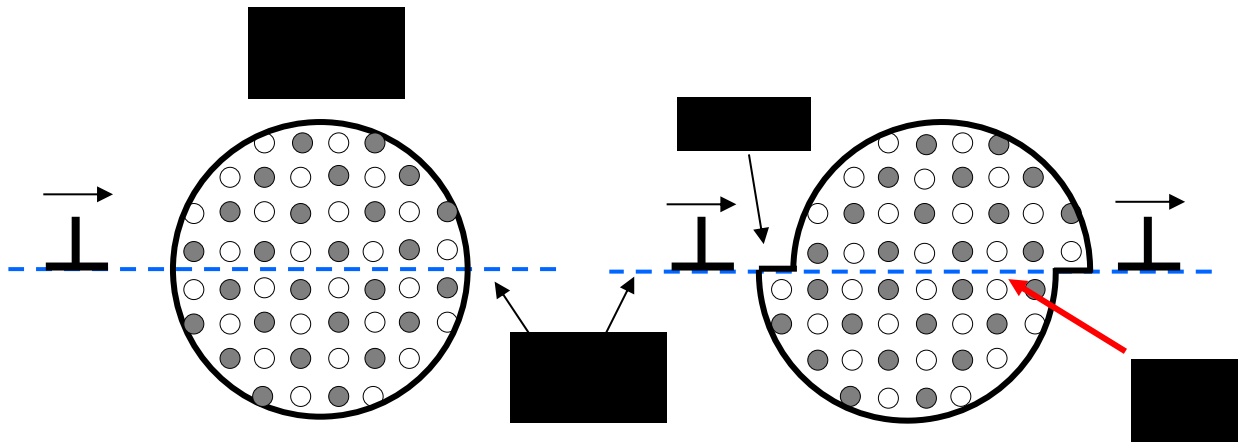
Figure 1.7 Schematic diagrams showing (a) a coherent precipitate sheared by dislocation, forming (b) APB and new interface.

Chapter 2 Experimental Theory and Technologies

In order to investigate the short fatigue crack growth behavior in precipitate hardened high strength Al alloys, a series of tests and characterizations were conducted on Al-Cu alloy (AA2024). Based on the mechanical properties as measured in standard of tensile tests, four-point bend fatigue tests were designed and carried out to study the fatigue initiation and short crack growth behavior, especially the interaction of crack with microstructures. Together with the earlier experimental results of short fatigue crack growth in AA8090, Optical microscope (OM), scanning electron microscope (SEM), electron backscatter diffraction (EBSD), focused ion beam (FIB) were utilized to study the effect of local texture and microstructure on short crack growth in 3-D.

2.1 Mechanical Test

2.1.1 Tensile Test

The dog bone shaped specimens for tensile testing were prepared according to ASTM standard [144], with a gage length of 25.4 mm and width of 6.35 mm (Figure 2.1). The specimens of Al-Cu alloy A2024-T351 were cut along L-direction and T-direction, respectively, on the L-T plane of the as-received plate.   Tensile tests were performed on an Instron 8802 servo-hydraulic testing machine (Figure 2.2) at a constant crosshead speed of 1.2 mm/min at room temperature in air. At least two specimens were tested in each orientation. The specimens of Al-Li alloy AA8090 plate were cut along the L-direction on L-S plane, which has been completed earlier by Zhai [95, 101]. The as measured 0.2% offset yield strength in the tensile curve, $\sigma_{0.2}$, was taken as the tensile yield strength σ_y. The loading forces in the fatigue tests were selected based on tensile properties, especially the tensile yield strength σ_y.

2.1.2 Fatigue Test

In the commonly used four-point bend testing rigs, the geometry, like the support span/load span ratio (L/t), is either 2 or 3, which usually fails to generate a uniform stress distribution in the sample surface under tensile loading. With the variation of L/t ratio, a sample can fail either right over of one of the loading rods in thin a sample or right in the middle of a thick one, leading to inconsistent results. In this research work, a homemade self-aligning four-point bend fatigue testing rig was used to perform the fatigue testing. The fatigue testing was performed in a self-aligning four-point bend whose sample and loading geometries are shown in Figure 2.3 and 2.4 [145]. The optimum test geometry (L/t of 4-5 and t/h of 1.2) for four-point bend fatigue has been established through numerical and experimental approaches [145]. By using this geometry, a uniform tensile stress can be achieved in the sample surface between the two loading rollers, and gives rise to repeatable consistent results. The nominal maximum tensile stress σ_{nom} in the sample surface can be calculated by the beam theory of engineering mechanics,

$$\sigma_{nom} = \frac{3F(L-t)}{wh^2} \tag{2.1}$$

where F is the load applied by one of the two loading rollers, L and t are the support span and load span respectively, w and h are the width and thickness of the specimens. In this research work, the fatigue experiments of AA8090 were conducted earlier by Zhai [95, 101]with the samples geometry of $l \times w \times h$ equal to $36.5 \times 10 \times 4.7$ mm^3, where l, w and h are the specimen length, width and height. The experiments of AA2024 in this work were carried out with specimen geometry of $36.5 \times 7 \times 4.7$ mm^3, The specimen surfaces which were under tensile load during fatigue tests were ground with SiC sand papers gritting from 240 to 1200, mechanically polished with alpha alumina (Al$_2$O$_3$) powder of 1 μm, 0.3 μm and 0.05 μm in size, followed by the final polishing with a silica colloidal suspension before fatigue testing.

The fatigue tests were conducted on an Instron 8802 testing machine (Figure 2.4), with a sinusoid wave form, at 20 Hz, a stress ratio (R=$\sigma_{min}/\sigma_{max}$) of 0.1 and room temperature in air. The tests were interrupted periodically with an interval of 1000~5000 cycles to monitor the crack length and interaction of crack with GBs.

2.2 Characterization

2.2.1 Scanning Electron Microscopy

Scanning electron microscopy (SEM) is a type of electron microscopic techniques to produce high-resolution images of a sample surface by scanning it using a focused electron beam with an high energy of 0.5~30 keV. The high-energy electron beam is collimated by electromagnetic condenser lenses, focused by an objective lens, and scanned across the surface of the sample by electromagnetic deflection coils [146, 147].

When the accelerated incident electrons bombard on the sample surface, a variety of signals can be generated, including secondary electrons (SE), backscattered electrons (BSE), diffracted backscattered electrons (signal used to determine crystal structure and orientation by EBSD system, which will be intruded in more details in the next section), Auger electrons, X-rays, etc (Figure 2.5). The SEs, generated within a few nanometers from the sample surface, are very sensitive to the surface topography, thus is the most used signal. They are detected by a scintillator-photomultiplier device and the consequent signal is transformed into a 2-D intensity distribution that can be viewed as digital image. Being different SEs, the BSEs are generated because of the elastic scattering/reflection of the incident electron beam by the atomic nuclei in the sample surface. The larger the atoms (with a greater atomic number Z), the higher probability of producing an elastic collision due to greater cross-sectional area of the nuclei. Hence, the image in BSE mode qualitatively incorporates composition information of the scanned surface. By means of X-ray energy dispersive spectroscopy (EDS), the characteristic X-rays signal emitted

from the sample can provide more quantitative elemental information [147]. In the present work, all the SE, BSE and EDS were used for the topography observation and chemical composition analysis on SEMs Hitachi S-4300 and S-3200.

2.2.2 Focused Ion Beam

Focused ion beam (FIB) microscope has gained widespread use in fundamental materials studies and technological applications over the recent years because it offers both high-resolution imaging and flexible micromachining in a single platform. The FIB instrument is similar to an SEM, except that the beam that is rastered over the sample is an ion beam rather than an electron beam. By the means of adjusting the parameters, such as beam current and accelerating voltage, an FIB can be used to, but not limited to, obtain high-spatial-resolution images, precisely deposit and micro-machine the sample surface at a scale from submicron to hundreds of microns.

In most commercially available FIB systems, the liquid-metal ion type source (LMIS) is usually used [148]. Among various types of LMISs (such as In, Bi, Sn and Au based source), the Ga-based blunt needle source (Figure 2.6) has been widely used because of its decided advantages in terms of low melting temperature, low volatility, and low vapor pressure [149]. During operation, Ga flows from a reservoir to the needle tip (with an end radius of about 10 μm), where it is extracted by field emission. A large negative potential between the needle and an extraction electrode generates an electric field of magnitude 10^{10} V/m at the needle tip. The balance between the electrostatic forces and the Ga surface tension results in the wetting of the tapered W needle geometry and the formation of a single Taylor cone at the needle tip. For typical emission currents used in FIB microscopes (~2 mA), a cusp forms at the tip of the Taylor cone with a tip radius of approximately 5 nm. Once the Ga^+ ions are extracted from the ion source, they immediately travel through a series of lens which can be simplified as a condenser lens and an objective lens, as shown in Figure 2.6.

When the Ga^+ ions bombard on the sample surface, the kinetic energy of the ions is transferred to other forms of energy or signals through interactions with the sample atoms. As shown in Figure 2.7, the ion-sample interaction generates a series of events, mainly including, but not limited to, ion reflection and backscattering, electron emission, electromagnetic radiation, atomic sputtering, ion emission and sample damage [150, 151]. Among these signals, the emitted electrons, especially the ion-induced secondary elections (ISEs), are collected by the detector for imaging in FIB system. Since ion beams are not as finely focused as electron beams, thus they generally yield a relatively lower resolution. However, the FIB can offer complementary information about sample surface because ISE imaging can deliver stronger channeling contrast from the crystals than SE imaging [149]. Another major application of an FIB is ion beam sputtering which allows the precise local removal or milling of material. When an accelerated Ga^+ ion impinges the target sample, it enters the sample, resulting in the ejection of a sputtered particle (which may be an ion or a neutral atom). The effect zone depth of ion bombardment is controlled by the accelerating voltage. For example, the penetration depth is ~20 nm for 25keV Ga^+ ions. The use of enhanced etching may increase the sputtering rate [150, 152]. Halogen gases, such as Cl_2, I_2, and XeF_2, can be directed to the area of interest. These gases can form a volatile compound with the sputtered material, thus accelerate the sputtering process. In the sample preparation that is by the means of FIB milling, an ion beam assisted chemical vapor deposition is usually used. In this application, a hollow needle is brought to within ~100-200 μm of the target surface, then the suitable gas (e.g. $W(CO)_6$) is injected from the needle tip and absorbed onto the target surface. When the Ga^+ beam is rastered over target region, the ion beam decomposes the gas, leaving a deposited layer of metal (e.g. W) while the by-product (e.g. CO) is extracted through the vacuum system [148, 151].

In this research work, the FIB was used to 1) make micro-notches in the selected grains, 2) reveal the crack morphology and grain structure in 3-D by cross sectioning, 3) perform

ISE imaging which provided complementary information over SE imaging. Two dual-beam SEM/FIB systems, FEI Quanta 200-3D and Hitachi NB5000, were used to carry out the experiments above.

2.3 Crystallographic Orientation

2.3.1 Description of Crystallographic Orientation

Texture is the non-random distribution of the crystallographic orientation of grains, or, a phenomenon of preferred orientation of grains [153, 154]. The texture has significant influence (20%~50% in many cases) on many material behaviors, such as mechanical properties, electronic properties, optical properties and so on [153]. In metallic materials, when a polycrystalline metal is plastically deformed, the lattice orientation of individual grains is rotated toward a preferred orientation in which certain lattice directions are aligned with the principal directions of plastic flow in the metal. The textured grains by forming processing are not to return to a random state by recovery, recrystallization and grain growth in the following heat treatment, instead, are to be transformed into new preferred ones which dramatically depend on chemical composition, initial orientation state, processing parameters and so forth. Two terms were usually used to describe the texture in materials. One is macro-texture describing the statistical orientation distribution of grains in a bulk material; the other one is micro-texture focusing on the individual grain orientation related to one or several more local grains. Over the years along the development of characterization techniques for texture measurement, several expression methods of texture were widely used, as discussed in the following paragraphs.

2.3.1.1 Miller Indices

Miller indices is a common orientation description which is expressed in the form of {hkl}<uvw>. The {hkl} represents the crystal plane perpendicular to the sample normal

direction (ND) while <uvw> denotes the crystal direction parallel to the certain processing (e.g. extrusion or rolling) direction of the sample (RD). For example, cooper (Cu) orientation can be denoted by {112}<111>, meaning {112} plane being parallel to ND and <111>aligned along RD.

2.3.1.2 Pole Figure and Inverse Pole Figure

The pole figure is a two-dimensional stereographic projection, with crystal orientation specified relative to the specimen geometry, which shows the variation of pole density with pole orientation for a selected set of crystal plane {hkl} [155]. For an individual crystal orientation (hkl)[uvw], its location on the pole figure is given by the stereographic projection of $\bar{n}$ in the spatial equatorial plane, where $\bar{n}$ is the unit vector normal to the (hkl) crystal plane and has spatial components in the (hkl)[uvw] orientation given by the column vector (Equation 2.2),

$$
\begin{pmatrix} n_1 \\ n_2 \\ n_3 \end{pmatrix} = \frac{1}{\sqrt{h^2+k^2+l^2}} \begin{pmatrix} \frac{u}{n} & \frac{kw-lv}{mn} & \frac{h}{m} \\ \frac{v}{n} & \frac{lu-hw}{mn} & \frac{k}{m} \\ \frac{w}{n} & \frac{hv-ku}{mn} & \frac{l}{m} \end{pmatrix} \begin{pmatrix} h \\ k \\ l \end{pmatrix}
\tag{2.2}
$$

where $m = \sqrt{h^2 + k^2 + l^2}$, $n = \sqrt{u^2 + v^2 + w^2}$.

To determine the position of a given pole on the sphere plane usually requires two angles: the angle α describing the azimuth of the pole, where α=0˚ is the north pole of the unit sphere, and angle β characterizing the rotation of the pole around the polar axis. These two angles start from a set specified external reference directions, which are usually selected to coincide with sample coordinates or processing directions (such as ND and RD, respectively, for rolled/extruded symmetry, Figure 2.8). The two pole figure coordinates α and β are corresponding to the spherical coordinate of $\bar{n}$ on the unit sphere through Equation 2.3 and is shown in Figure 2.8.

$$\begin{pmatrix} n_1 \\ n_2 \\ n_3 \end{pmatrix} = \begin{pmatrix} sin\alpha cos\beta \\ sin\alpha sin\beta \\ cos\alpha \end{pmatrix} \qquad (2.3)$$

In order to unambiguously represent an orientation, an individual pole is insufficient because the crystal can still rotate about this particular pole. The number of poles to unequivocally characterize a crystal orientation depends on the crystal symmetry or the pole symmetry, but generally three poles are necessary to determine an orientation completely. The more details regard measuring pole figures will be introduced later. In one word, the pole figure characterizes the pole positions on the equatorial plane in a stereographic projection, with respect to processing directions.

Rather than representing the orientation of the crystal coordinate system in the sample coordinate system, vice versa, the orientation of the specimen coordinate system can be projected into the crystal coordinate system, which is referred to as inverse pole figure. In the reverse pole figure, the reference system is the crystal coordinate system, and the "orientation" is defined by the axes of the sample coordinate system, e.g. RD, TD and ND. Unlike the pole figure, the inverse pole figures have not to show the entire equatorial plane, but one unit triangle will suffice. For example, for the cubic crystal symmetry, the unit triangle <100>, <110> and <111> is sufficient. However, for representation of macro-texture data, inverse pole figures are usually inferior to pole figures.

2.3.1.3 Rotation Matrix

In order to specify an orientation, two reference coordinate systems are required: one relating to the whole specimen (global/sample coordinate system) and the other one relating the crystal (crystal coordinate system). Usually, both of them are right handed Cartesian systems. The axes of the sample coordinate system $S = \{s_1 s_2 s_3\}$ are conventionally chosen according to important surface/direction associated with the external form or shape of the sample, e.g. the rolling direction (RD), the transverse direction (TD) and normal of rolling plane (ND). The crystal coordinate system

$C = \{c_1 c_2 c_3\}$ is usually assigned to the direction of low indices or crystal symmetry, e.g. axes [100], [010] and [001] in orthogonal branch (i.e. cubic, tetragonal, orthorhombic structure).

Rotation matrix, embodying the rotation of the sample coordinates onto the crystal coordinates, is a square matrix of nine numbers (Equation 2.3). The first row of the matrix is given by the cosines of the angles (α_1, β_1, γ_1) between the first crystal axis, [100], and each of the three specimen axes, X, Y, Z, in turn (Figure 2.7). The second row of the orientation matrix is given by the cosines of the angles (α_2, β_2, γ_2) between [010] and X, Y, Z in turn. Similarly, the third row of the matrix comprises the cosines of the angles (α_3, β_3, γ_3) between [001] and X, Y, Z. In a complete form, the rotation matrix is expressed by Equation 2.4

$$g = \begin{pmatrix} cos\alpha_1 & cos\beta_1 & cos\gamma_1 \\ cos\alpha_2 & cos\beta_2 & cos\gamma_2 \\ cos\alpha_3 & cos\beta_3 & cos\gamma_3 \end{pmatrix} = \begin{pmatrix} g_{11} & g_{12} & g_{13} \\ g_{21} & g_{22} & g_{23} \\ g_{31} & g_{32} & g_{33} \end{pmatrix} \tag{2.4}$$

With the rotation matrix, the sample coordinate system (C_S) and crystal coordinate system (C_C) can be correlated with and transformed to each other by Equation 2.5

$$C_C = g \cdot C_S \tag{2.5}$$

2.3.1.4 Euler Angles and Euler Space

Compared to Miller indices, pole figure and rotation matrix, Euler angles are three numbers that can concisely express the crystal orientation. The Euler angles refer to three sequent rotations that transform the sample coordinate system onto the crystal coordinate system. Generally, there exist three major rotation conventions which were proposed and developed by Bunge, Roe and Kocks [154, 156], respectively. Among them, the most commonly used is Bunge's convention whose three sequent rotations are performed as following and Figure 2.9 [153, 154, 157, 158]:

1. φ_1 – about the ND, transforming TD into TD' and RD into RD', rotation matrix = $g_{\varphi 1}$

2. Φ- about the axis RD' (new orientation), transforming TD' into TD" and ND into ND", rotation matrix = g_Φ

3. φ_2 – about the ND" (new orientation), rotation matrix = $g_{\varphi 2}$

Here, $\varphi_1, \Phi, \varphi_2$ are the Euler angles. These three rotation results in a total rotation of

$$g = g_{\varphi 2} \cdot g_\Phi \cdot g_{\varphi 1} =$$

$$\begin{pmatrix} cos\varphi 1 cos\varphi 2 - sin\varphi 1 sin\varphi 2 cos\Phi & sin\varphi 1 cos\varphi 2 + cos\varphi 1 sin\varphi 2 cos\Phi & sin\varphi 2 sin\Phi \\ -cos\varphi 1 sin\varphi 2 - sin\varphi 1 cos\varphi 2 cos\Phi & -sin\varphi 1 sin\varphi 2 + cos\varphi 1 cos\varphi 2 cos\Phi & cos\varphi 2 sin\Phi \\ cos\varphi 2 sin\Phi & -cos\varphi 1 sin\Phi & cos\Phi \end{pmatrix}$$

(2.5)

With the Euler angles, any crystal orientation can be represented unequivocally as a point in a 3-D coordinate system whose axes are spanned by the three Euler angles. Such a 3-D coordinate system (or space) is referred to as Euler space. To represent all possible crystal orientations, the maximum size of the Euler angle space varies with the symmetry of the crystal structure. It requires larger Euler space size for low-symmetry crystal structures while smaller for high-symmetry ones. For example, the range of $0° \leq \varphi_1, \varphi_2 \leq 360°$ and $0° \leq \Phi \leq 180°$ is required to define the triclinic crystal symmetry, which also define the maximum size of the Euler angle space; while the range of the Euler angles is reduced to $0° \leq \varphi_1, \Phi, \varphi_2 \leq 90°$ to fully represent $m\bar{3}m$ symmetry in cubic crystal system. If considering the symmetries of 6/mmm, the space size can be further deducted to the range of $0° \leq \Phi, \varphi_1 \leq 90°$ and $0° \leq \varphi_2 \leq 60°$. Although the crystal orientation appears three times in the reduced Euler angle space due to high-symmetry of cubic structure, i.e. it only requires a further reduced Euler angle space to fully represent all crystal orientations, the range of $0° \leq \varphi_1, \Phi, \varphi_2 \leq 90°$ is

commonly used for general description of the crystal orientation in a cubic system [153, 154].

2.3.1.5 Orientation Distribution Function (ODF)

Superior to pole figure, orientation distribution function (ODF), which is defined as probability density function of orientation, g, offers an unequivocal description of texture in 3-D Euler space ($\varphi_1 - \Phi - \varphi_2$) [154]. Assuming a microstructure consisting of different grains i of volume V_i with different orientations, the ODF $f(g)$ is defined by the relationship expressed in Equation 2.6.

$$\frac{dV}{V} = f(g)dg, \text{with } dg = \frac{1}{8\pi^2} sin\Phi d\varphi_1 d\Phi d\varphi_2 \text{ and } \oint f(g)dg = 1 \qquad (2.6)$$

where V is the sample volume and dV is the volume of all crystallites i with the orientation g in the angular element dg and g is a function of ($\varphi_1, \Phi, \varphi_2$). In practice, the ODFs are mathematically computed from the experimentally measured pole figures. The pole density $P_{hkl}(\alpha, \beta)$ is correlated with Euler angles through Equation 2.7.

$$P_{hkl}(\alpha, \beta) = \frac{1}{2\pi} \cdot \int_{\gamma=0}^{2\pi} f(g)d\gamma \ , \ g = \{\varphi_1, \Phi, \varphi_2\} \qquad (2.7)$$

where γ corresponds to the possible rotation angle of the crystallite about direction (hkl) in the pole figure. The Equation 2.7 has to be solved in order to calculate the ODF ($f(g)$), which is commonly conducted by two main approaches, i.e. series expansion method and direct method, though series expansion is most often used.

In the series expansion method, the to-be-solved function $f(g)$ together with pole figure $P_{hkl}(\alpha, \beta)$ is expanded to series of harmonic functions Equation 2.8 and 2.9.

$$f(\varphi_1, \Phi, \varphi_2) = \sum_{l=0}^{\infty} \sum_{m=-l}^{+l} \sum_{n=-l}^{+l} C_l^{mn} T_l^{mn}(\varphi_1, \Phi, \varphi_2) \qquad (2.8)$$

$$P_{hkl}(\alpha, \beta) = \sum_{l=0}^{\infty} \sum_{n=-l}^{+l} F_l^n(hkl) \, k_l^n(\alpha, \beta) \qquad (2.9)$$

The two expansions are related through the Equation 2.7 and the corresponding coefficients C_l^{mn} and $F_l^n(hkl)$ which has the form of

$$F_l^n(hkl) = \frac{4\pi}{2l+1}\sum_{m=-l}^{+l} C_l^{mn} k_l^{*m}(\theta_{hkl}, \gamma_{hkl}) \qquad (2.10)$$

The coefficients $F_l^n(hkl)$ can be obtained by integration of Equation 2.9 over (α, β), which yields

$$F_l^n(hkl) = \int P_{hkl}(\alpha, \beta) k_l^{*n}(\alpha, \beta) \sin\alpha \, d\alpha \, d\beta \qquad (2.11)$$

The asterisks terms k_l^{*m} and k_l^{*n} are harmonic functions [156]. Thus, the calculation of $f(g)$ can be achieved following the steps $F_l^n(hkl) \rightarrow C_l^{mn} \rightarrow f(g)$. Most of the calculation using this method was carried out in an approximation $16 \leq l \leq 22$ and 5° steps for angular variables $\varphi_1, \Phi, \varphi_2$ for cubic crystal.

2.3.2 Texture Measurement

2.3.2.1 Macro-texture Measurement by X-ray Diffraction

The macro-texture is usually measured by X-ray diffraction and expressed by pole figure. The principle of pole figure measurement by X-ray is based on Bragg's law for reflection of radiation at the crystal lattice planes, i.e. $\lambda = 2 \, d_{hkl} \sin\theta$. For most bulk materials, back reflection method is commonly used, and its geometry is demonstrated in Figure 2.10. During the measurement, the sample is first mounted on a sample stage driven by a goniometer, with its sample coordinates coinciding with three perpendicular rotation axes $(\varphi, \chi \text{ and } \omega/\theta)$ of the goniometer, i.e. RD//ω, TD//χ and ND //φ [159]. To measure the intensity of pole (hkl), the X-ray source and detector/counter are then positioned to have an angle of *180-2θ_{hkl}*, with the bisectrix between the incident and diffracted beams being normal to the sample surface. In this geometry, only the crystal planes (hkl) with normals parallel to the bisectrix can diffract the X-ray beam that can be received by the detector. In order to measure the orientation of all (hkl) planes in the

sample surface, the sample has to be rotated around axis φ and axis χ, respectively. In most modern stepper-motor driven X-ray systems, the sample firstly rotates 360 about axis φ (i.e. $\varphi = 0 \rightarrow 360°$), then around χ for a certain degree that meets the requirement on resolution (typically 5°), followed by the rotation around axis φ for 360 and subsequently χ for 5° again. This cycle is repeated until χ spans to 90° for a complete pole figure. The rotations about axis φ and axis χ are related to the coordinates, α and β, in the texture analysis pole figure, by the relation of $\beta = \varphi$ and $\alpha = 90° - \chi$ (Figure 2.11). As the specimen rotates, the X-ray scans over the area on the equatorial plane. The intensity distribution of a particular crystallographic direction in the polycrystalline in the specimen can be recorded and analyzed. It is defined by the volume fraction dV/V of crystals having their crystallographic direction parallel the bisectrix (Equation 2.12)

$$\frac{dV}{V} = P_{hkl}(\alpha, \beta) sin\alpha d\alpha d\beta \tag{2.12}$$

where $sin\alpha d\alpha d\beta$ is the unit area on the sample direction. $P(\alpha, \beta)$ is the pole density which represents the number of crystals whose direction is parallel to sample direction, i.e., the probabilities of crystal direction aligns in the normal direction to (hkl). It is necessary to note that the description of texture by pole figure is incomplete because it just provides a specific crystal direction without discerning the rotation of the crystals about this direction. There is no way to use pole figures to obtain an unequivocal and complete orientation of individual grains or volume elements.

2.3.2.2 Micro-texture Measurement by EBSD

Electron backscatter diffraction (EBSD) has become a widely used microstructural crystallographic technique to examine the crystallographic orientation of many materials. An EBSD system is usually associated with an SEM and uses the diffraction pattern (Kikuchi pattern [160]) from the illuminated volume to determine the crystal orientation. The configuration of an EBSD system is schematically shown in Figure 2.12. In the

EBSD measurement [161, 162], the sample is tilted towards to the EBSD detector (fluoresces screen) at a relatively high angle (usually 70˚ for most systems), allowing more electrons to be diffracted towards a fluorescent screen positioned at a certain distance to the tilted sample. When the incident electrons bombard the sample surface, they are diffusely scattered in all directions. This means that there must always be some electrons arriving at the Bragg angle θ_B at every set of lattice planes, and these electrons can then undergo elastic scattering to give a strong and reinforced beam that gives rise to Kikuchi pattern, which is schematically shown in Figure 2.12(b). The locus of the diffracted radiation is the surface of cone (called Kossel cone) that extends about the normal of the diffracting atomic plane (hkl). The source of electron scattering can be considered to be between the lattice planes, thus two cones of radiation result from each plane-family. Because of the high energy of the incident beam (20-30 keV), the electron wavelength is very small, which generally yield the Bragg angle θ_B to be ~0.5˚. Consequently, the apex angle of a diffraction cone is close to 180˚, meaning the cones are almost flat. The diffracted electrons (cones) are intercepted by a phosphor screen positioned against the sample surface, so that the electrons (cone surfaces) can be recorded as almost straight lines and form Kikuchi pattern on the screen. Since the Kossel cones from a lattice plane are formed in pairs, thus the whole Kikuchi pattern consists of pairs of parallel lines where each pair, or "band," has a distinct width and corresponds to a distinct crystal plane. The Kikuchi pattern contains a wealth of crystallographic information, such as angle between Kikuchi bands, band width, and distance between poles. In determining an individual pattern, the experimentally recorded pattern is processed, and compared with the theoretically one simulated based on the database, and then the software can calculate the crystallographic orientation.

In this study, EBSD work was carried out on a Field Emission Gun SEM (Hitachi S-4300), equipped with a CCD camera and a Channel EBSD system (HKL Technology, Demark). The crystal orientation of the location of interest in the sample was measured

by scanning the area point by point in a step size of 0.3-1 μm, with the acceleration voltage of 20 KV and working distance of 21 mm. The measured crystal orientation was expressed in Euler angles (φ_1, Φ, φ_2).

2.4 Numerical Modeling Software

A part of the present research work is based on numerical calculations and simulations, for example the calculation of short fatigue crack growth through grains, prediction of crack length in textured alloys, twist angle mapping in Euler space, statistics analysis of the simulation results, etc. To fulfill these calculations, programs were developed using Matlab software. Compared with other commercial languages, such as C and Fortran, Matlab offers efficient matrix manipulations and graphical functions.   More importantly, Matlab provides convenient interface with other languages and software, allowing convenient extending to or adapting our program code with other applications. More details regarding the modeling and simulation will be discussed in Chapter 5 and 6.
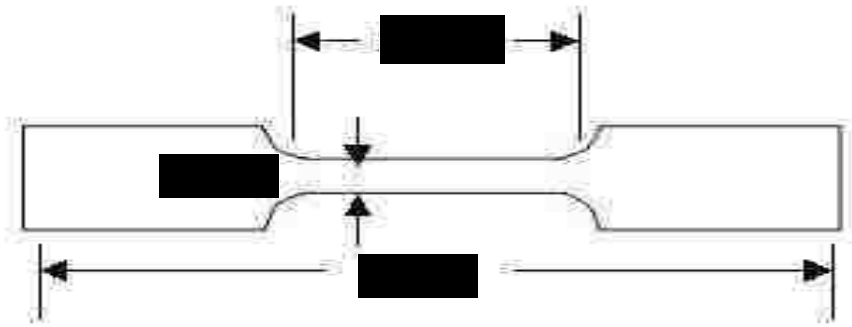
Figure 2.1 Geometry of the dog bone shaped tensile test specimens.

Figure 2.1 The Instron 8800 servo-hydraulic test machine used for tensile test.
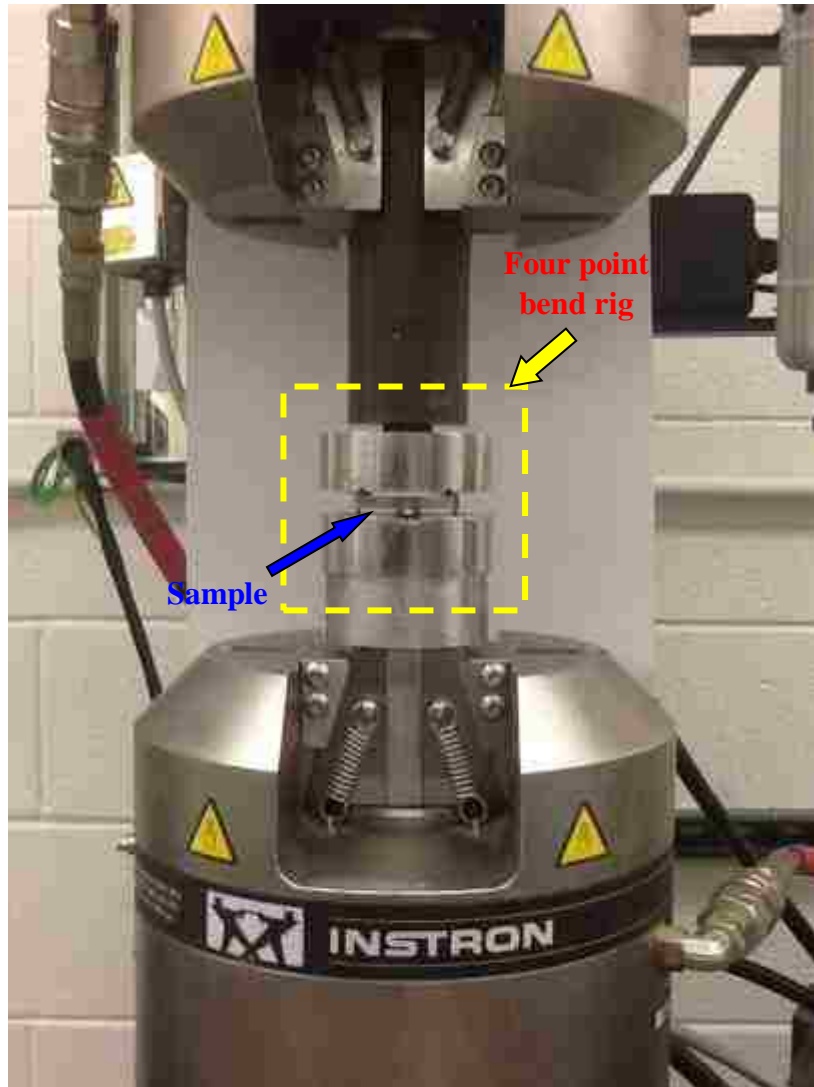
Figure 2.3 Loading geometry of the self-aligning four-point bend fatigue testing rig.
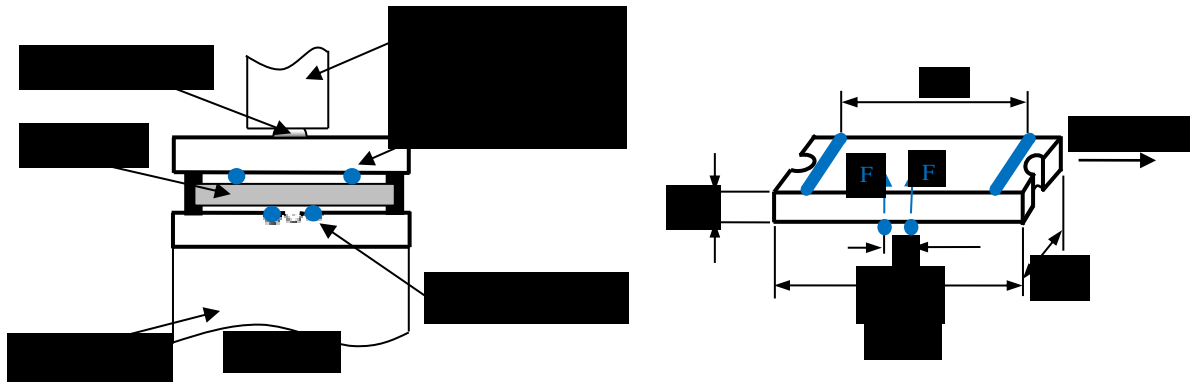
Figure 2.4 Schematic diagrams showing, (a) the testing geometry, and (b) the sample geometry used in four-point bend fatigue tests [145].
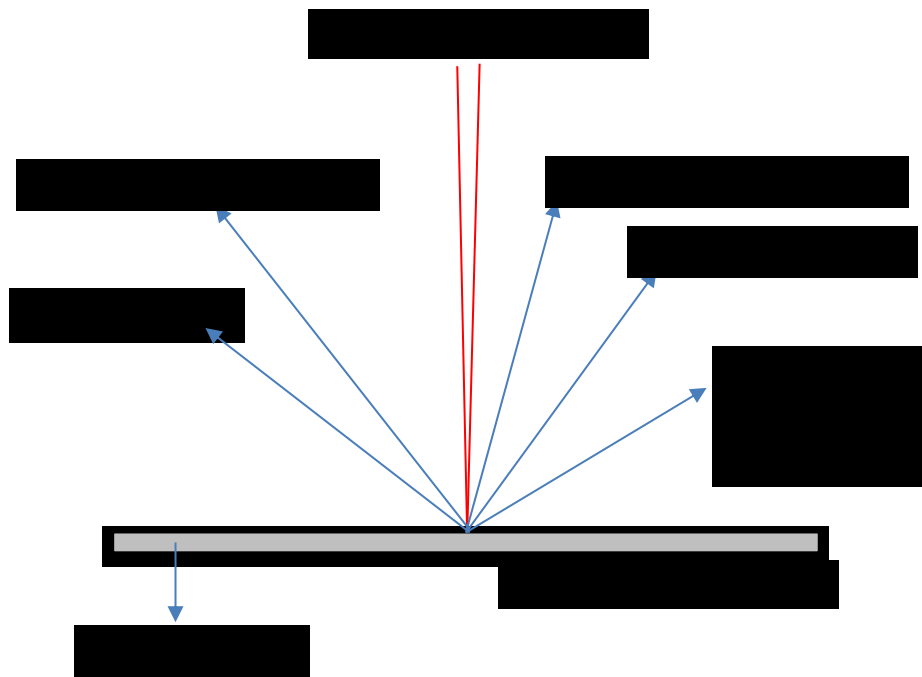
Figure 2.5 Main signals produced by electron bombardment in an SEM
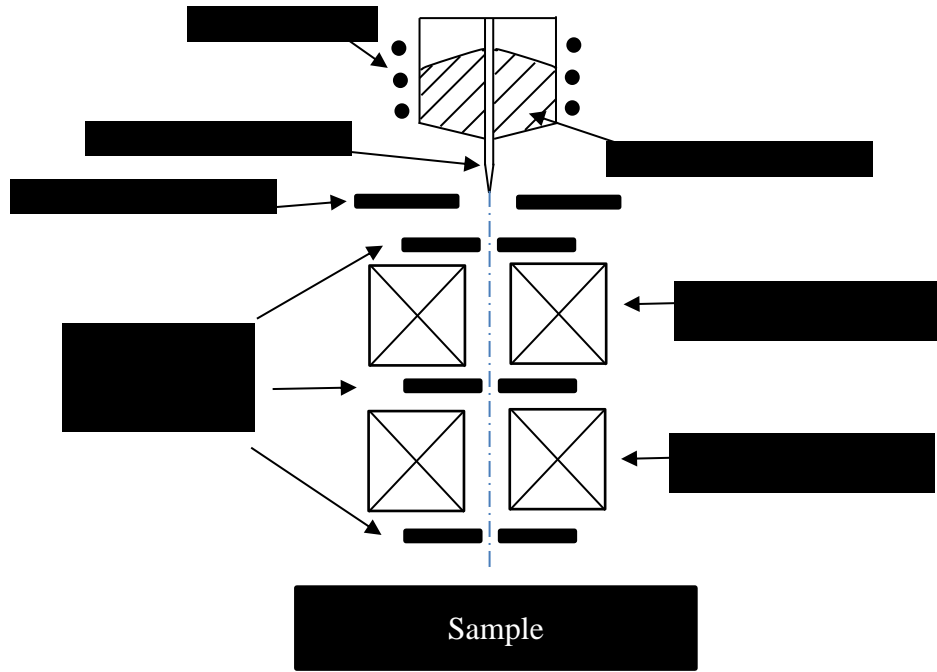
Figure 2.6 Schematic diagram of the LMIS and lens system of an FIB
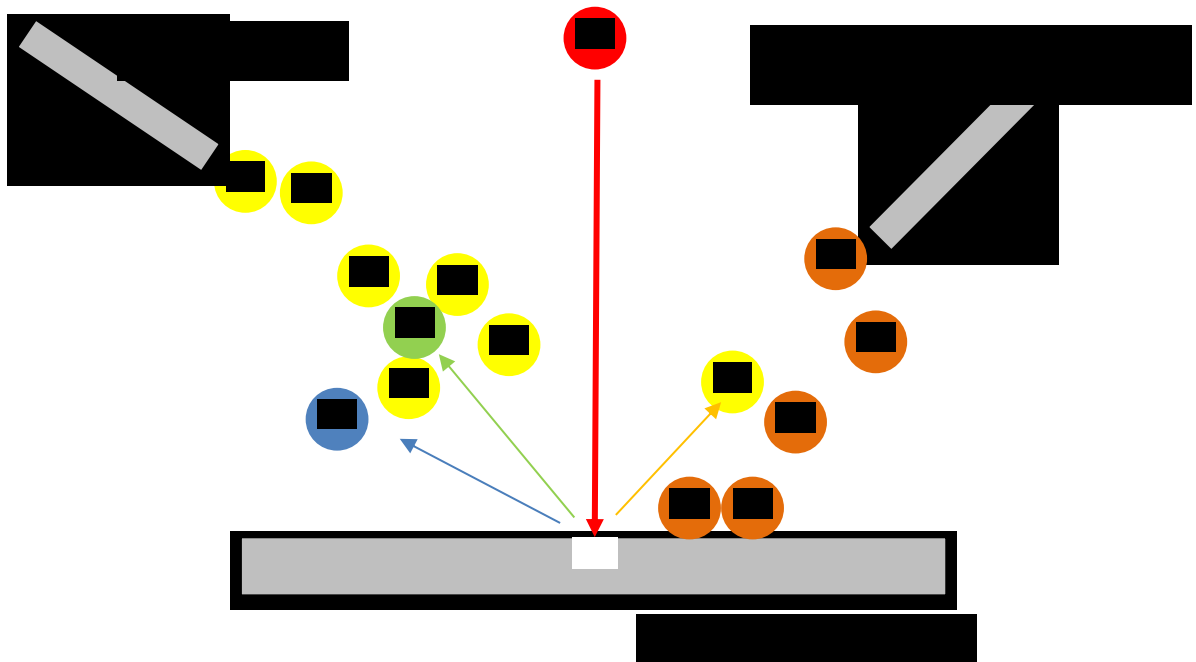
Figure 2.7 Main interaction of Ga^+ with sample material in an FIB
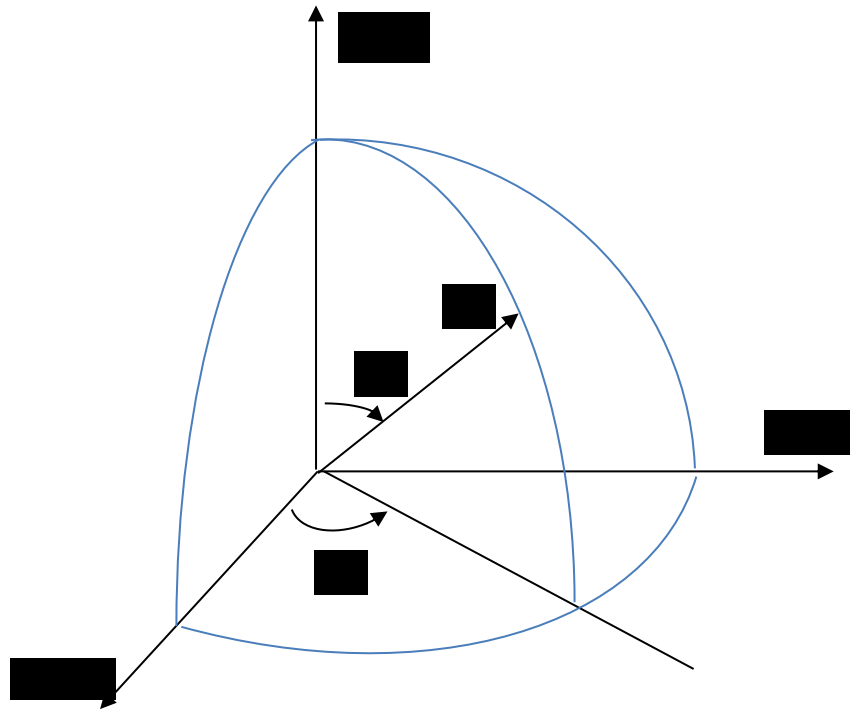
Figure 2.8 Sketch diagram showing the relationship of two pole figure coordinate (α, β) and the spherical coordinate of $\bar{n}$ on the unit sphere
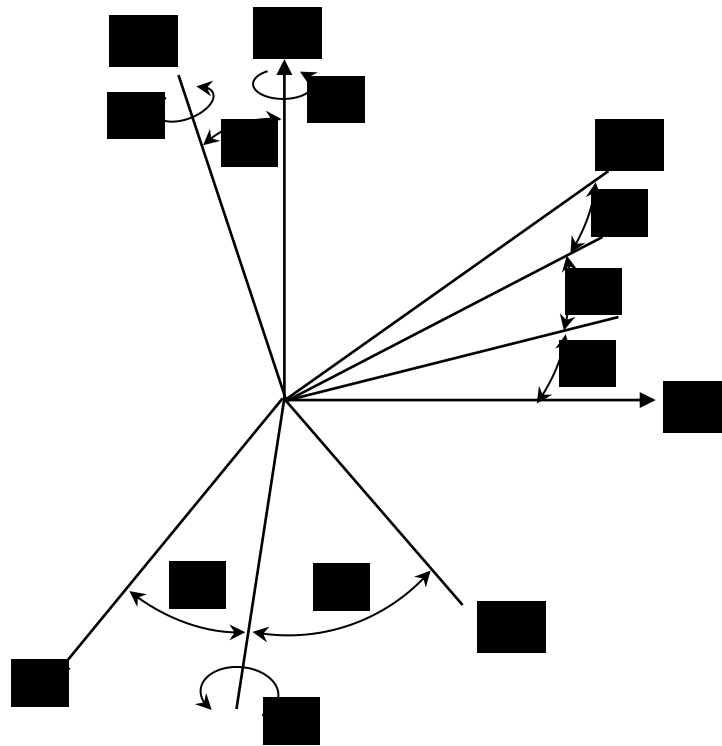
Figure 2.9 Relationship between sample coordinate system and crystal coordinate system

in definition of Euler angles
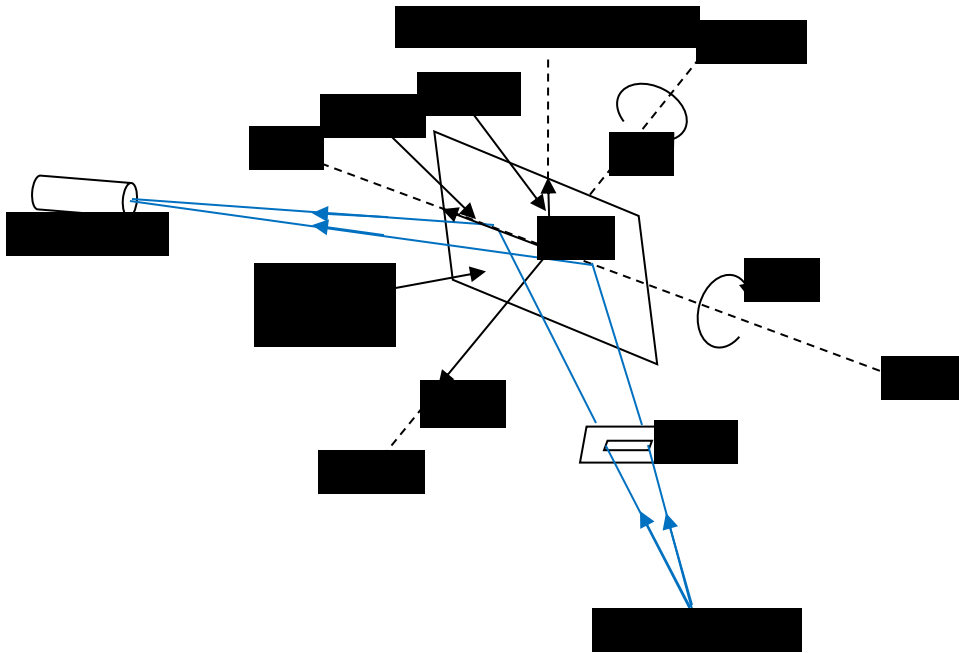
Figure 2.10 Schematic diagram showing reflection geometry in X-ray diffraction experiments [70].
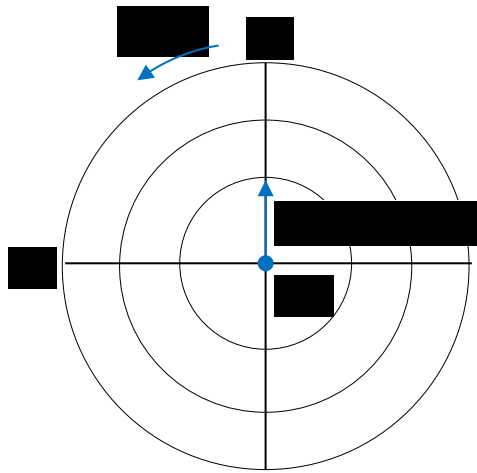
Figure 2.11 Schematic diagram showing relation of rotation angles (α, β) in XRD geometry and angles (φ, χ) in pole figure

(a)

Sample

Electron Beam

Diffracting planes

Tilted sample

Screen

Kikuchi lines

(b)
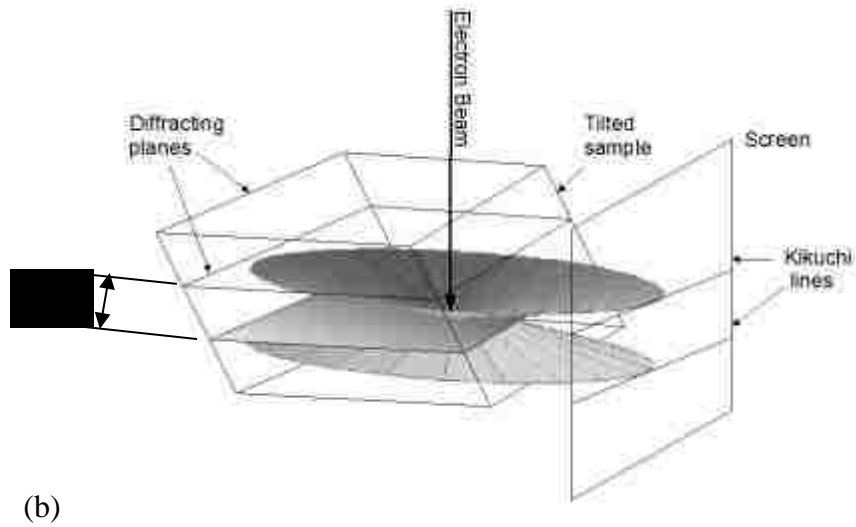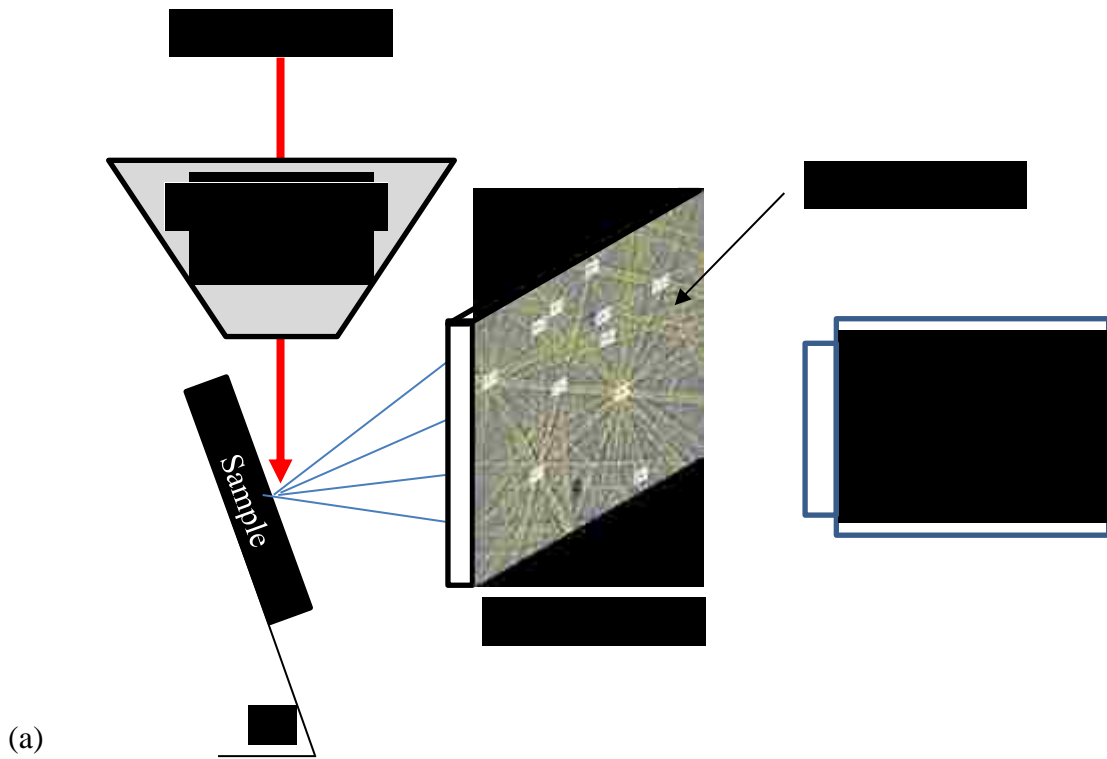
Figure 2.12 Schematical diagram show ing (a) the tpycial geometry for an EBSD system, (b) the formation of Kikuchi lines

Chapter 3 3-D Effects of Microstructures on Short Fatigue Crack Growth

It has already been well recognized that the behavior of short fatigue crack growth is significantly influenced by the local microstructures which include grain boundary (GB), phase boundary, constituent particles, voids, etc. Among different types of microstructures, GBs have been recognized as the major factor controlling short crack propagation. Many 2-D models dealing with the GB effect on short crack growth have been proposed in the last few decades; however, they are incapable of satisfactorily explaining the short crack behaviors observed experimentally, due to their 2-D nature. Recently, 3-D effect of GBs on short fatigue crack behavior has drawn intensive attention in research. Some new understanding in 3-D has been achieved, but further studies need to be conducted to elucidate the behaviors of short fatigue crack growth thoroughly and quantitatively. This chapter focuses on the 3-D effect of GBs on short fatigue crack growth in precipitation hardened high strength Al alloys.

3.1 Introduction

Due to the effect of local microstructure and texture, short fatigue cracks often behave differently from long cracks in alloys. For example, they are often deflected and branched at grain boundaries (GBs), sometimes even inside grains, and show significantly higher but scattered growth rates than long cracks under the same nominal driving force [66-69]. Since a short fatigue crack grows preferably along a slip plane within one grain and is often deflected at a GB/phase boundary, GBs/phase boundaries are commonly considered to be one of the major barriers to short fatigue crack growth and account for the marked variation of the short fatigue crack growth rate measured in most engineering alloys [62, 63, 65, 94]. Several analytical models have previously been developed in attempts to take into account the effects of local GBs/phase boundaries and crystallographic orientation on short fatigue crack growth behavior. Hobson [163] accommodated the effect of GBs into two equations describing short crack growth via a statistical approach. However, his model only yields good agreement with experimental data within the first grain but fails beyond that [164]. Chan and Lankford [104] reconsidered the crack tip plastic strain

range and modified the linear elastic fracture mechanics (LEFM) by introducing a crystallographic function $K(\Phi)$ with respect to resolved shear stress in cracked grain and its neighboring grain in front of the crack tip. Their model cannot satisfactorily explain the marked scattering often observed in growth rate of short cracks. For example, it predicts little or no deceleration in growth rate within individual grains. Based on the constraint on the crack tip plastic zone size [63], Navarro and De los Rios [117, 118, 122] incorporated the Sachs factor averaged over the grains along the crack front into their 2-D dislocation model which took into account the effect of slip band blocking by a GB in simulating short crack growth. Although it can predict the crack growth retardation at grain boundaries, this model cannot distinguish the difference in resistance between different types of GBs. Moreover, it is unable to explain crack branching at GBs and crack deflection observed inside grains rather than at a GB where the resistance to crack growth is expected to be the largest. These 2-D models could hardly deal with the 3-D effects of microstructures on short crack growth behavior. It is still desirable to quantitatively understand the relationships between local microstructure and texture, and short fatigue growth behavior in 3-D, in order to develop a microstructurally-based model for predicting the life of a short fatigue crack in engineering alloys.

Traditionally, misorientation of two neighboring grains is often used to describe directly crack deflection at their boundary for the sake of convenience, e.g., a high angle GB should lead to a large angle deflection, whereas a small angle deflection takes place only at a low angle GB [165, 166]. Such an assumption could often be invalid since the GB geometry has to be taken into account in understanding crack deflection at the GB. The misorientation of two grains is unrelated to the GB geometry but the orientations of the two grains. As shown in Figure 3.1, Zhai et al. [95, 167] have revealed that the crack deflection can be better described with twist and tilt components of the deflection at a GB and that these components are the key parameters that control the growth behavior of short fatigue cracks across GBs in an AA 8090 Al-Li alloy. With such a crystallographic model, the 3-D characteristics of short crack growth, such as crack deflection and branching at GBs, deflection inside grains, crack retardation and arrest at GBs, can all be explained qualitatively. Recently, Marx et al [107] investigated the interaction of the short fatigue crack emanated from artificial notch with GB using a 3-D FIB tomography

technique. Their work not only supported Zhai's crystallographic model, as described in [95], but also revealed that the inclination of a GB below the sample surface could influence the crack growth rate when the crack was propagating across the GB. However, the effect of GB inclination on crack twist at GB has not been quantitatively analyzed and the cracks studied in only covered two grains [107]. Ludwig et al [112], using diffraction and phase-contrast X-ray tomography, obtained a complete graphical   description of the local crack growth rates of short fatigue cracks in 3-D. Although this tomography technique enables to non-destructively detect grain shape, grain position, grain orientation and crack growth in grains, its spatial resolution still needs to be enhanced in order to investigate the mechanism for short crack growth in microscopic scale. Therefore, work still needs to be done to first fully understand how the growth behavior of a short crack, including its growth path and rate, are controlled by the local grain structure and texture along its path that covers several grains; and second quantify the relationships between the growth behavior and the local microstructure and texture.

This work was carried out to study the growth behavior of a short crack by studying its growth path and rate as regard to the local grain structure and texture along the crack path in an AA8090 Al-Li alloy. The results from the present work demonstrated that GB tilting could also affect twist angle of crack deflection at the GB and that the GB could still influence the growth behavior after the crack passed the GB on surface. The results obtained from this work may serve as a foundation for building up a 3-D quantitative relationship between growth behavior of a short crack and local microstructure in an engineering alloy.

3.2 Experimental Details

The experiments of this part have been completed earlier by Zhai [87, 95, 101], however, the results have not been thoroughly analyzed. In order to provide clear and complete information about the experiments, the experimental details are introduced as following.

3.2.1 Material, Fatigue Test and Crack Growth Measurement

A 45 mm thick Al-Li 8090 alloy plate (for detailed chemical composition see ref. [87]) was used in this work. Its temper condition and microstructure are described in [101].

Samples (36×10×4.6 mm3) for four point bend fatigue were cut with the plane under the tension loading being parallel to the L-S plane (L-the rolling direction and S-the rolling plane normal) and the loading axis being along the rolling direction. The surface under the maximum tensile stress in four-point bend in each sample was ground and mechanically polished before the fatigue tests which were conducted using a self-aligning four-point bend rig [145] under a constant maximum stress (246 MPa), equivalent to 50% the yield stress (492.1 MPa), at frequency of 20 Hz, stress ratio R= 0.1 and room temperature in air. The fatigue strength of the alloy in the L direction was 197 MPa (i.e., the maximum stress).

The fatigue tests were periodically interrupted to detect short cracks and follow their length on the sample surface using an optical microscope at 50× and 200×, respectively. An interval between 1000 to 5000 cycles was chosen so that several points within each grain could be measured in the crack growth rate curve in hope of studying orientation effects of the grain and GBs on short crack growth. In the case that the crack tip passed through a GB during a period of fatigue, the number of cycles at which the crack propagated across the GB was estimated. The error of the estimation could be very limited because the interval between each observation is relatively very small.

3.2.2 Electron Back Scatter Diffraction Experiments

After the measurement of the growth rate curve of the selected cracks, the crystallographic orientation of each grain that interacted with the cracks was determined using electron back scatter diffraction (EBSD). For EBSD measurement the sample surface was etched with a Keller's etchant after the fatigue tests. From the EBSD measurement, an orientation matrix for each grain was obtained, so that the orientations of all the possible slip planes in each grain could be determined. Thus, crack plane orientation can be determined by matching the crack path with one of the traces of the slip planes on the sample surface [95].

3.3 Results and Discussions

3.3.1 Short Fatigue Crack Path

A short fatigue crack was found on the sample surface at 7×10^5 cycles when it was about 30 μm long, and subsequently its growth was monitored by interrupting the fatigue test periodically until 9.15×10^5 cycles. Figure 3.2 shows its morphology before and after etching at 9.15×10^5 cycles. Note that part of this crack, from grain 7 to grain 11, was used in an earlier paper to demonstrate the α and β effects on crack path in this alloy. In this paper, the growth behavior of the rest of the crack, including its path and growth rate, as well as the effect of GB tilt, are discussed.

The crack was initiated perpendicular to the loading axis in grain 3 (Figure 3.2). The growth behaviors of its two tips were measured separately. The crack growth was predominantly crystallographic, i.e., the crack was deflected at each GB it passed, as revealed in Figure 3.2(b). The deflection angles varied substantially at GBs. The crack also bifurcated at GB3/5 (the notation of GBi/j means the GB between grains i and j), GB10/11, GB11/12 and GB15/16, respectively.

3.3.1.1 Crack Initiation

With the knowledge of grain orientation (determined from EBSD measurement), the crystal plane of the crack plane in each fractured grain could be identified by matching the crack path with one of the traces of the slip planes on the sample surface. It was found that the deflection angle, 86°, of the crack path in grain 3 did not match any of the angles, θ, (i.e., the angle between the trace of a crystal plane on the surface and the load axis in the grain (Figure 1.1), 72.6°, 31.1°, -40.1° and -73.3°, calculated for all four {111} planes in the grain. It could only match the angle of the (001) plane on the surface of the grain instead. This suggested that the crack plane was likely to be along the (001) plane which was approximately vertical to the load axis. Examination of the fracture surface of this sample revealed that the crack was indeed roughly perpendicular to the load axis in grain 3, as shown in Figure 3.3(c) where the sample surface is perpendicular to the viewing angle. It has previously been recognized that cracks are preferably initiated in a cleavage fashion

with the facet plane being along {100} or {110} plane which is perpendicular to the load axis in an Al alloy which contains trace elements, such as Na and K, over 10 ppm in content [168-170]. It was not surprising that the alloy used in this work might contain these trace elements in the amount over 10 ppm, as these elements are the natural impurities in Al-Li alloys because it is hard to separate them from the alloying element, Li, in the alloys.

3.3.1.2 The α Minimization Criterion for Short Crack Growth

The orientations of all the grains that interacted with the crack in Figure 3.1 were determined using EBSD after the sample was etched at 9.15×10^5 cycles. θ, ψ (as defined in Figure 1.1) and Schmid factor (m) of all the four {111} planes in each of these grains were calculated, assuming that the GB planes in the sample were all parallel to L-T plane (T-the long transverse direction), i.e., perpendicular to the sample surface. This assumption was made to resemble the grain structure in a rolled plate or sheet product of Al alloys where grains are usually in a pancake/disc shape, i.e. the planar GBs of the pancake-shaped grains are parallel to the L–T plane, and are the major boundaries with which a crack interacts. By matching to the crack path with one of the traces of the four {111} planes on the sample surface, the crack plane could be determined in each grain. The twist (α) and tilt (β) angles of the crack deflection at each GB (between grains *a* and *b*) were then derived by $\alpha = |\psi_a - \psi_b|$ and $\beta = |\theta_a - \theta_b|$ respectively and regarded as the measured values of α and β. These values were compared to the minimum possible α and the corresponding β, termed as the predicted α and β, at each GB, since a short crack is believed to follow the path that offers the minimum α at each GB [95]. These results are listed in Table 1, and the calculated θ, ψ and Schmid factor (m) of all the four {111} planes, together with the observed θ, in each grain are given in Table 3.1. It is evident in Table 1 that the observed θ in each grain that interacted with the crack, except grain 3, was in good agreement with that of the trace of one {111} plane in the grain, and that the observed α was consistent with the minimum possible twist angle at most GBs that the crack propagated through. This meant that, after the crack was initiated on a (001) plane in grain 3, the subsequent path of the crack across GBs followed the slip plane that formed the minimum twist angle between the crack planes across each GB in this alloy.

However, as shown in Table 1, four GBs (GBs 3/2, 2/1, 16/19 and 16/17), out of the 13 GBs through which the crack propagated, failed to provide the minimum α for the crack growth, i.e., the observed α at the GBs were not the minimum values among the four possible slip planes. As will be discussed in details in Section 3.1.3 and 3.1.4 in this chapter, this was caused by the discrepancy between the actual grain structure in the alloy and that used in calculating α, since GBs sometimes might not be parallel to L-T plane beneath the sample surface and there might also be some secondary GBs buried beneath the surface in the alloy. These GBs could alter the crack path on the surface from that predicted by assuming that GBs were parallel to L-T plane. It appeared that β was not as dominant as α in controlling the path of crack growth on the surface in the Al-Li alloy (Table 1). For an instance, from grain 6 to grain 7, the crack propagated onto the ($\bar{1}11$) plane which had α of 21.1°, β of 25.5° and Schmid factor (0.415), despite the ($11\bar{1}$) plane had a smaller angle β (17.8°) and higher Schmid factor (0.449) but larger α (58.2°) in grain 7.

As shown in Figure 3.2, the crack also branched at GB 3/5, in addition to at GB 10/11. Similar as the case at GB 10/11, as discussed in [95], the crack branching at GB3/5 was also due to the selection of the minimum α by the crack at the GB. As illustrated in Figure 3.4 and Table 3.1, crack A at GB 3/5 was along the primary slip plane ($1\bar{1}1$) in grain 5 and had an α of 35°, much larger than that of 2.5° for crack B at the GB. After crack initiation on (001) plane in grain 3, the crack initially propagated onto the ($1\bar{1}1$) plane in the surface region in grain 5 due to a higher resolved shear stress on this plane, but soon was arrested because of higher resistance due to higher α of 35° for crack A at GB3/5 as it tried to propagate deeper. It re-started on the ($\bar{1}11$) plane that had a much smaller α, 2.5°, i.e., much smaller resistance to crack growth at GB3/5. Note that, as listed in Table 3.1, the predicted Schmid factor (0.432) of the ($1\bar{1}1$) plane was slightly smaller, instead of being larger, than that (0.434) of the ($\bar{1}11$) plane in grain 5. This was possibly due to a possible error in the definition of the direction of the L axis in EBSD measurements for determination of grain orientations. This direction could well be several degrees away from the actual load axis, since there was no well-defined reference line available for positioning the sample to align the load axis with the L axis in the EBSD measurement. The sample was aligned roughly by naked eyes on the sample stage prior to the EBSD

measurement. For an example, a deviation of 5° between these axes can change the Schmid factors of the $(1\bar{1}1)$ and $(\bar{1}11)$ planes in grain 5 from 0.432 and 0.434 to 0.461 and 0.386, respectively. As a result, the Schmid factor of $(1\bar{1}1)$ plane in grain 5 could well be the largest under the actual fatigue loading condition. With the new path along the $(\bar{1}11)$ plane, the resistance to crack growth was much smaller, so that the crack could successfully propagate through GB3/5 eventually. This further supported the crystallographic model for short crack growth across a GB(as proposed in [95]).

3.3.1.3 The Effect of GB Tilting

As shown in Table 1, GB3/2 was one of the three GBs where the observed and predicted α and β were inconsistent, respectively. In grain 3, angle ψ of the crack plane was -82.3°, while ψ angles of the four {111} planes ((111), $(\bar{1}11)$, $(1\bar{1}1)$ and $(11\bar{1})$) in grain 2 were -32.7°, -34.8°, 60.3° and 52.7°, respectively, as listed in Table 3.1. The minimum possible α at GB3/2 should then be 37.4° for the plane $(1\bar{1}1)$, assuming that the GB was perpendicular to the sample surface. Such a large twist angle should have caused large fracture steps forming on the crack plane in grain 2, but no fracture steps were observed on the fracture surface in grain 2, as shown in Figures 3(a) and (c) which are SEM micrographs of the same side (B) of the fractured sample but with different viewing angles. This indicated that α for the crack plane in grain 2 was in fact close to zero at GB3/2. Meanwhile, the angle θ of the crack path in grain 2 on the sample surface matched to that of plane $(\bar{1}11)$ instead of $(1\bar{1}1)$, which implied that the crack actually propagated along $(\bar{1}11)$ in grain 2.

Examination of the fracture surface in grains 3 and 2 revealed that GB2/3 was not perpendicular to the sample surface, as evident in Figures. 3.3(a-c), unlike that originally assumed. As shown in Figure 3.3(b) which is the conjugate fracture surface of the region as shown in Figure 3.3(a), there was a faint line between areas 3 and 3' on the fracture surface, though the fracture surface was almost flat over both areas. Although it was impossible to determine the orientation of area 3' experimentally, it was reasonable to believe that these two areas might be associated with two separate grains with grain 3' being completely buried beneath the sample surface, like the grain structure illustrated in Figure 3.3(d). Both

these grains might share a common (001) plane, so that the crack could be initiated on (001) in both grains, since the crack was almost not deflected at GB3/3'. This assumption was reasonable, since the alloy was solid solutionized at 545°C (much higher than the recrystallization temperature 400°C for a typical Al alloy) for 3.8 hrs after hot cross-rolling, about 20% of the alloy was recrystallized. The rest of the alloy was still unrecrystallized with deformed pancake shaped grains due to the addition of Zr to the alloy. Precipitates of $ZrAl_3$ could effectively pin grain boundaries, thereby prohibiting the formation of new grains in this alloy during solid solution heat treatment. The recrystallized grains in this alloy were often small in size and located mainly along the main boundaries of the pancake shaped grains, as shown in Figure 3.5 which illustrates the grain structure on the rolling plane of the alloy. The recrystallized grains often had either cube or Goss orientation which offered a {001} plane perpendicular to the load axis in the rolling direction. Therefore, grain 3' could well be a recrystallized grain, since it was small and part of the crack initiation site on {001} plane.

Since the orientations of the crack planes in grains 3' and 2 were all known and α at GB3'/2 was close to zero because there were no fracture steps formed at GB3'/2, the inclination angle of GB3'/2 could be calculated by tilting the boundary to the position where it was parallel to the intercept line (i.e., line **ad** in Figure 1) of the crack planes in grains 3'and 2. As illustrated in Figure 3.1, α becomes zero when the GB is parallel to the intercept line **ad** of the crack planes in two neighboring grains. Figure 3.6 is the plot of the calculated α vs. GB tilting angle, γ, as defined in Figure 3.3(d), for all the four {111} planes in grain 2. It can be seen in Figure 3.6 that, when the GB is tilted towards grain 2, α between (001) plane in grain 3' and (1$\bar{1}$1) in grain 2 decreases quickly from 37.4° to zero when γ is about 38°. For the ($\bar{1}$11) plane identified as the crack plane in grain 2, GB3'/2 has to be tilted towards grain 2 by 42° for α to be zero. Therefore, the inclination angle, γ, of GB3'/2 should be 42°.

The GB tilting effect was also the reason why there were no fracture steps formed on the crack plane at GB6/7 (Figure 3.7), despite α at GB6/7 was calculated to be 21.1° for the crack plane (i.e., ($\bar{1}$11), as identified in Table 1) in grain 7. By calculating α at GB6/7 as a function of γ for the ($\bar{1}$11) plane in grain 7, the inclination angle, γ, was identified to be 24° for α to be zero (i.e., no fracture steps were formed on the ($\bar{1}$11) plane in grain 7). As

shown in Figure 3.7, GB6/7 indeed was inclined towards grain 6, as calculated. These results demonstrated that the orientation of a GB can also influence the value of α significantly, in addition to the orientations of the two neighboring grains. Although it is difficult to determine the orientation of a GB that is beneath the sample surface in experiment, it is still possible to study or simulate the crack growth across an inclined GB numerically, since the geometry and orientation of GBs could be controlled in a computer simulation, thereby the growth behavior of a short fatigue crack can be studied and understood in a more complex grain structure than the layered one used in this work.

3.3.1.4 The Effect of the Secondary Grain Boundaries beneath the Surface

Crack deflection inside individual grains was also observed in grains 1 and 15, respectively (Figure 3.2). Figures 3.3(b) and 3.7 show the corresponding fracture surface of the deflected crack in these grains, indicating that there was a large fracture step generated just beneath the location where crack deflection occurred in grains 1 and 15, respectively. These fracture steps were likely to be formed as a result of the existence of oblique GBs completely buried beneath the surface. Although invisible from the surface, these GBs could alter the path of the crack on the surface, since they were close to the surface, about 15~20 μm beneath the surface as in the case of grain 1. As discussed in the above section, there were certain GBs that were not perpendicular to the sample surface in this alloy. These GBs were named as secondary GBs here, to differentiate them from the major GBs which were perpendicular to the surface and parallel to the load axis. The secondary GBs could be the GBs in the bottom parts of grains in the L-S sample surface. It was possible that some grains could have shallow secondary GBs beneath the surface, since they were intercepted by the surface in their bottom halves, like grains 1 and 15. Alternatively, these oblique GBs could be the boundaries of the smaller recrystallized grains that were in the surface region. Such a GB could lead to crack deflection inside a grain on surface, if it is just buried beneath the surface in the grain. The formation of large fracture steps (Figures 3.3(b) and 3.7) could be the evidence for the existence of these GBs in the subsurface of grains 1 and 15.

In the case of grain 1 (Figure 3.7), the crack was initially formed at GB2/1 along $(11\bar{1})$ which had the smallest α (10°) at GB2/1 among the four slip planes, as shown in Table 3.1.

The crack generated along $(11\bar{1})$ on surface soon encountered the shallow secondary GB which could alter the crack path on surface. Consequently, the crack was deflected along (111) in grain 1 since the crack path on surface could be dominated by the large subsurface grain (i.e., grain 1' in Figure 3.3(d)) after the crack propagated into this large grain under the surface. As a result, a large fracture step was produced in the fracture surface (Figures 3.3 and 3.7). This explanation is supported by the crack growth rate measured on the surface of grain 1 that the crack was retarded before being deflected inside grain 1 (Figure 3.8), as will be discussed in next section.

Observation of multiple crack deflections within individual grains in the L-T sample (i.e., sample surface was parallel to the rolling plane) of the same alloy supported the suggestion that the existence of secondary GBs beneath the surface was responsible for crack deflections inside grains (Figure 3.5(b)). In this sample, the major planar GBs were approximately parallel to the surface and the first such a GB from the surface should be about the average thickness of the pan-cake shaped grains, i.e., 26 μm. A fatigue crack with the size of an average grain (about 200 μm) on the surface would interact with about 3-4 such GBs beneath the surface, assuming the crack has a semi-circular shape. Each of these GBs might cause crack deflection on the surface, thereby giving rise to multiple crack deflections within a grain on the surface of the L-T sample, as shown in Figure 3.5(b).

3.3.2 Growth Rate Variations

The effective growth rates of the two tips of the crack shown in Figure 3.2 were measured along the S-direction on the surface after it was found at 7×10^5 cycles. As shown in Figure 3.8, the growth rates of the two tips varied markedly and were profoundly non-symmetrical with tip 2 growing much faster than tip 1. Inside some coarse grains, such as grains 8, 11 and 13, the crack growth rate reached the peaks, though the peak values and locations varied significantly (Figure 3.8). In grain 8, the growth rate was increased steadily before the crack encountered the next GB, while it reached its peaks roughly in the middle of grains 11 and 13, respectively. Inside some other coarse grains, including grains 10, 15 and 1, however, the crack was retarded significantly (Figure 3.8). Furthermore, the crack was retarded to different degrees at different GBs in terms of growth rate (Figure 3.8). For

example, at GBs2/1, 10/11 and 13/15, the crack still maintained a non-zero growth rate, while it was retarded at GBs 7/8 and 15/16 for a period of time (Figure 3.8). These observed variations in crack growth at GBs and inside coarse grains could hardly be explained using a 2-D model (e.g., the one reported in [117, 118]), since it could only predict a decrease in crack growth rate at a GB and an increase after the crack passed the GB on surface. These variations could be accounted for by the 3-D effects of the local microstructure, i.e., the crack growth was dominated by α, β, Schmid factor, GB geometry and subsurface GBs, ahead of the crack tip. For example, since α was different at each GB, the crack growth rate could be different at the GB and inside a coarse grain as well.

In grain 8, the relatively small α (1.7°) for the crack plane allowed steady increase in crack growth rate as the crack grew deeper since the driving force ΔK increased with crack growth, while the resistance was small (Figure 3.8). The observed peaks in grains 11 and 13 were likely to be due to α (0.7° and 6.5°) being small at GBs10/11 and 11/13, respectively, and large Schmid factors (0.443 and 0.49) of the slip planes on which the crack propagated in these grains, since the resistance due to crack plane twist was minimal and the driving force was relatively high for the crack. As described in [95], at GB10/11, a crack was firstly generated along the primary slip plane (111) that had an α of 7.2° and a Schmid factor of 0.438 in grain 11. Because of the relatively small α and large Schmid factor, the crack could still maintain a rate of about 0.8 nm/cycle in grain 11 after the crack passed GB10/11 (Figure 3.8). However, because there was another plane ($\bar{1}$11) that had an even smaller α (0.7°) and also a high Schmid factor (0.443), the crack was branched eventually along ($\bar{1}$11) plane at GB10/11. The branched crack could then propagate much faster, at about 4 nm/cycle, on ($\bar{1}$11) in grain 11, leading to a peak in growth rate in grain 11. The high growth rate peak (8.5 nm/cycle) observed in grain 13 was attributed to the combination of low α (6.5°) at GB11/13 and crack branching inside grain 11. Since the crack was arrested at GB11/12, it was branched inside grain 11. Since the branched crack was analogue to a corner crack as it was formed on the old crack plane, it could grow much faster than a surface crack, leading to the high growth rate observed inside grain 13 despite of α being 6.5° at GB11/13 (Figure 8). The crack was then retarded when it reached the bottom of the main crack in grain 11. Assuming the main crack was in a semi-circular shape, the crack length along its main axis before branching was about 133.3 μm (Figure

3.2) and the distance between the branching point and the crack tip at GB11/12 was 6.7 μm. The depth of the main crack at the branching point could then be estimated to be 29 μm. If the branched crack profile was in a quarter-circular shape, the crack could roughly grow for about 29 μm before encountering the bottom of the main crack. The actual crack depth at the branching point could be slightly smaller than 29 μm since the shape of the main crack front might be a semi-ellipse rather than a semi-circle, as reported in the literature. The integral of the growth rate peak over number of cycles was calculated to be about 26 μm, which supported the above analysis.

In grain 1, the crack grew initially at a rate of 0.5 nm/cycle along the primary slip plane $(11\bar{1})$ which had the smallest α of 10° at GB2/1, but soon retarded with a growth rate of almost zero, followed by a sharp increase in growth rate up to 3.2 nm/cycle at the deflection point. Subsequently, the crack propagated at the growth rate less than 0.4 nm/cycle along the deflected path (111) (Figures 3.8 and 3.2). This variation of growth rate was due to the existence of a shallow oblique GB beneath the surface of grain 1, as discussed earlier. Before the crack deflected inside grain 1, the crack tip was retarded by the more resisting secondary GB beneath the surface, building up elastic energy in the vicinity of the crack tip due to the high resistance from the GB. Once the crack plane was deflected onto $(11\bar{1})$ in surface grain as a result of this secondary GB, the crack growth could accelerate duo to release of the elastic energy, i.e., there was a peak in measured growth rate curve of the crack the location of the crack deflection in grain 1 (Figure 3.8). The crack then re-started on (111) plane at a growth rate of less than 0.4 nm/cycle afterwards, due to the large fracture steps formed beneath the surface and large twist angle for the crack under the surface (Figure 3.3(b)). Similar as the case in grain 1, a subsurface GB beneath the surface of grain 15 was likely to be the reason for causing the decrease in crack growth rate inside grain 15.

In grain 10, the crack growth rate curve had a "U" shape, i.e., the growth rate decreased inside the grain after the crack passed the GB8/10 and increased towards GB10/11 (Figure 3.8). As shown in Figure 3.7, the first fracture step was about 10 μm beneath the surface. This meant that the crack could initially propagate at a non-zero rate for a certain distance before the first fracture step had to be formed beneath the surface, since fracture step formation at GB8/10 presented significant resistance to crack growth. The formation of the

fracture steps dragged the crack growth on surface, thereby leading to crack retardation on the surface, namely, the crack growth rate became zero inside grain 10 (Figure 3.8). After these fracture steps were formed at GB8/10, the crack could propagate at a non-zero rate on the surface again, since the resistance to crack growth was reduced due to the formation of fracture steps on GB8/10 was completed beneath the surface.

Grain size could also play an important role in controlling the crack growth rate on surface. The larger a grain was, the broader the growth rate peak could become inside the grain unless there was a subsurface GB interfering with the crack in the grain. For example, in grain 11 which was relatively large, the peak of crack growth rate was broad inside the grain (Figure 3.8), because of a small α (0.7°) at GB10/11 and no subsurface GB beneath the surface. In contrast, there were no broad peaks in growth rate inside grains 2 and 15 because of the GB 3-D effect, though they were large in size as well. Fine grain size could give rise to higher GB density and more significant 3-D effects of GBs on crack growth in the alloy. This may explain why the growth rate of a short crack in a fine grain material is lower than in a coarse grain material, as observed in Al-Mg alloy and pure Ti for example [171, 172]. Therefore, a finer grain structure is desirable in order to enhance the resistance fatigue crack growth in an alloy. These 3-D effects of the local microstructure on short crack growth behaviours could account for the marked fluctuation in short crack growth. A long crack, unlike the short crack that could interact with only several grains, interacts with many GBs along its front, so that its growth behaviours could be regarded as being controlled by the average microstructures, thereby resulting in a growth rate with less fluctuation in the alloy.

3.4 Discussion

As discussed above, the observed crack path and growth rate from this work supported the crystallographic model proposed earlier for crack deflection and retardation at GBs in the Al-Li 8090 alloy [95]. The crack path and growth rate were a function of several factors such as α and β angles of crack plane deflection at a GB, Schmid factor of the slip plane and grain shape and size in the Al-Li alloy. α appeared to be the main factor that dictated the crack path and could significantly affect the crack growth rate. A GB with a large α angle could cause the tip of a crack to be retarded significantly or branched or

even arrested. The further evidence for the α effect on crack growth could be found in Figure 3.9 where fracture steps were also formed due the twist of the crack planes in the neighboring grains when a crack propagated through their GB vertically along the GB plane in an AA2099 Al-Li alloy. Similar to the crack propagation perpendicularly across a GB, the formation of fracture steps on the fracture surface minimized the total area of fracture on the GB in Figure 3.9, so that both crack planes across the GB were roughly parallel to each other. The side surfaces of fracture steps were likely to be secondary slip planes because the short cracks always follow the slip plane in typical planar slip materials, such as Al-Li alloys and Ni-Al alloys [173]. The formation of fracture steps, although on a small scale, was also observed in Ni-based alloy [107]. The size and spacing of these steps depended on the value of α. The larger the α is, the larger and denser these steps are. The formation of these steps presented major resistance to crack growth across the GB vertically.

Each GB interacting with the crack front could contribute to the resistance to crack growth. The reason why a short crack could become non-propagating is likely to be attributed to the crack encountering several GBs with high resistance along its front in 3-D. When the driving force is equal to or less than the total resistance from these GBs, the crack is arrested. This phenomenon was not fully understood before, mainly because the effects of subsurface GBs could not be studied experimentally as it is almost impossible to measure the crack growth in 3-D and to characterize the crystallographic orientations of those grains that interact with the crack. A more realistic microstructurally-based model needs to be developed for quantification of short growth behaviour in engineering alloys. Such a model allows further understanding of short crack growth in 3-D quantitatively in alloys.

The value of α at the first GB that a crack encounters is a critical factor that controls the growth behavior of the crack, since the initial driving force for such a micro-crack (i.e., a crack initiated within one grain) is relatively small due to the crack size being small. As reported previously, multiple parallel cracks were initiated preferably along the {111} planes in individual Goss oriented grains in a hot extruded AA8090 Al-Li alloy [87]. Most of these cracks could not propagate through the first GBs they encountered in the alloy, which indicated that the resistance of the boundaries between the Goss grains and their neighboring grains to crack growth was sufficiently high to arrest these cracks at the

GBs. In this work, cracks were initiated predominantly perpendicular to the load axis in grains with its <001> being parallel to the load axis in the Al-Li alloy (Figure 3.2). The resistance from the first GBs to the growth of a vertical micro-crack can then be analysed by calculating α as a function of the orientation of the neighboring grain. As shown in Figure 3.10(a), it was assumed that the initial crack was vertical to the sample surface and perpendicular to the load axis in grain 1, and that the GB was vertical to the surface and along the load axis. This was similar as the crack in grain 3. α angles of this crack plane with all the four slip planes in grain 2 with a specific orientation were then calculated on the GB plane and the minimum value was selected. Since the grain orientation could be defined as a point in Euler space, the minimum α as a function of the grain orientation could be represented by a series of plots of α vs. Euler angles, φ_1, Φ, φ_2, as shown in Figure 3.10(b) where φ_1, Φ, φ_2, vary from 0 to 90°, respectively, to cover all the possible orientations and the value of α is shown in a rainbow color scale. Each square in Figure 3.10(b) represents a φ_1-Φ section where φ_1 and Φ range from 0 to 90° while φ_2 is constant with an interval of 5° between successive sections. The darkest blue represents α <5° and deep red represents α>45°. The positions of the commonly occurring texture components, such as brass, copper, S, cube, Goss, r-cube and P, in Al alloys are also superimposed in Figure 3.10(b).

It can be seen in Figure 3.10(b) that, if grain 2 has one of the typical deformation orientations, such as brass, copper and S orientations, the micro-crack is expected to have a minimal resistance to propagate into this grain, as α<5°. If the grain has a recrystallization texture, such as, cube or rotated cube, the crack will be greatly retarded or even arrested when trying to propagate into the grain. In the case of GB5/3, grain 5 had φ_1=61.2°, Φ=83.7°, φ_2=33.4°, which defined a point close to S orientation that gave rise to a very small α for the crack at GB3/5 (Figure 3.10(b)). This was consistent with the observed result in Table 3.1. The micro-crack in Figure 3.10(a) was similar as those cracks initiated: 1) in coarse particles in Al alloys since the cracks are perpendicular to the load axis [167]; and 2) on {111} planes in a Goss oriented grains in the Al-Li alloy as reported in [87], since the intercept lines of these {111} planes are vertical to the sample surface on GBs. The crack arrest observed at the first GBs of these Goss grains might be because the grains adjacent to the cracked Goss grains had a cube orientation. This was

highly possible since the alloy reported in reference [87] had a strong <100> fiber texture that mainly contained Goss and cube orientations, thereby most grains adjacent to the Goss grains where crack initiation took place were likely to be cube grains. As a result, the micro-cracks in the Goss grains were retarded or arrested due to large α at the first boundaries they encountered. Such α-Map might also be regarded as a resistance map, useful for alloy design. With the knowledge of the preferred crack orientation in the initial grains and the GB orientation, an α-Map, i.e., can be plotted for the crack to propagate through the GB. The grain structure can be engineered, if possible, in such a way that each of their GBs provides a large α, in order to maximize the resistance to fatigue short crack growth in an alloy. The large α will retard or even stop the crack advance and eventually increase the fatigue properties of the alloy.

3.5 Conclusions

The twist components of crack deflection at GBs along the crack front were the key factor controlling the short path and growth rate in an AA8090 Al-Li alloy. The smaller α, the faster the crack grew. In addition to the crystal orientation of grains, the tilt of the GB plane could also profoundly influence α, thus affecting the resistance to crack growth. The twist components of crack deflection at GBs also allowed explanation of the phenomena associated with the anomalous growth behaviours such as deflection and branching at GBs and inside grains, non-uniform growth, and retardation, as often observed experimentally, since the 3D effects of GBs could be taken into account in understanding these behaviours. The observation of the formation of fracture steps when a crack propagated along a GB further verified that α dominated crack growth across GBs in planar slip alloys. α-map could be a useful tool for identifying the orientations of the neighbouring grains for higher resistance to crack growth through the boundary with the grain containing a short crack, and for alloy design for optimum resistance to crack growth.

Table 3.1 θ, ψ and Schmid factor of all the possible slip planes in each grain that the crack had propagated through, together with measured θ of the crack. The Euler angle (unit: degree) of each grain are listed under grain name in the sequence of $\varphi_1, \psi, \varphi_2$.

Grain #	Slip planes	θ (°) P*	θ (°) M**	ψ (°) P*	m		Grain #	Slip planes	θ (°) P*	θ (°) M**	ψ (°) P*	m	
Grain1 -30.6 96.5 36.4	111	**17.6**	**19**	**-20.2**	**0.2**	✓	Grain 10 -3.3 92.5 67.1	111	-20.3		-23.4	0.251	
	$\bar{1}11$	86.8		-84.5	0.11			$\bar{1}11$	65.4		-50	0.499	
	$1\bar{1}1$	65.5		24.7	0.338			$1\bar{1}1$	**70.4**	**70**	**55.4**	**0.48**	✓
	$11\bar{1}$	-22	-35	-44.8	0.263	X		$11\bar{1}$	-23.4		32.7	0.313	
Grain 2 -78.7 87.2 -85.2	111	-43.3		-32.7	0.391		Grain 11 84.0 92.7 80.9	111	**-55.9**	**-57**	**48.2**	**0.438**	✓X
	$\bar{1}11$	**33.6**	**34**	**-34.8**	**0.361**	✓		$\bar{1}11$	**40.7**	**39**	**54.7**	**0.443**	✓
	$1\bar{1}1$	-49.9		60.3	0.468			$1\bar{1}1$	-41.2		-45.8	0.427	
	$11\bar{1}$	50.1		52.7	0.473			$11\bar{1}$	43.6		-33.9	0.371	
Grain 3 82.3 93.4 32.5	111	72.6		43.1	0.456		Grain 12 28.2 93.9 32.2	111	-31.2		44.2	0.39	
	$\bar{1}11$	31.1		-63.8	0.402			$\bar{1}11$	71.6	73	-25.3	0.37	X
	$1\bar{1}1$	-40.1		81.9	0.459			$1\bar{1}1$	77.2		82.9	0.219	
	$11\bar{1}$	-73.3		-28.6	0.38			$11\bar{1}$	6		9.2	0.077	
Grain 3 82.3 93.4 32.5	100	-15.1		9.9			Grain 13 24.7 98.2 73.5	111	52.1		-24.1	0.359	
	100	1.6		2.5				$\bar{1}11$	-11.3		-15	0.146	
	001	**86.6**	**86**	**-82.3**		✓		$1\bar{1}1$	**-45.4**	**-47.5**	**54.7**	**0.49**	✓
								$11\bar{1}$	61.6		79	0.421	
Grain 5 61.2 96.3 56.6	111	-83.7		65.3	0.336		Grain 15 -59.2 130.0 -88.6	111	15.9		24.6	0.2	
	$\bar{1}11$	**30.5**	**30.5**	**-79.8**	**0.434**	✓		$\bar{1}11$	81.3		-22.9	0.292	
	$1\bar{1}1$	-34.4	-35.5	-47.3	0.432	X		$1\bar{1}1$	**-24.8**	**-26**	**38.5**	**0.314**	✓
	$11\bar{1}$	24.2		-6	0.088			$11\bar{1}$	85.3		86.4	0.093	
Grain 6 29.4 27.1 81.2	111	**35.4**	**34.5**	**85.6**	**0.472**	✓	Grain 16 58.5 147.1 58.1	111	86	83	47.9	0.497	X
	$\bar{1}11$	38.4		-14.1	0.2			$\bar{1}11$	-25.6		-20.2	0.266	
	$1\bar{1}1$	-33.8		-46.4	0.427			$1\bar{1}1$	64.8		-62	0.472	
	$11\bar{1}$	-75.6		59	0.417			$11\bar{1}$	**-12.6**	**-13.5**	**30.9**	**0.195**	✓
Grain 7 76.5 76.5 88.8	111	-39		49.5	0.458		Grain 19 -12.7 62.1 81.0	111	**-40**	**-41**	**-53.9**	**0.47**	✓
	$\bar{1}11$	**61.6**	**60**	**64.5**	**0.415**	✓		$\bar{1}11$	42.4		-17.6	0.244	
	$1\bar{1}1$	-21.6		-23.4	0.235			$1\bar{1}1$	31		79.9	0.435	
	$11\bar{1}$	52.3		-36.2	0.449			$11\bar{1}$	-79.2		54.7	0.429	
Grain 8 -13.5 98.3 -72.3	111	-30.6		52.3	0.416		Grain 17 -25.8 53.7 7.3	111	**29.4**	**27**	**-73.6**	**0.423**	✓
	$\bar{1}11$	**71.4**	**70**	**62.8**	**0.412**	✓		$\bar{1}11$	-34.3		-49.8	0.435	
	$1\bar{1}1$	52.2	50.5	-41	0.474	X		$1\bar{1}1$	-86.2		66.1	0.329	
	$11\bar{1}$	-18		-15.4	0.181			$11\bar{1}$	24.4		-4.7	0.07	

*P-predicted value **M-measured value   ✓-crack propagating   X-crack arrested

73
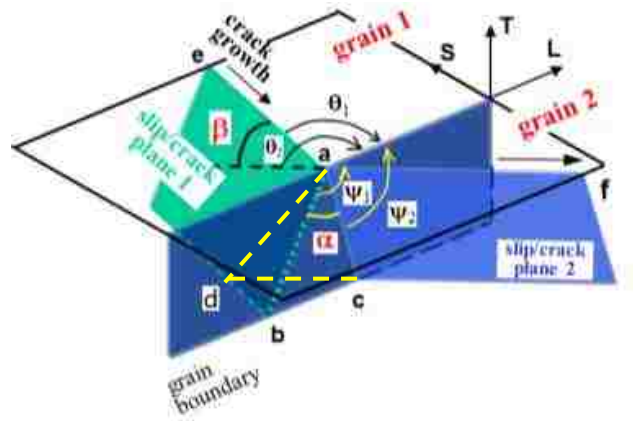
Figure 3.1 Schematic diagram showing a crystallographic mechanism for crack growth along slip plane 1 in grain 1 onto slip plane 2 in grain 2. The crack growth across the GB is controlled by α and β (after [95]). **ad** is the intercept line of crack planes 1 and 2.
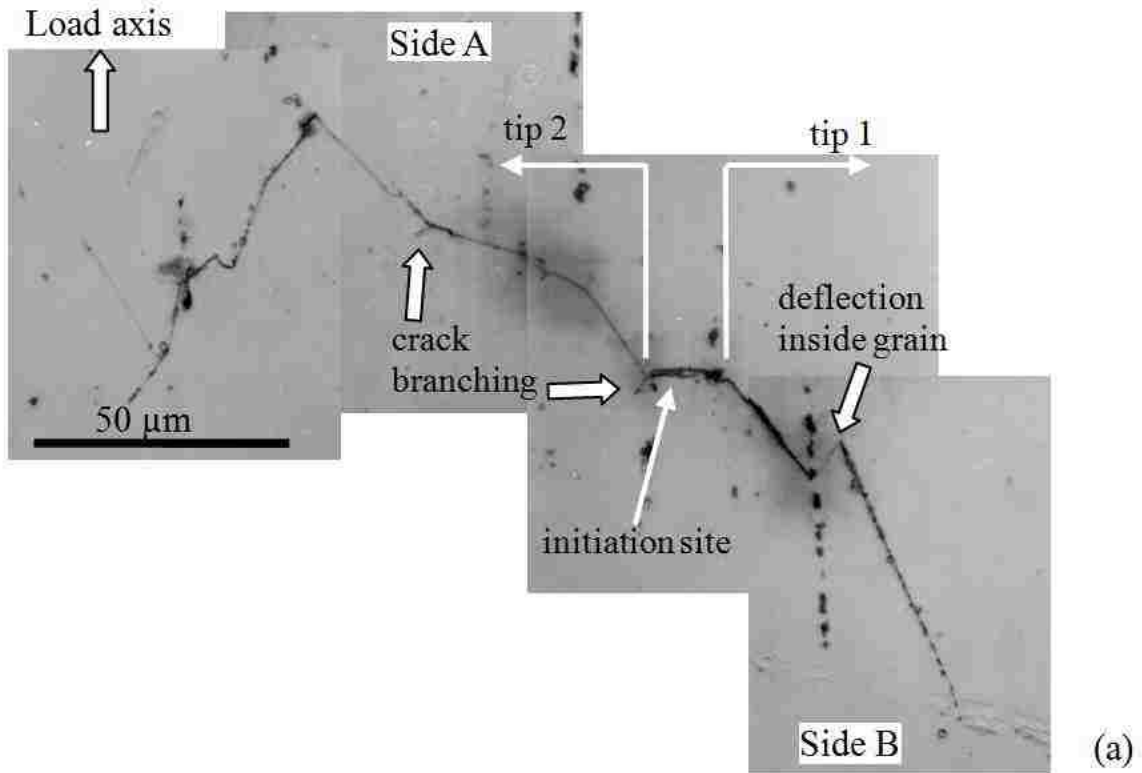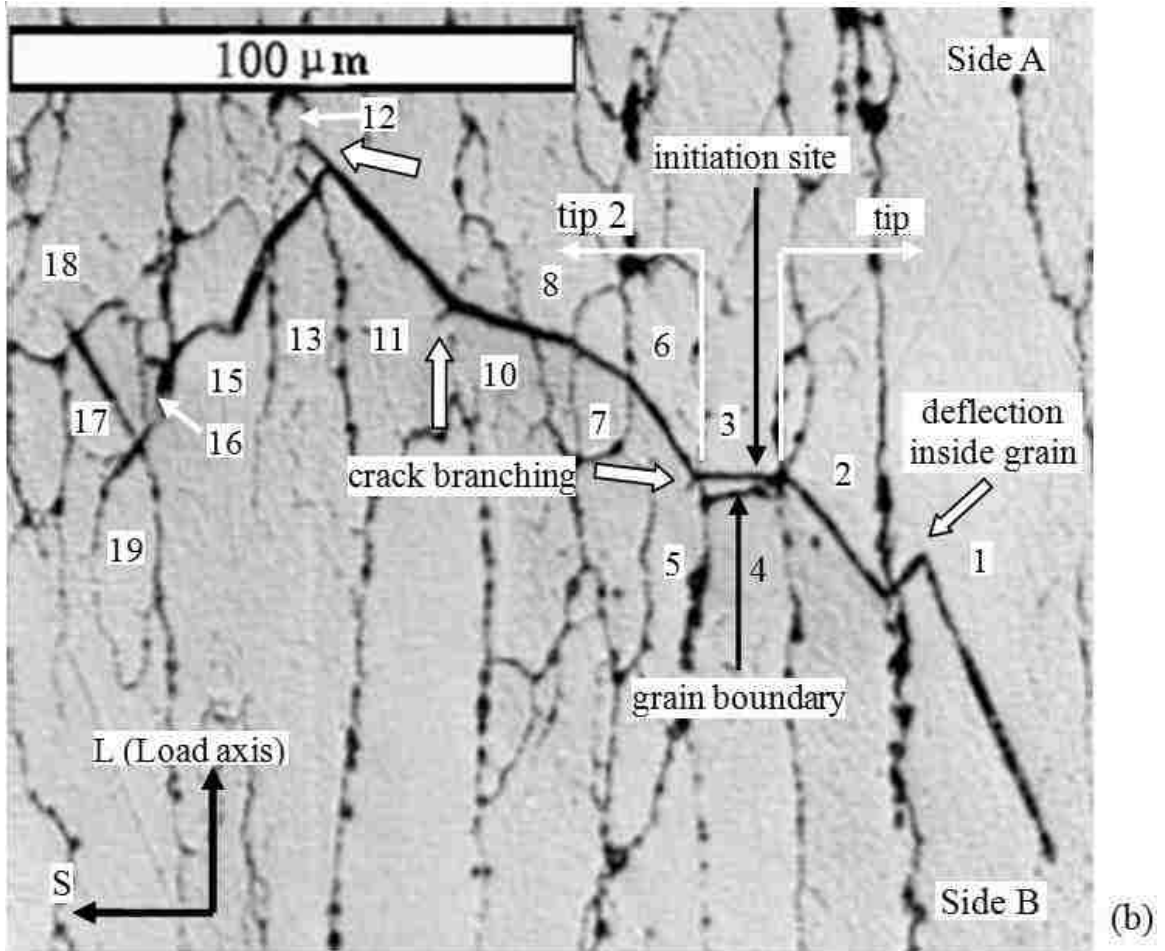
Figure 3.2 (a) SEM micrograph of a short fatigue crack in Al-Li 8090 alloy before etching; (b) Optical micrograph of the same crack after etching. 9.15×10^5 cycles.
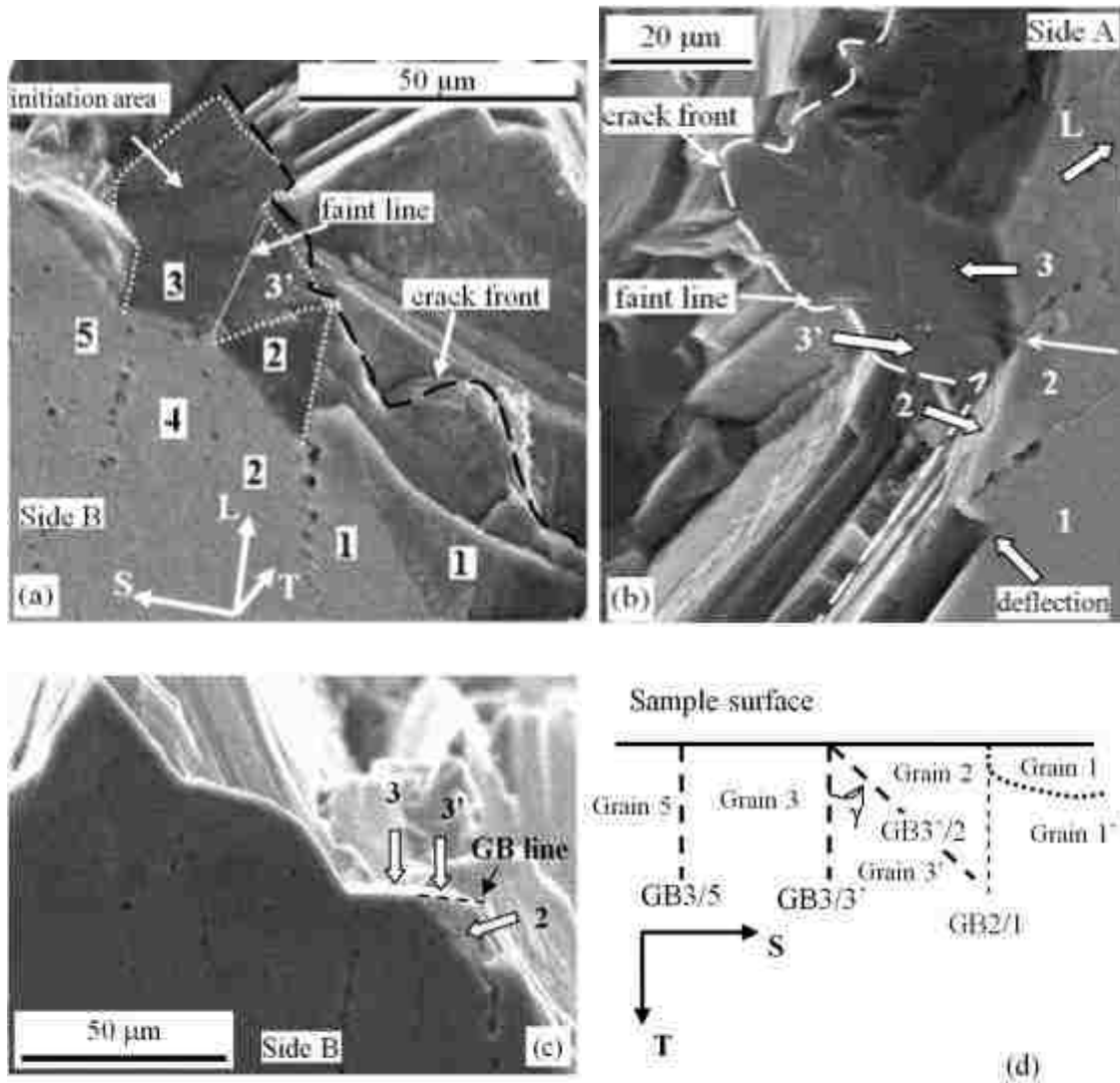
Figure 3.3 (a) & (b) SEM micrographs of the two conjugate fracture surfaces (sides B and A) of the crack shown in Figure 2; (c) SEM micrograph of the fractured sample (size B) when the sample surface is perpendicular to the viewing angle. (d) A sketch of the grain structure around the crack initiation site on the cross-section perpendicular to the load axis.
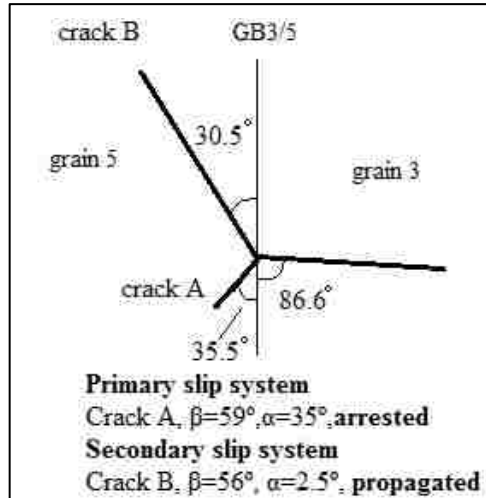
Figure 3.4 Schematic diagram showing the twist α and tilt β angles of branched crack at GB3/5.
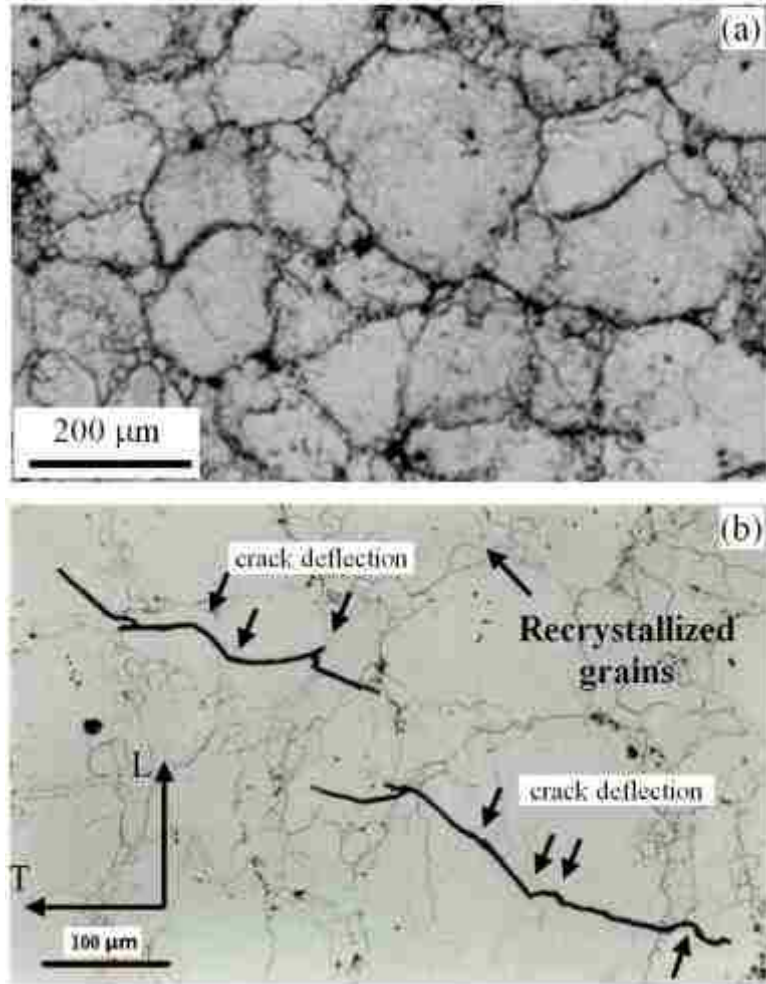
Figure 3.5 Optical micrographs showing: (a) clusters of fine recrystallized grains along the unrecrystallized grain boundaries and (b) crack deflections inside the coarse unrecrystallized grains in an Al-Li 8090 sample. Arrows indicate crack deflections within grains.
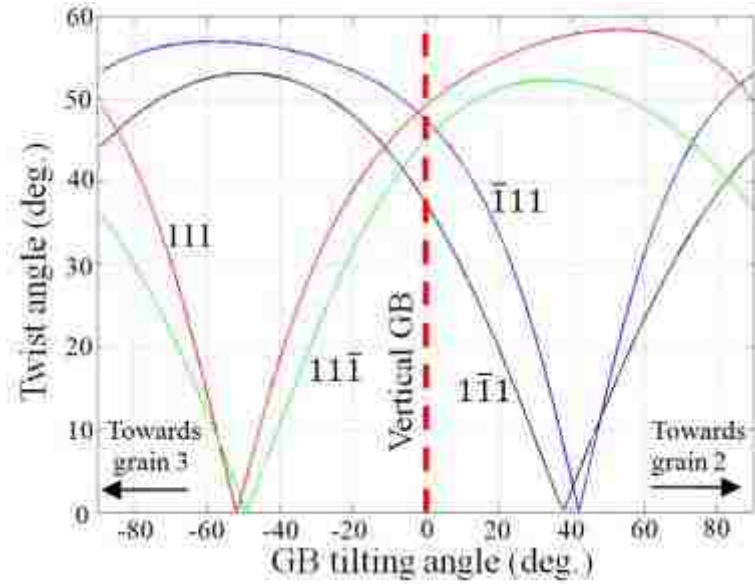
Figure 3.6 Plot of twist angles for all four slip planes in grain 2 as a function of GB tilting angle at GB3'/2.
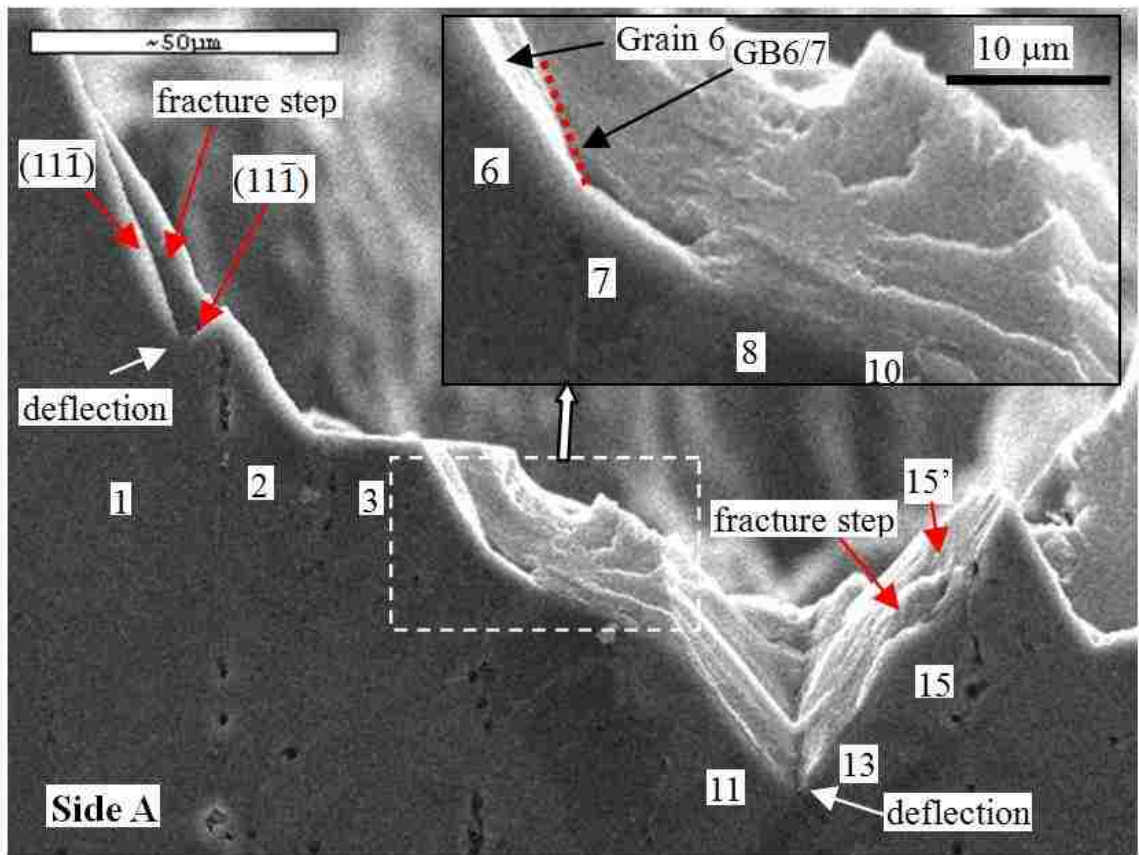
Figure 3.7 SEM micrograph of the crack shown in Figure 3 after being fractured. GB6/7 is tilted towards grain 6 from the vertical position.
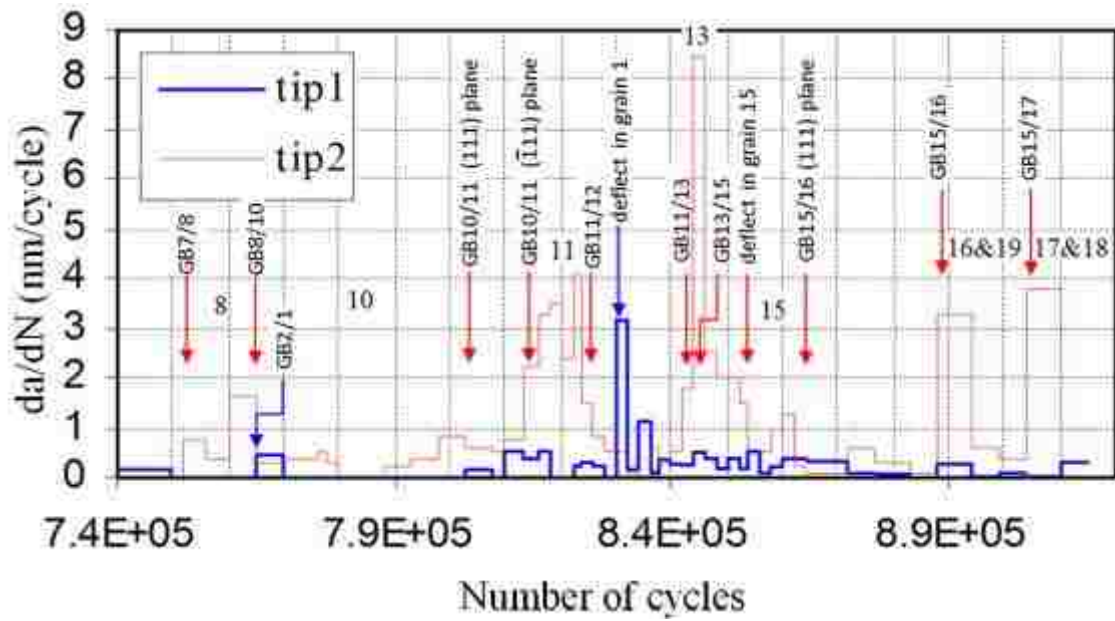
Figure 3.8 Crack growth rates of the two crack tips.
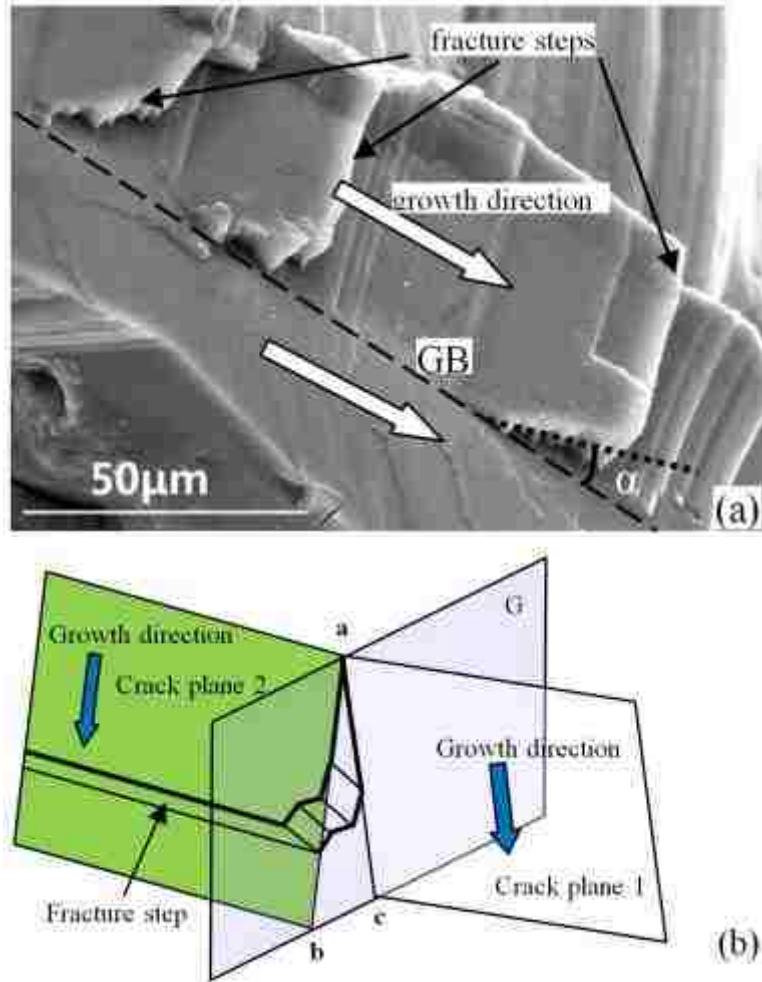
Figure 3.9 (a) Fracture step formation when a fatigue crack propagates along a GB in an AA 2099 Al-Li alloy (b) sketch of the formation mechanism for the fracture steps.
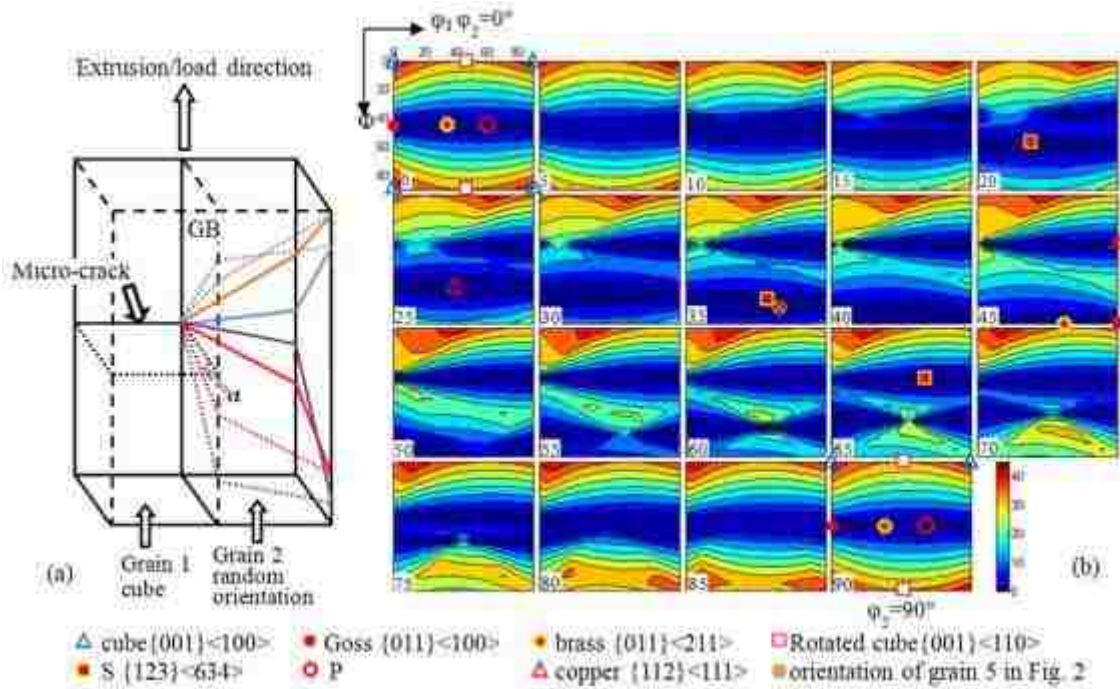
Figure 3.10 (a) Schematic diagram showing orientations of two neighboring grains for calculation of α at GB. The micro-crack is initiated on one {001} plane vertical to loading axis in cube grain 1. Grain 2 has a random orientation. The dot-line planes represent crack plane and {111} planes in grain 1and grain 2, respectively. (b) α-Map at GB between cube grain 1 and a randomly orientated grain in Euler space superimposed with typical texture components. The value of φ_2 of each section is labeled at the bottom-left corner.

Chapter 4 Experimental Quantification of Resistance of Grain Boundaries to Short-Fatigue Crack Growth in 3-D in Al Alloys

In Chapter 3, it has been illustrated that the twist component of crack deflection at GB is the key factor controlling the crack path and GB-resistance against crack propagation. The minimum-α criterion has also shown to be capable of predicting the crack propagation path and identifying GB-resistance qualitatively. However, the quantitative relationship between GB-resistance and α has not been established. This chapter proposes an experimental approach to investigate the interaction of crack propagation with selected GBs with a wide range of α quantitatively, and determines that GB-resistance increases as a Weibull-type function of α in high strength Al alloys.

4.1 Introduction

The early stage of fatigue crack growth is of scientific and engineering interest, because it can compromise more than 90% of a component's fatigue lifetime [1]. Being different from long crack stage, the growth of short fatigue crack is sensitive to local microstructure, such as grain boundary (GB), phase boundary, particle, etc. Among these microstructural features, GB has been commonly recognized to be the major barrier to short fatigue crack growth [62, 63, 65, 94] and account for the marked variation of the short fatigue crack growth rate measured in most engineering alloys [66-69]. Over the past decades, numerous efforts have been made in attempt to quantitatively understand the behavior of short fatigue crack growth through GBs. Most of them were based on Bilby-Cottrell-Swinden (BCS) theory, which described the crack and the plastic deformation zone in the vicinity of the crack tip as array of continuously distributed dislocations. In this theory, the process of slip-band blocking by a GB was considered, which was further developed later by Navarro and De los Rios et al [117, 118, 122] by incorporating a Sachs factor averaged over the grains along the crack front for short crack growth simulation. However, these traditional models which are 2-D in essential, do not

directly take into account the local crystallographic orientation and cannot explain short crack behavior, such as branching and deflection at GBs. In the recently decade, the establishment of new characterization techniques makes it possible to investigate the interaction of short cracks with the local microstructure in 3-D. With the aid of electron back scatter diffraction (EBSD) and acoustic microscope, Zhai et al [95, 143, 174] studied the effect of crystallographic geometry of the GBs that interacted with short fatigue cracks in Al-Li alloy and Al-Cu alloy. A 3-D crystallographic model was subsequently proposed that the twist and tilt components (rather than misorientation) of the crack deflection at a GB were the key parameters controlling the growth behaviors of short cracks in planar slip materials. Schaef and Marx et al [107-109], using focused ion beam (FIB) and EBSD, studied the interaction between short cracks and GBs in Ni-based superalloy in 3-D, which yielded the similar results as Zhai's observations in Al alloys. With the development of the combined diffraction and phase-contract X-ray tomography, Ludwig, Herbig and King et al [110-112] were able to obtain an in-situ full picture of the short crack growth in a polycrystalline in 3-D, although the spatial resolution has to be further enhanced in order to observe the crack growth behavior in more details. It was found that the observed interactions between the crack and the polycrystalline microstructure can be explained using Schmid factors and the tilt twist model of Zhai and Wilkinson [111]. These recently work enriched the understanding of the behavior of short crack propagating through GBs, however, it is still lacking that a microstructure-based numerical model to quantify the resistance to short crack growth. As presented in the present paper is an experimental approach to quantify the GB-resistance to short fatigue crack growth. For the first time, it was found that the GB-resistance increases with twist component at the GB, following a Weibull-type function.

4.2 Experiments

4.2.1 Material

The material used in this work was an Al-Cu alloy AA2024-T351 provided in the form of a 7 mm thick sheet which had a pancake shaped grain structure with the average grain size of about $361 \times 97 \times 37$ μm^3 (Figure 4.1). Its chemical composition is shown in Table 1. The yield strengths the alloy were measured to be 346 MPa and 380 MPa in T and L direction, respectively. Samples ($36 \times 7 \times 4.6$ mm^3) for subsequent four-point bend fatigue test were cut with the plane under the tension-tension loading being parallel to the T-S plane (T-transverse direction and S-short transverse direction) and the loading axis being along the T direction. The sample surface under the tensile stress in four-point bend was ground, mechanically polished and etched with Keller's etchant to reveal grain structure before subsequent experimental procedures.

4.2.2 Micro-notches fabricated with FIB

After etching, the grains which were relatively thick (50~80 μm in S direction) and with relatively straight GBs were selected. In the center of each selected grain, a micro-notch with 2 μm in width, 15 μm in depth (in L direction) and 30 μm in length (in S direction) was made with an FEI Quanta 200-3D dual beam SEM/FIB system. The notch plane was made with main notch-plane being either perpendicular or 45˚ to the T direction and the notch-tips being at least 10~25 μm away from the immediate GBs. 68 notches were made in 6 samples and the notches in each sample were sufficient apart (at least 500 μm) from each other to avoid stress shielding effect. As shown in Figure 4.2 are two of such micro-notches for demonstration.

4.2.3 Fatigue Testing and Crack Growth Monitoring

Both the un-notched and notched samples were fatigued using a self-aligning four-point bend rig (Figure 4.3) [145] under a constant maximum stress, at a frequency of 20 Hz, stress ratio R= 0.1 and room temperature in air. The fatigue strength of the un-notched alloy in the T direction was 346 MPa (i.e., the maximum stress), which served as a reference for the fatigue of notched ones. The maximum stress for notched samples ranged from 280 to 346 MPa. The fatigue tests were periodically interrupted to detect short cracks and follow their lengths on the sample surface using an optical microscope at least $500\times$ and an SEM (Hitachi S-4300), respectively. An interval between 1000 to 3000 cycles was chosen, so that the crack tip propagation in both grains and near-GB regions could be monitored continuously.

4.2.4 EBSD Measurement and FIB Cross-sectioning

After the fatigue testing, the crystal orientations of the grains surrounding the cracks were measured with EBSD (Oxford HKL system). At the interested GBs, the area was cross-sectioned perpendicular to T direction to reveal the morphology of the cracks and GBs beneath the surface, using a Hitachi NB5000 dual beam SEM/FIB system. The combined information of grain orientation, traces of crack planes on sample surface and on cross-section surface were used to determine the crack plane orientation in individual grains. Together with the GB morphology, the actual α at each GB was calculated, which will be discussed in more details later.

4.3 Results

4.3.1 Crack initiation

Only 7 micro-notches, out of 68 as made, became the crack initiation sites during the fatigue test. These cracks were detected within the range of 1.8×10^4~6×10^4 cycles. EBSD measurement of the crack-initiation grains showed that these grains were roughly either R-cube or Goss orientated, which is evidently presented in the pole figure and the

corresponding orientation distribution function (ODF) (Figure 4.4). In such orientations, the grains have relatively high Schmid factor, i.e. the grains are "soft" orientated. Actually, the Schmid factor of the crack-initiation grains were measured to be 0.435~0.475, which promoted the crack initiation to occur in these recrystallization-type grains. This is consistent with that the fatigue cracks were prone to nucleated in recrystallized grains in Al-Cu alloy and Al-Li alloy [87, 174].

4.3.2 Short Fatigue Crack Growth Behavior

Upon the cracks being initiated, they propagated crystallographically through 5~8 GBs (until about 150~250 μm in length) before transited to the non-crystallographic growth mode (the present work focuses on the crystallographic growth regime). The crack grew with varying growth rates, especially with decreases at GBs. For example, as shown in Figure 4.5 (a) is the growth behavior of a fatigue crack under the maximum stress of 346 MPa during the fatigue test. The crystal orientations of the grains surrounding the crack, as measured with EBSD, is presented in inverse pole figure mode in Figure 4.5 (b). And in Figure 4.5 (c) the GBs revealed by EBSD mapping are sketched out in the SEM micrograph. The lengths of two crack tips (defined as the distance from the notch center to the crack tip, as measured by projecting the length in the S direction) are plotted against the number of cycles in Figure 4.6 (a), and the growth rate of two crack tips vs. the total crack length is plotted in Figure 4.6 (b). Crack tip 1 was detected at 3.6×10^4 cycles when it was 7 μm long from the notch edge. It propagated straightly about 84° off the T direction in grain G1. It reached a growth rate of ~0.28 nm/cycle before impinging the first GB (GB1/2, the notation of GB i/j means the GB between grains i and j) at around 4.8×10^4 cycles, followed by being arrested for 3000 cycles prior to extending into grain 2. Subsequently, it seemed to "burst" with a growth rate ~0.23 nm/cycle immediately after passing GB1/2, but slowed down to 0.16~0.18 nm/cycle very shortly. As crack tip 1 grew in grain 2, it accelerated gradually to a growth rate of ~0.32 nm/cycle

until being retarded significantly to ~0.06 nm/cycle at around 12.3×10^4 cycles at GB2/3. Afterwards, the crack tip 1 retrieved its original growth rate in about 1.2×10^4 cycles and then propagated with an accelerating speed. On the other side, crack tip 2 was detected at 6×10^4 cycles when it was about 7 μm from the notch tip. The initial growth rate of tip 2 was measured to be ~0.18 nm/cycle. Similar to crack tip 1, it also advanced crystallographically in grain G1, following a path about 84˚ with respect to T direction. As crack propagated, its growth rate increased gradually to 0.32 nm/cycle until reaching GB1/5 where it dropped to 0.21 nm/cycle and then re-increased afterword. After entering the grain G5, the crack tip 2 propagated straightly in an oblique path -57˚ off the T direction. The crack tip 2 re-gained its original growth rate after 2×10^4 cycles, and then it started to grow very fast with an average growth rate of ~1.45 nm/cycle, but followed by a decrease to 0.32 nm/cycle at GB5/6. Beyond GB5/6, it started to propagate non-crystallographically in grain G6. The non-crystallographic growth may be due to that secondary GB beneath the surface could alter the path of the crack on the surface [143]. In the present study, the decrease of the crack growth rate at a GB (Δ(da/dN)) is defined to be the difference of the da/dN before and after passing the GB, which is also demonstrated in Figure 4.6 (b). The measured Δ(da/dN) at different GBs will be correlation with the resistance at GB in the following sections.

4.3.3 Propagation plane of short fatigue crack

With the EBSD measurement of each grain that contained the crack, the slope angle of traces (relative to T direction) of low-index slip planes ({100}, {110} and {111}) on the sample surface could be calculated. Then these slopes were compared with that of the cracks. It was found that most of the cracks were almost parallel, with a deviation-angle less than 2~4˚, to the trace of one {111} plane on the surface, indicating that most crack planes were following one of {111} plane. This is consistent with that the crack planes always followed one of a {111} planes in planar slip type Al alloys, such as Al-Li alloy

[95], Al-Mg alloy [102] and Al-Cu alloy [174]. Sometimes, the slope-angle of the crack path happened to be close to those of more than one slip plane, making it less reliable to determine the crack plane by merely matching the traces on the sample surface plane. For instance, the Euler angle of grain G3 was measured to have $\varphi_1=203.97°$, $\Phi=40.64°$ and $\varphi_2=225.91°$. The slope-angle of slip plane traces θ was calculated to have $\theta_{(111)} = 24.7°$, $\theta_{(\bar{1}11)} = 89.8°$, $\theta_{(1\bar{1}1)} = -40.1°$ and $\theta_{(11\bar{1})} = 27.0°$ (Figure 4.5 (c)), while θ of the crack was measured to be $\theta_{Crack} = 26.3°$ which was very close to those of plane (111) and $(11\bar{1})$. In such a situation, the crack plane trace on the cross-section plane (vertical to T direction) was revealed by FIB to verify on which slip plane the crack was exactly propagating. As demonstrated in Figure 4.5 (d) is the cross-section plane revealed by trenching along the dash line Figure 4.5 (c). Similar to calculating the slip plane trace on the sample surface, the angle (γ) between traces on the cross-section plane and L direction were calculated to have $\gamma_{(111)} = -5.9°$, $\gamma_{(\bar{1}11)} = 89.6°$, $\gamma_{(1\bar{1}1)} = 32.1°$ and $\gamma_{(11\bar{1})} = -77.4°$ (Figure 4.5 (d)). Since the angle γ for the crack path on cross-section plane was measured to be $-4.8°$, thus the crack plane in grain G3 can be determined to be parallel to slip plane (111). In the present work, the determination of crack plane was carried out by matching theoretical slip plane path with crack plane path on surface, and on cross-sectioned surface if needed.

4.3.4 Grain Structure

Since the grains are much longer in L and T directions than in S direction, thus the major fraction of the GB planes could be expected to be almost flat and vertical to S direction. As a fact, the GBs trace on cross-section plane (revealed by FIB) was verified to be vertical to sample surface. For example, it is evident in Figure 4.5 (d) that the GB2/3 is almost straight and vertical to S direction. As shown in Figure 4.5 (e) is another example (GB1/5) of the straight and vertical GBs. Therefore, the GBs were assumed to be vertical

to the surface and the GB tilting effect on α [143] does not need to be considered in this study.

4.3.5 Determination of α at GBs

The value of α at GBs was determined as follows. First, upon the initial crack path (path inside the notched grain) was determined, the theoretical value of possible α could be calculated by α=arcos ([E]×[N$_1$]•[E]×[N$_2$]) [95], where [E], [N$_1$] and [N$_2$] are the unit vectors of the normal of the GB plane, crack plane in the notched grain and the favorite slip plane for crack growth in the neighboring grain [95, 143], respectively. Then the slip plane that the crack grew on in the neighboring grain could be predicted theoretically. Second, this theoretically predicted slip plane was compared with the experimentally observed crack plane to verify if the crack followed a minimum-α path after passing a GB. In this study, the crack indeed followed a minimum-α path within crystallographic growth region and α at each GB was determined.

4.4 Discussion

4.4.1 Resistance *R* vs. *α*

The interaction of the crack growth with 14 GBs was captured successfully in this work, showing that the extent of the crack growth rate drops varied at different GBs. As plotted in Figure 4.7 (a), the Δ(da/dN) at each GB is correlated against the corresponding α, in which the Δ(da/dN) range from 0 to 1.4 nm/cycle while α range from 3.7˚ to 33.2˚. It was found that the data points of Δ(da/dN) at GBs vs. α fell into a band enveloped by two straight dash lines. It is evident that the Δ(da/dN) increases with α linearly although the data points are somewhat scattering due to possible experimental error. When the α is very small, e.g. <5˚, the Δ(da/dN) is relatively insignificant (<0.2 nm/cycle). At some GBs (e.g. the one with α=3.9˚), the crack growth retardation was even too ignorable to be detected in the experiment (Δ(da/dN)=0). When α arises (e.g. >30˚), the Δ(da/dN) increases considerably to 1~1.5 nm/cycle which is one order higher than that in low-α region. In such a high-α region, the cracks were usually held at the GBs for several

thousand cycles before entering the neighboring grains due to the significant resistance of GBs.

Traditionally, the resistance of GB was not taken into consideration in modeling crack growth behavior in classic fracture mechanics. The Paris law (Equation 4.1) or its derivatives contains only the driving force term ΔK, but not resistance term R. Since the scale of a long crack is much larger than the microstructural barriers (such as GB and phase boundary), i.e. the cracked area covers numerous grains, thus the material is traditionally regarded as a homogenous continuous medium. Thereby, the influence of local microstructure on the crack growth can be ignored when compared with the crack growth driving force. Actually, it has been incorporated in power law coefficient, C, and exponent, n, as intrinsic materials properties. For a short crack, however, the fractured area usually covers only a limited number of grains and its growth driving force is relatively small. Thus the influence from the local microstructure played a significant role on crack propagation, i.e. the resistance of GB becomes considerable compared with the crack growth driving force. Such a resistance can obviously decrease the growth rate when a crack is interacting with a GB. Thereby, as reflected in a growth rate curve, the nadir of the growth rate at or shortly after passing a GB, $(da/dN)_{GB}$, can be expressed by Equation4.2.

$$\left(\frac{da}{dN}\right) = C \cdot \Delta K^{m} \tag{4.1}$$

$$(da/dN)_{GB} = \frac{da}{dN} - \Delta\left(\frac{da}{dN}\right) = C \cdot (\Delta K - R)^{m} \tag{4.2}$$

Solving Equation 1 and 2 yields the resistance term R, which could be expressed by Equation 4.3.

$$R = \Delta K - (\Delta K^{m} - \Delta\frac{da}{dN}/C)^{1/m} \tag{4.3}$$

In Equation 4.1~4.3, ΔK is the crack growth driving force before it impinging the GB. It was estimated by $\Delta K = 2\Delta\sigma\sqrt{a/\pi}$ assuming the crack had a semi-circle shaped contour, in which $\Delta\sigma$ is applied far-field stress amplitude and a is the crack half-length as

measured on the sample surface. In this study, the coefficient $C=1.89\times10^{-7}$ mm/cycle and exponent $m=2.73$ were obtained by fitting the Paris region of the long fatigue crack growth in Al-Cu alloy AA2024-T3 [175]. For each GB, the resistant term R could be calculated according to Equation 3. As shown in Figure 4.7 (b), resistant R is plotted against the corresponding α at the 14 GBs as measured in the present study. It was found that R increased slowly when α was relatively small, then raised rapidly when α was within the middle range (12~22˚) before saturated after 25˚. This relation resembles the shape of a two-parameter Weibull type function as expressed by Equation 4.4, where R_f defines the maximum resistance, i.e. the saturation resistance at high α region; α_0 the scale parameter defining the location for the bulk of distribution; and n the shape of the distribution. With the collected data, the distribution of R vs. α could be fitted by Equation 4.5. Despite that the data points at high α region are somewhat scattering due maybe to experimental error, the trend of data match with fitted function well. It is noticed that the R_f was fitted to be 0.9 MP√m, which is a relatively high compared with the driving force of microstructurally or mechanically short cracks. For high strength Al alloys with tensile yield strength of 270~380 MPa (e.g. for 2000, 6000 and 7000 series), the driving force for a crack reaching 500 μm long (conventional length of transition from short crack to long crack) can be estimated to be 4.3~6.1 MPa√m, assuming the crack has semi-circle shape and is loaded under maximum load of yield strength with stress ratio R=0.1. This implies that, even for a crack about to turn into a long one, the GB resistance could reach 15~20% of the nominal driving force. For a crack at very initial stage, like 100 μm long crack, this fraction can even reach to 32~46% of its driving force. Therefore, the resistance of GB played an important role in dominating the early stage of crack growth and is responsible for the scattering of growth rate of microstructurally short crack. This implies that the resistance of GB has to be taken into account in modeling the short fatigue crack growth, which is discussed in spate papers [106, 176].

$$R(\alpha) = R_f\{1 - \exp[-(\alpha/\alpha_0)^n]\} \tag{4.4}$$

$$R(\alpha) = 0.9\,\{1 - \exp[-(\alpha/20.1)^{4.2}]\} \tag{4.5}$$

4.4.2 Microstructural Threshold

In some circumstance that the resistance at the GB is extremely high, the crack tip could be completely arrested by the GB. As shown in Figure 4.8(a) is another example of the growth behavior of another fatigue crack emanated from the notch, under the maximum stress of 346 MPa. The crack tip 1 and 2 were noticed at 5.7×10^4 cycles and 6×10^4 cycles, respectively. Crack tip 1 was determined to follow $(\bar{1}11)$ plane in grain 1, while tip 2 followed (111) plane. Crack tip 2 passed GB1/3 at 6.3×10^4 cycles, followed by propagating subsequently through grain G3 into grain G4 and re-entering grain G3 finally. On the other side, however, crack tip 1 impinged GB1/2 at 6.9×10^4 cycles and then became non-propagating afterwards. At the stage when the tip 1 reached the GB, the crack driving force was about 2.03 MP√m. The calculation showed that the minimum α at GB was very high (α=33.2°), which can render a GB-resistance of about 0.9 MP√m (according to Equation 5) being 44% of the driving force. Such a high resistance could undermine the driving force for crack growth, making significant crack growth retardation. As tip 2 grew, the resistance effect was expected to appear less significant because the driving force rose, so that the crack was supposed to extend into grain G2 after being significantly retarded for a certain number of cycles. In this particular case, however, the GB1/2 was found to debond finally (as revealed by SEM in Figure 4.8 (c)). This may be due to that the stress intensity at the vicinity of crack tip 1 became so large (i.e. 2.7 MP√m when the fatigue test was terminated at 8.1×10^4 cycles) that GB was torn apart. This could happen when the segregation of detrimental trace elements or S phase precipitation along GB resulted from imprecise heat treatment. Once the GB broke its integrity, the local region became non-continuous, so that the stress and strain could not

transfer into the neighboring grain and thus the propagation of the crack tip was ceased. The similar case of crack being arrested at the GB was also found in hot extruded AA8090 Al-Li alloys [87]. As reported, multiple parallel cracks were initiated preferably along the {111} plane in individual Goss-orientated grains. Most of these cracks could not propagate through the first GBs they encountered in the alloy, which indicated that the resistance of the GBs between the Goss grains and their neighboring grains to crack growth was sufficiently high to arrest these cracks at the GBs [143,167]. It can be inferred that the high α GB, especially when it is the 1st GB to the crack, has a critical effect to small cracks, because the growth driving force at this stage is relatively small so that the crack can be easily arrested completely. This mechanism may partially explain the microstructural threshold for short crack growth.

The relationship of GB-resistance vs. α provides a new understanding of the effect of microstructure on short fatigue crack growth. Although the parameters/coefficients in the as fitted relation are material-based, the trend of the relation should prevail in most slip planar materials. The relation of GB-resistance vs. α can be incorporated in the modified Paris law for the development of short crack growth model in 3-D [106]. Also, it can also be used for alloy design in terms of texture optimization because α is a function of texture, which is discussed in details in separate papers [176].

4.5 Conclusion

The interaction of short fatigue crack growth with GB was experimentally observed in an Al-Cu alloy. The growth behavior of a short fatigue crack was mainly determined by the twist component (α) of crack plane deflection at a GB which rendered the resistance to crack growth. Such GB-resistance can render the growth rate drop when the crack is passing a GB. It was experimentally quantified that the GB-resistance to short fatigue crack growth increased with α, following a Weibull type relation. This paper also

presented an approach to quantify the GB-resistance to short fatigue crack growth in planar slip materials.
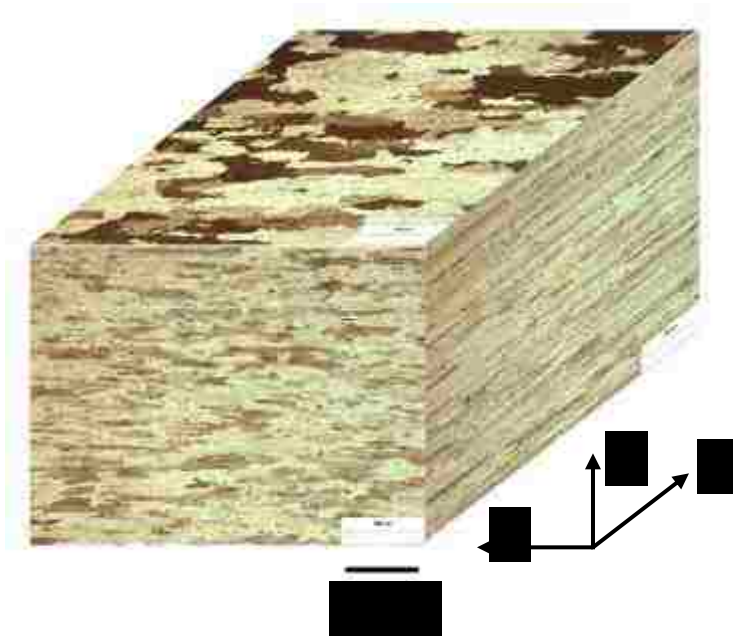
Figure 4.1 Microstructure the Al-Cu alloy AA2024-T351 used in this study, showing pancake shaped grain structure.
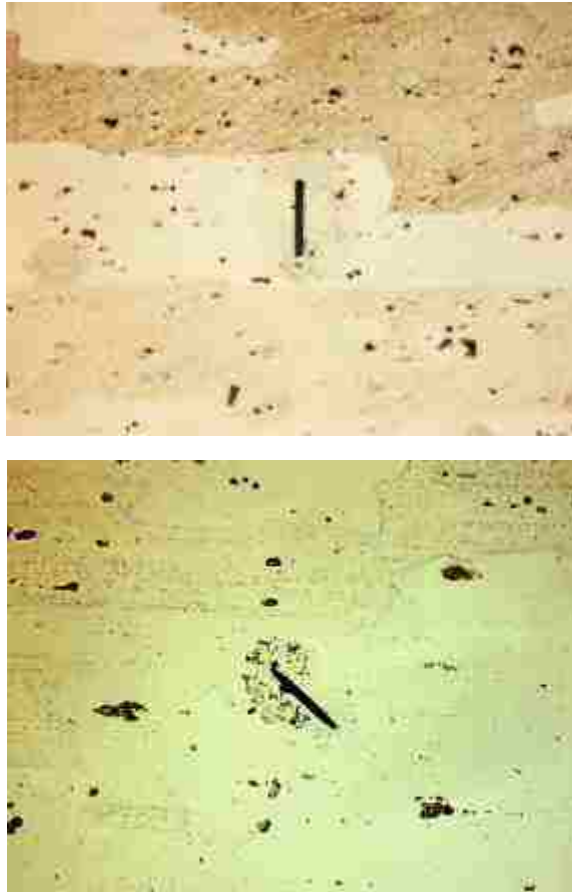
Figure 4.2 Two examples of the micro-notches made with FIB.
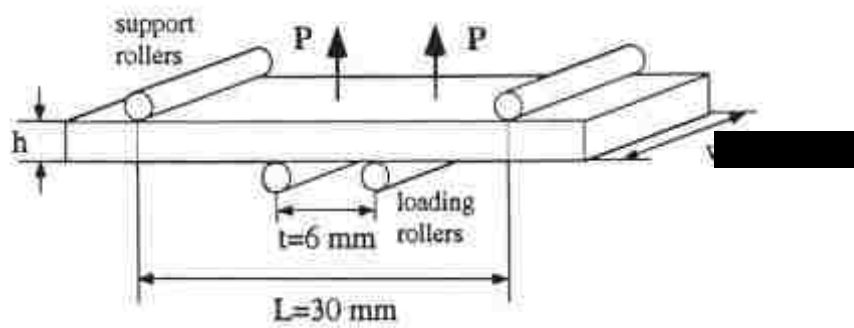
Figure 4.3 Four-point bend specimen geometry and the loading states.
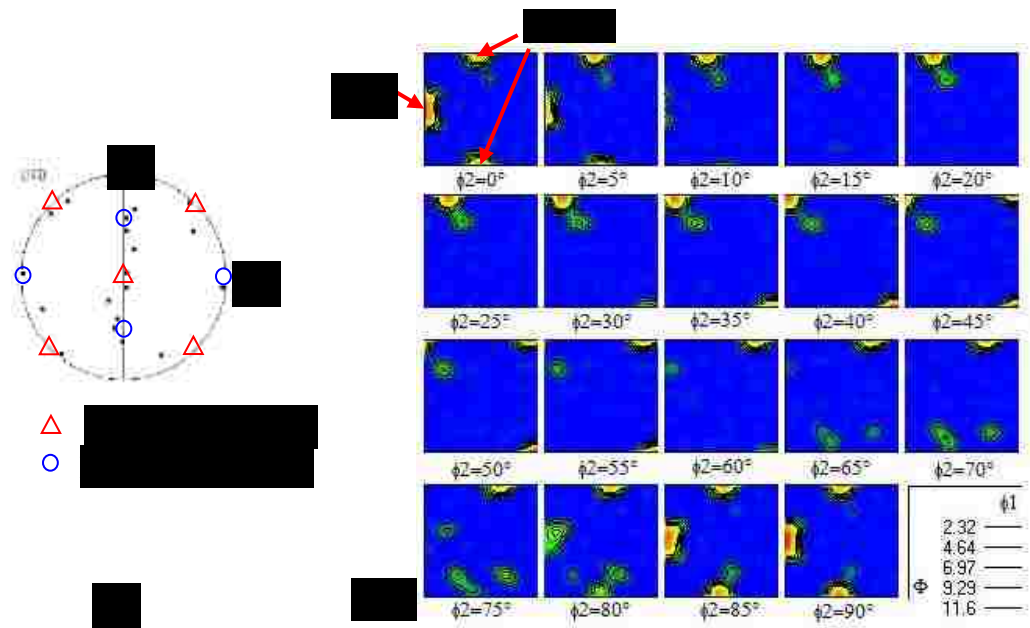
Figure 4.4 Crystal orientation of crack-initiation grains represented by (a) (100) pole figure and (b) ODF.

(a)

(d)

(e)
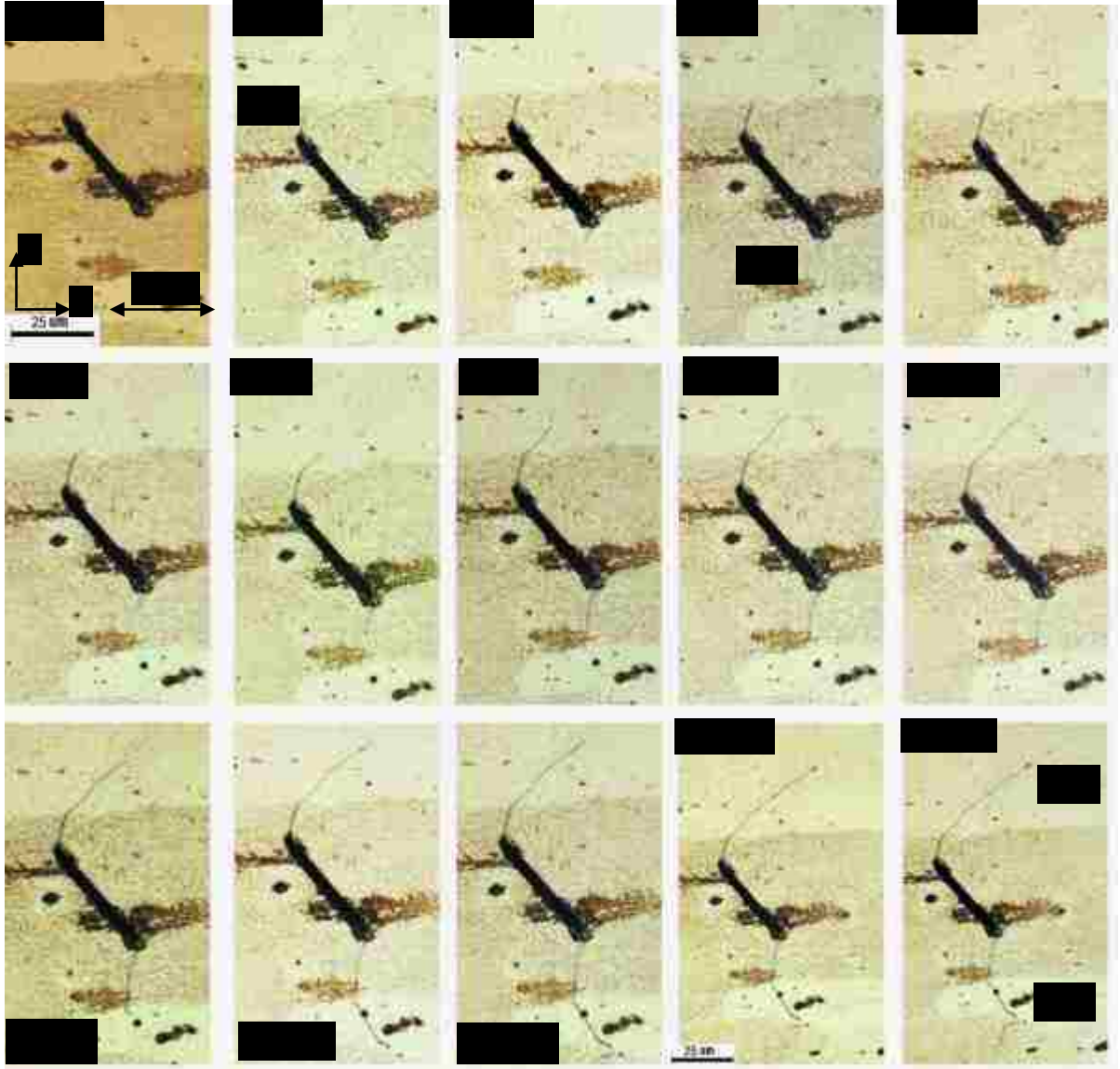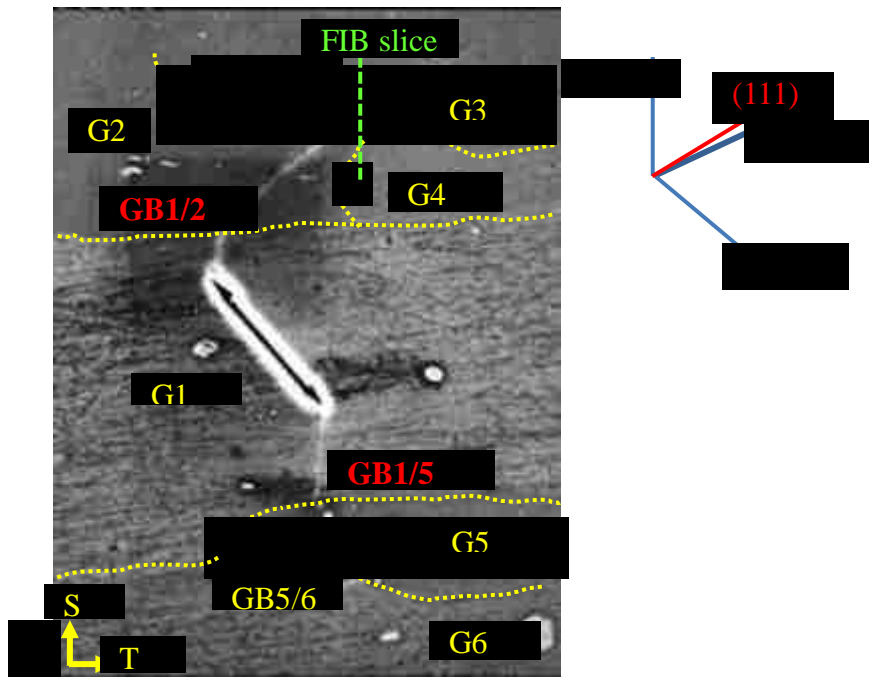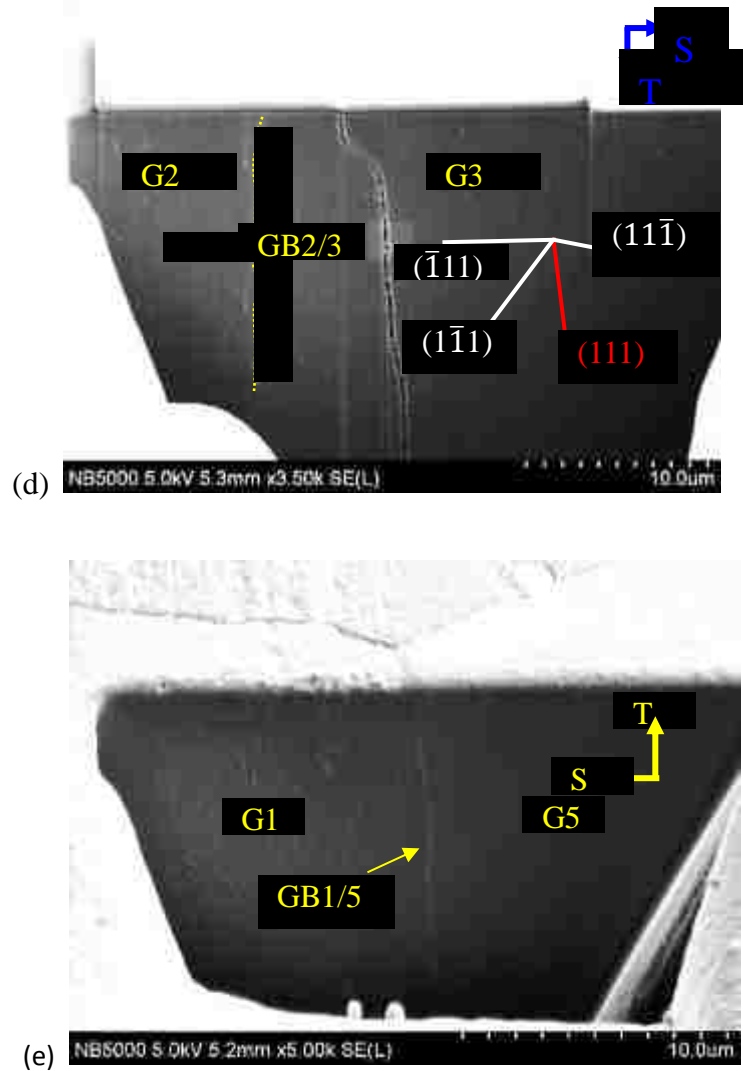
Figure 4.5 (a) Crack growth behavior of a short fatigue crack emanated from a pre-notch; (b) EBSD mapping presented in inverse pole figure mode with respect to L-direction; (c) SEM micrograph with GBs sketched out. As demonstrated on right are the traces of {111} planes in grain G3 on sample surface; (d) cross-section revealed by FIB milling along the dash line in (c). As superimposed drawing shows the traces of {111} planes in grain G3 on cross-section plane.
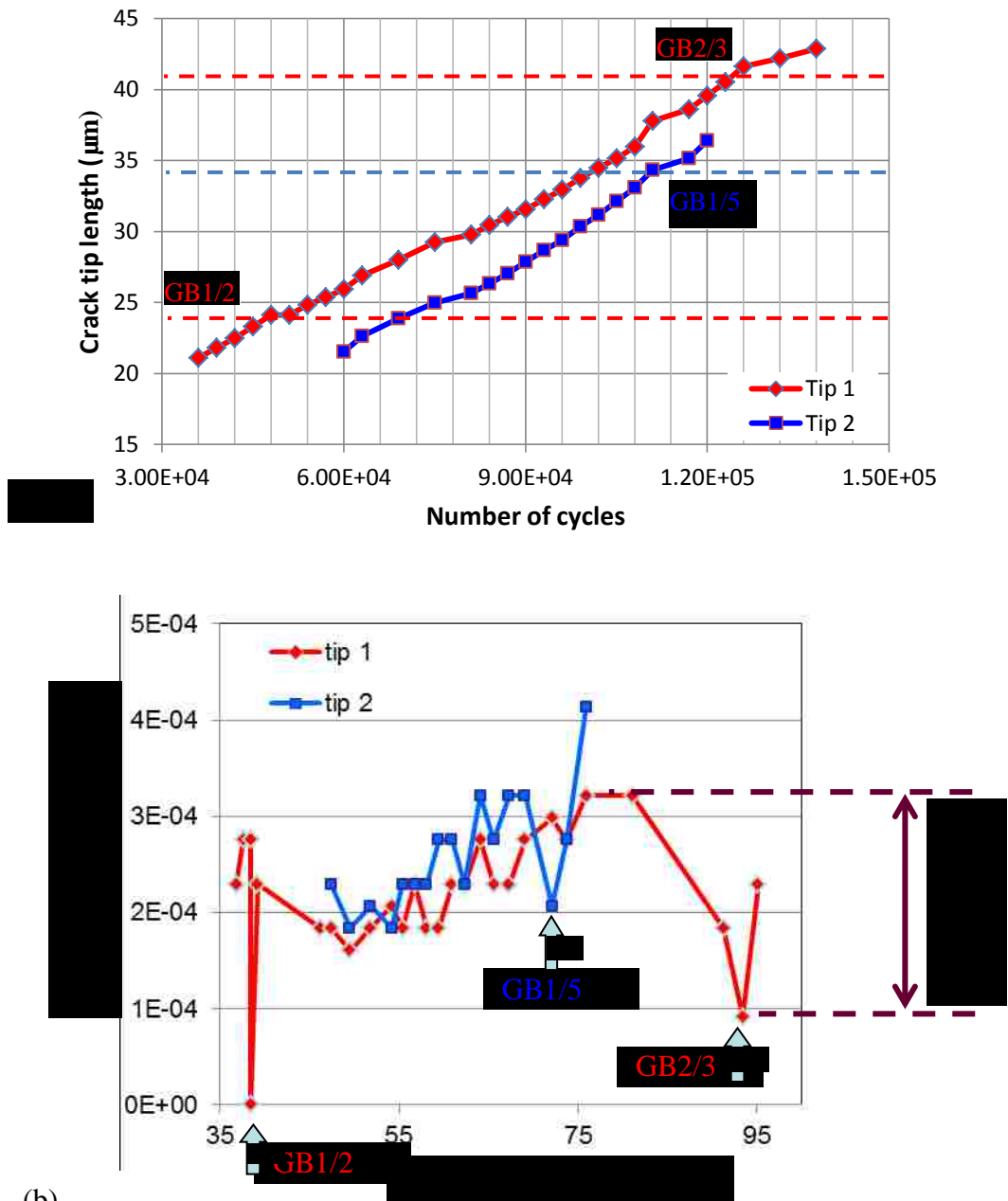
(b)

Figure 4.6 (a) Crack tip length vs. number of cycles; (b) growth rate vs. total crack length, which also shows the definition of Δ(da/dN) at GB2/3.

(b)
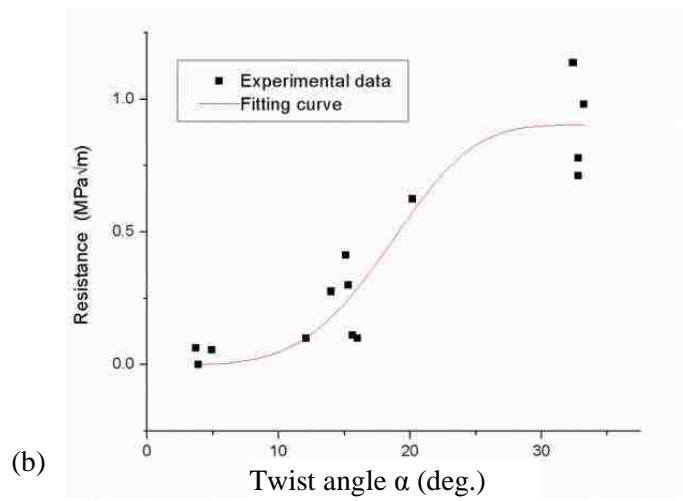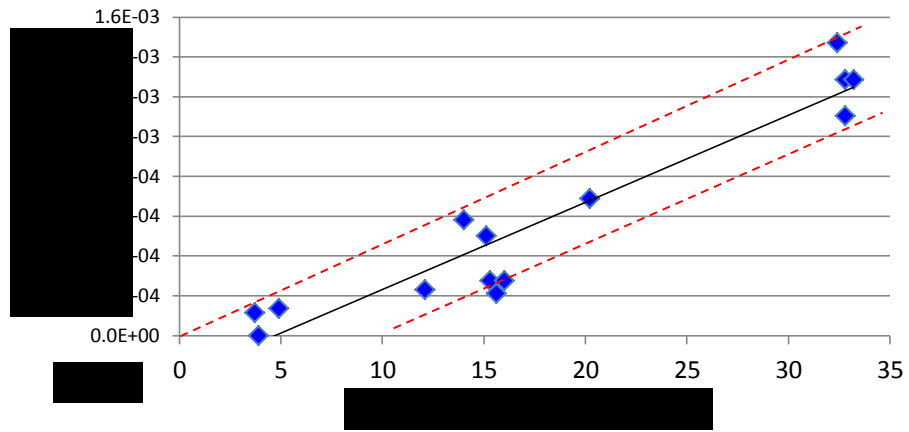
Figure 4.7 (a) Δ(da/dN) vs. α and (b) resistance of GB vs. α at 14 GBs.
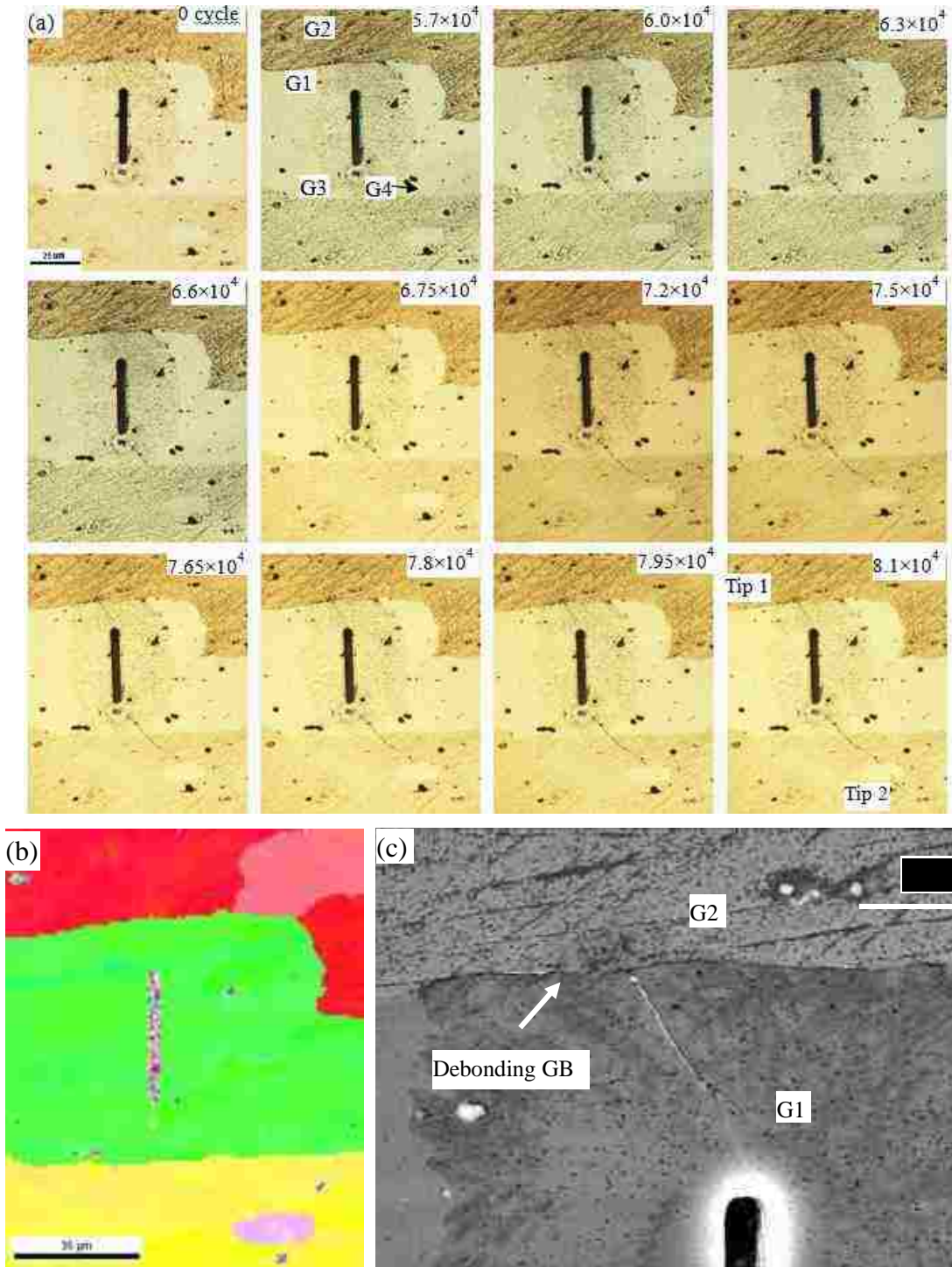
Figure 4.8 (a) Crack growth behavior of a short fatigue crack emanated from a pre-notch; (b) EBSD mapping presented in inverse pole figure mode with respect to L-direction; (c) SEM micrograph showing the crack being arrested at the GB.

Chapter 5 Modeling of Short Fatigue Crack Growth in 3-D in High-Strength Al Alloys

In the previous Chapters in this thesis, the behaviors of short fatigue crack growth through grain boundaries have been experimentally investigated. The results showed that: (i) GBs are the main barrier to the short crack growth; (ii) the twist angle (α) of crack plane deflection at the GB results in resistance to crack growth, thus controlling the crack path and influence crack growth rate; and (iii) GB-resistance increases with α, following a Weibull type function. All of these conclusions pave the way for developing a quantitative model to describe the short crack growth though grains in engineering alloys. In this chapter, a microstructurally-based numerical model was developed, in attempt to simulate the short crack growth through grains in 3-D.

5.1 Introduction

Grain boundaries are commonly considered to be one of the major barriers to short fatigue crack growth [62, 63, 65, 94] and account for the marked variation of the short fatigue crack growth rate measured in most engineering alloys [66-69]. Several analytical models have previously been developed in attempts to take into account the effects of local GBs/phase boundaries and crystallographic orientation on short fatigue crack growth behaviors. Hobson [163] accommodated the effect of GBs into two equations describing short crack growth via a statistical approach. However, his model only yields good agreement with experimental data within the first grain but fails beyond that [164]. Chan and Lankford [104] reconsidered the crack tip plastic strain range and modified the linear elastic fracture mechanics (LEFM) equation by introducing a crystallographic function $K(\Phi)$ with respect to resolved shear stress in cracked grain and its neighboring grain in front of the crack tip. Their model cannot satisfactorily explain the marked scattering often observed in the growth rates of short cracks. For example, it predicts little or no deceleration in growth rate when a crack is propagating through the boundary between two

similarly orientated grains. Based on the constraint on the crack tip plastic zone size [63], Navarro and De los Rios [117, 118, 122] incorporated the Sachs factor averaged over the grains along the crack front into their 2-D dislocation model which took into account the effect of slip band blocking by a GB in simulating short crack growth. Although it can predict the crack growth retardation at grain boundaries, this model cannot distinguish the difference in resistance between different types of GBs. Moreover, it is unable to explain crack branching at GBs and crack deflection observed inside grains rather than at a GB where the resistance to crack growth is expected to be the largest. These 2-D models could hardly deal with the 3-D effects of microstructures on short crack growth behaviors. With the aid of electron back scatter diffraction (EBSD), Zhai et al [95, 105, 174] studied the effect of crystallographic geometry of the GBs that interacted with short fatigue cracks in Al-Li and Al-Cu alloys in 3-D. A 3-D crystallographic model was subsequently proposed that the twist and tilt components (rather than misorientation) of the crack deflection at a GB were the key parameters controlling the growth behaviors of short cracks. It has also been supported by experimental observations of crack growth behaviors in Ni-based alloys [107, 113] and Ti-Al alloys [177], etc. This model is successful in qualitatively interpreting the 3-D behaviors of crack growth, such as crack deflection, branching, retardation and arrest at GBs, crack deflection inside grains and rugged crack profile in Al-Li alloys [143]. The model reveals that the resistance of individual GBs to short crack growth can be different, hence has to be taken into account in simulation of short crack growth satisfactorily.

In this work, based on the discovery that the resistance of a GB to short crack growth can be quantified as a Weibull-type function of the twist component of crack deflection at the GB, the growth behaviors of a short crack could then be simulated by taking into accounts both the resistance and driving force at each GB along the crack front. The effect of each GB that interacted with the crack could be incorporated in quantification of the crack growth.

5.2 A 3-D Model for Short Fatigue Crack

5.2.1 Resistance of GBs due to Crack Plane Twist

As discussed earlier, among all the microstructural factors such as α, β and Schmidt factor, α is the most dominant one that control the short crack growth [95, 105]. The experiments in Chapter 4 shows that the resistance due to α, $R_j(\alpha)$, is a Weibull-type function of α, as expressed by Equation 5.1.

$$R(\alpha) = R_f\{1 - \exp[-(\alpha/\alpha_0)^n]\} \tag{5.1}$$

Where R_f is the resistance (with the same unit as stress intensity K) when α is around the maximum possible value before another slip plane becomes available with a smaller twist angle. The possible maximum twist angle can be as large as up to 35.3 °(i.e., half the angle between two {111} planes). α_0 and n are scaling and shape factors, respectively. R_f, α_0 and n are material-dependent parameters that can be determined experimentally for a specific alloy by fitting the experimental crack growth rate curves. The trend of R vs. α is demonstrated in Figure 5.1.

The resistance of a GB could also be contributed by its neighboring GBs, as these GBs could interact with each other when a short crack propagates through these GBs simultaneously. So, the total resistance, $R_{eff,i}$, at GB$_i$ is the summation of the contributions from all its neighboring GBs, as shown by Equation 5.2.

$$R_{eff,i} = \sum_j^M P_{ij} \cdot R_j(\alpha) \tag{5.2}$$

Where $R_j(\alpha)$ represents the resistance merely from GB$_j$ and is a function of α at GB$_j$ and P_{ij} is an interaction factor describing the percentage of the resistance at GB$_j$ is contributed to the resistance at GB$_i$. P_{ij} is a function of the geometry of the crack front and the distance between GB$_i$ and GB$_j$. M is the total number of GBs interacting with the crack. In this work, P_{ij} is assumed to be a simple Gaussian function, as schematically demonstrated in Figure 5.1(b).

$$P_{ij} = aexp(-(x_{ij} / D)^2) \tag{5.3}$$

Where x_{ij} is the distance between GB$_i$ and GB$_j$ on the crack front, D is the coefficient which adjusts the bell shape described by the function, and a is a constant. D determines the effective zone size and intensity of the resistance around GB$_i$. The larger the D is, the larger the zone affected by GB$_i$ is. Since the maximum value of P_{ij} is 1, $a = 1$. The assumption in Equation 5.2 is made, based on the fact that the crack front around a GB of high resistance is often dragged by the GB [174].

5.2.2 Driving Force for Crack Growth along the Crack Front

In this work, as an attempt to quantify the short crack growth behavior along the crack front, mode I loading is considered in calculating the driving force and resistance at each GB along the crack front. The torturous crack front due to crack plane deflection at GBs will be projected on the plane normal to load axis. The effective driving force for the crack growth at GB$_i$ is given by

$$\Delta K_{eff,i} = \bar{K} - R_{eff,i} \tag{5.4}$$

Where $\bar{K}$ is the crack growth driving force, expressed by Equation 5.5 [18, 20].

$$\bar{K} = (K_{max}\Delta K^+)^{0.5} \tag{5.5}$$

In Equation 5.5, K_{max} is the corresponding maximum value of the applied stress intensity factor, and ΔK^+ is the positive part of the range of the applied stress intensity factor [20-23]. This correlates the R-ration effects for Al alloys. The applied stress intensity factor of the imaginary semi-circular crack whose radius (a_{max}, (Figure 5.2)), is defined by the maximum distance from center of the crack to the crack front, as calculated by $\Delta K = 2\Delta\sigma\sqrt{a_{max}/\pi}$. Therefore, the effective driving force at an arbitrary point along the crack front is given by

$$\Delta K_{eff,i} = (K_{max}\Delta K^+)^{0.5} - \sum_j^M P_{ij} \cdot R_j(\alpha) \tag{5.6}$$

When $\Delta K_{eff,i} \leq 0$, the crack is non-propagating at GB$_i$, while it is propagating when $\Delta K_{eff,i} > 0$. The larger the term $\sum_j^M P_{ij} \cdot R_j(\alpha)$ is, the smaller the effective driving force for crack growth at GB$_i$.

5.2.3 Crack Front Growth in 3-D

In this work, a simple layered grain structure is used for simulating short crack growth in an alloy, like the case of some high strength Al-Cu and Al-Li alloys where grains have a disk-like shape. As shown in Figure 5.2(a), the grains have large dimensions in L (rolling) and T (transverse) directions but small in the S (short transverse) direction. Assuming the alloy in Figure 5.2(a) has a matrix which is a continuum homogeneous linear elastic solid which contains 5 GBs, and a crack propagates only along one slip plane in each grain. The shape of a surface crack is semi-circular or semi-elliptical in a continuum homogeneous isotropic linear elastic solid, since the applied driving force (i.e., the stress intensity factor K) is constant along the crack front, as shown by the dot-dash line in Figure 5.2(a). However, the shape of a real short fatigue crack (<0.5 mm) in an engineering alloy can be significantly irregular, as illustrated by the solid line in Figure 5.2(a), because the resistance varies markedly at different GBs along the crack front. At those GBs that have larger α, for example, GB2 and GB4, the crack front falls behind the semi-circular or elliptical line, while the crack front around those GBs that have smaller α, can move faster than that at the GBS with larger α. The relationship among the nominal driving force, effective resistance and effective driving force at an arbitrary i on the crack front along the crack front can be expressed by Equation 5.6 and schematically demonstrated in Figure 5.2(b).

To simulate the growth of the crack front, first, it is assumed that the size of the plastic zone at the crack tip is small, relative to the crack size in high strength Al alloys. This assumption is supported by the experimental observations that there are hardly any slip lines other than the one along the crack ahead of the crack tip. Figure 5.3(a), for example, shows the tip of a 110 μm long short fatigue crack occurred in an AA2524 Al-Cu alloy after four point bend fatigue at 8.74×10^5 cycles under constant maximum stress of 80% yield strength at R=0.1. There is no multiple slip taking place in the vicinity of the crack tip. EBSD measurement on the crack reveals almost no crystallographic misorientation around

the crack tip (Figure 5.3(b)). The misorientation and misorientation gradient along the dot line from point *a* to the crack tip reveal that there is an increase in misorientation from 1° to 3.75° in the position about 2 μm away from the crack tip (Figure 5.3(c)). Similarly, the misorientation gradient remains very low (much lower than 1°), but only increases at 2 μm away from the rack tip (Figure 5.3(d)). This indicates that the plastic zone size in the vicinity of the crack tip is about 2 μm about the crack tip. Such a plastic zone size is very small, in comparison to the crack length, so the linear elastic fracture mechanics (LEFM) can be applied to quantification of the crack growth in the high strength Al alloy. In other words, the Paris law can be used to quantify the growth rate along the short crack front in the alloy.

Since the effective driving force at each point along the crack front can be characterized by Equation 5.6, the crack contour can be discretized by the small segments ended at each two adjacent points. Thus, the advance of crack front line can be equally represented by the progress of the segments, as demonstrated in Figure 5.4. S_1 (ending at P_1 and P_2) and S_2 (ending at P_2 and P_3), are two neighboring segments of crack front at the nth cycle. Under the driving force $\Delta K_{eff,P1}$, $\Delta K_{eff,P2}$ and $\Delta K_{eff,P3}$, P_1, P_2 and P_3 advance for $\Delta a_1, \Delta a_2$ and Δa_3 (Equation 5.7) in the next cycle to P_1', P_2' and P_3', respectively. The direction of Δa_i is normal to line $P_{i-1}P_{i+1}$. Therefore, the new crack front line in at the n+1th cycle will be represented by the points P_i' linked by segments S_i'. At the convex parts of the crack front, a new segment at the n+1th cycle will be longer than that at the nth cycle. If its length exceeds the up-limit of mesh size, then a new point will be inserted in the segment to divide it into two segments to keep the fine mesh. This calling for further mesh is conducted if needed at each cycle to keep the same level of sensitivity of the crack front to the GB resistance.

$$\Delta a_i = \int C\left(\Delta K_{eff,Pi}\right)^m dN \tag{5.7}$$

5.2.4 Framework of the Model

Since the resistance along the crack front is mainly controlled by the resistance of the GBs that interact with the crack front, the factors, such as grain and GB orientations, and grain size ahead of the crack front, would affect the 3-D crack path and growth rate, as illustrated in Figure 5.5. Once the orientations of the initial micro-crack plane and the neighboring grain of the crack are known, the possible α at the GB can be calculated. Subsequently, the crack path could then be predicted, according to the minimum α principle for short crack growth across the GB. Knowing the grain orientation and size, the nominal driving force, and effective resistance, the effective driving force at each point along the crack front can be computed. A modified Paris law, given in Equation 5.7, is employed to calculate the position of each point along the crack front at each loading cycle. Since the new crack front will change the value of the interaction factor P_{ij} in Equation 5.3, $R_{eff,i}$ and ΔK_{eff} need to be recalculated for the next loading cycle. The computation continues until the crack becomes a long crack, namely, it covers a sufficiently large number of grains, so that the resistance at each GB can be regarded as a constant (i.e., the average value). Subsequently, quantification of further crack growth can be made using the classic Paris law but with a constant resistance term (R) in ΔK_{eff}. In other words, $\Delta K_{eff} = \bar{K} - R$, where $\bar{K}$ is the applied nominal driving force. R is alloy dependent and responsible for the higher resistance found in the alloys where fracture surface is torturous.

5.3 Simulation of Short Fatigue Crack Growth

5.3.1 Baseline Setup of Simulation

As an attempt to demonstrate how the resistance of GBs affect short crack growth in 3-D, an alloy with simple layered grains is used in this work. As shown in Figure 5.6(a), the planes of the main GBs (marked as dash lines in Figure 5.6(a)) in the alloy are parallel to the L-T plane and perpendicular to the free surface. As mentioned earlier in the paper, such

a grain structure resembles the grain structure typically found in some high strength Al alloys [16]. It is assumed that the initial crack is 6 μm long with a semi-circular shape centered in grain 1. The grain structure is symmetrical with respect to $x=0$ in order to save the computation time as the growth behaviors of both the crack tips are identical on the surface. The resistance assigned to the GBs in the alloy is increased gradually from the boundary between grains 1 and 2 (GB1/2) to GB4/5. The twist angles of 6°, 8°, 10°, and 13° are assigned to GBs 1/2, 2/3, 3/4 and 4/5, respectively, i.e., the resistance at these GBs is from 0.1 to 0.5 MPa√m, respectively, labeled in Figure 5.6(a). With such a grain structure, the applied maximum cyclic stress of 150 MPa and stress ration $R=0$ are used in the model in order to simulate the growth of a propagating short crack in the alloy. In other words, the crack simulated could propagate through each of the GBs in the grain structure. In $\Delta a_i = \int C\left(\Delta K_{eff,Pi}\right)^m dN$, the exponent $m = 2.73$ and $C=1.89 \times 10^{-10}$ m/cycle which is approximately 2 orders of magnitude larger than that for long cracks because short-fatigue cracks sometimes grow faster than the long cracks by 1 to 2 orders of magnitude [1]. The values of the parameters used in the simulation are listed in Table 5.1.

5.3.2 Results and Discussion

5.3.2.1 Crack Front Evolution in 3-D

Figure 5.6(a) shows the simulated growth of the crack front in 3-D for 9×10^3 cycles in a simplified digital grain structure using the model described above in this paper. The solid lines in Figure 5.6(a) represent the crack fronts at different numbers of cycles with an interval of 500 cycles, respectively. The final crack is 50 μm long on the surface and 43 μm in depth. The average growth rate of each crack tip is about 2.4 nm/cycle, which is reasonably consistent with the typical growth rate (0-8 nm/cycle) of a short fatigue crack measured in high strength Al alloys [17] AA8090 Al-Li alloy [143, 167]. It can be seen in Figure 5.6(a) that the crack front is evolved from the initial semi-circular shape to a bell shape with the bell axis being parallel to the GBs. This is understandable since a short crack normally grows faster in the direction parallel to the main GBs than in the direction

perpendicular to the GBs in such a grain structure. The crack front is dragged behind by those GBs that have relatively large resistance, such as GBs 4/5, 3/4 and 2/3, etc. The higher the α at a GB is, the farther the crack front near that GB lagged behind. It is evident in Figure 5.6(a) that each GB still has an effect on the crack growth after the crack propagates through the GB on the surface. However, such an effect is weakened with the increase in crack length, since the applied driving force increases with the crack growth and the GB resistance remains constant. As a result, the effective driving force is increased as the crack grows, leading to a steady increase in crack growth rate along the same GB below the surface. Take the GB2/3 as an example, the curvature of the crack front is initially outward due to higher resistance by the GB, but becomes inward around the GB as the crack grows deeper below the surface, indicating the reducing effect of the GB resistance. This effect could be responsible for the crack front being in a bell shape in such a grain structure.

The result shown in Figure 5.6(a) demonstrates that the crystallographic model for short crack growth is able to simulate crack growth in 3-D, unlike the previously developed models which are all 2-D and typically predict that the crack growth rate regains its original value immediately after the crack tip passes a GB on sample surface [117, 122]. In the model developed in this work, the growth of the crack tip is still affected by the GB that it just passes because first crack tip is still dragged by the same GB below the surface until the crack tip advances beyond the effective zone of the GB. For example at GB1/2, the crack profiles on the sample surface experience shorter spacing just after the crack tip passes the GB on the surface, indicating higher resistance from the GB under the surface. Subsequently, these profiles show increasingly larger spacing as crack tip grows further away from the GB. This effect will be discussed in more details in the next session.

5.3.2.2 Growth Rate Curve

The growth rate of each crack tip on the surface is plotted against ΔK in Figure 5.6(b). It is evident in Figure 5.6(b) that the growth rate shows a dip in the plot at each GB that the crack interacts with, and that it generally increases with crack length, though the resistance also increases at GBs in the sequence of interaction with the crack. However, the amount of the dip in the growth rate curve at a GB appears increase with the resistance of the GB. For example, at GB1/2 which has a resistance of 0.1 MPa√m, the growth rate dip is 6.0 nm/cycle, as compared to 118.6 nm/cycle at GB4/5 where the resistance is 0.5 MPa√m.

As discussed earlier in the chapter, the growth of the short crack front is affected by all the GBs that interact with the crack. The growth rate of the crack tip on the surface does not pick up its original speed immediately after passing a GB, since the GB still drag the crack beneath the surface. As a result, it gradually increases as the crack tip advances further away from the GB on the surface. This is because the resistance from the GB decreases with the distance from the GB. Such a 3-D effect of the GB explains why the experimentally measured growth rates of short cracks are so scattering. In measurements, it is difficult or even impossible to monitor the crack growth at each cycle. Instead, the growth rates are usually taken by measuring the growth length on the surface for a period of several thousand cycles. Therefore, details of the crack growth behaviors could be missed, leading to rather scattered growth rate data. With the model developed in this work, these growth behaviors can be investigated in details, especially around the GBs the crack propagates through, as shown in Figure 5.6(b).

To illustrate the effect of crack length on the growth rate of a short crack, the growth rate of the crack tip on the surface is quantified against the crack half-length in a grain structure consisting of layered grains of 10 μm thick, as shown in Figure 5.7. Each GB in the grain structure has a constant twist angle of 7.25˚, which is equivalent to a resistance of 0.15 MPa√m. It can be seen in Figure 5.7 that the growth rate drops at each GB, but

the amount of the decrease in growth rate is progressively reduced at the GBs as the crack propagates. The variation of the growth rate can be enveloped by two asymptotes that approach to each other as crack size increases. The result shown in Figure 5.7 demonstrates that the resistance from each individual GB to crack growth becomes less significant as the crack grows longer. This is because GBs could interact with each other and the resistance from each individual GB to crack growth is contributed to by all the GBs along the crack front. When the crack becomes a long crack, more GBs interact with the crack front. The resistance from each GB approaches to an average value. As the crack grows longer under a constant cyclic stress amplitude, the driving force is increased since the crack length increases. As the average resistant from each GB is almost a constant, the relative influence of each GB on crack growth should be weakened, as compared with increasingly large nominal driving force, thereby the dips in the growth rate curve at GBs become relatively smaller as the crack becomes longer, as shown in Figure 5.7. This average resistance may be regarded as a materials property describing difficulty of long fatigue crack growth.

The result in Figure 5.7 is consistent with that predicted by Navarro's 2-D model which takes an average value for the crystallographic effects of the grains covered the crack front on short crack growth on the surface [13,14]. However, Figure 5.7 is obtained using the 3-D model developed in this work, demonstrating that this 3-D model is able to simulate the growth behaviors of both short and long cracks.

5.4 Experimental Verification

5.4.1 Experiment

As an attempt to validate the proposed model, it was used to simulate the growth behavior of short fatigue cracks in the Al-Li alloy 8090 in Chapter 3. The details regarding material and experimental procedures were introduced in Chapter 3. This section, serving as an example, demonstrates the capability of the model in simulating the growth of the crack in

Figure 3.2. This crack was found on the sample surface at 7×10^5 cycles when it was about 30 μm long, and subsequently its growth was monitored by interrupting the fatigue test periodically until 9.15×10^5 cycles. Figure 3.2 shows its morphology before and after etching at 9.15×10^5 cycles. After the measurement of crack growth rate, the sample was etched with Keller's etchant to reveal the grain structure. Also, the crystallographic orientation of each grain that interacted with the crack was determined using EBSD. More details regarding the crack growth vs. GBs has been discussed in Chapter 3.

In the simulation, the digital grain structure was constructed based on the experimentally observation. For simplicity, the digital grains were layered with major GBs bring perpendicular to S direction, because the grains in the alloy possessed pancake shape due to hot cross-rolling. The width of each grain was assigned to be the crack path length (projected to S direction) within each grain, i.e. distance (as projected to S direction) between two intersection points of GBs with the crack path. The crystallographic orientation of each grain that interacted with the crack was assigned with the experimentally measured value. A secondary GB parallel to surface, lying about 15 μm beneath grain 1 as shown in fractography Figure 3.3, was added in the digital microstructure. Since it is very difficult, even impossible, to precisely measure the lifetime at the crack initiation and initial size of the crack, a 10 μm long semi-circle micro-crack in the surface was assumed to be initiated in the center of grain 3 at 6.5×10^5 cycles. This assumption is within the average range of lifetime for crack initiator (6×10^5-10×10^5 cycles) in Al-Li alloys [166]. The parameters used in the simulation were obtained from either literatures or experiments, as listed in Table 5.2. The coefficients C and m were assigned to be 1.43×10^{-10} m/cycle and 2.09, respectively, which are the averaged values obtained by fatigue experiments of the Al-Li alloy AA8090 [103, 178]. The twist angle and corresponding resistance at each GB were provided in Table 5.3 Since it was unable to measure the crystal orientation of grain 1' which was underneath grain 1, α along GB1/1' was estimated to be 10° for an approximate, based on that GB1/1' had a significant resistance against crack tip growth

on surface (Chapter 3). With such a grain structure, the same loading condition as those used in the fatigue test (applied maximum cyclic stress of 246 MPa and stress ration R=0.1) was used in the calculation.

5.4.2 Simulation Results and Discussion

5.4.2.1 Crack Front Evolution

Figure 5.9 shows the simulated evolution of the crack front progress in 3-D during fatigue, starting from the initial crack to 8.6×10^5 cycles in the reconstructed digital grain structure. The solid blue lines in the figure represent the crack fronts at different numbers of cycles. Because the crack growth rate at the beginning is very small, so the interval of crack front contours is selected to be 5000 cycles before crack tip 2 reaches GB7/8, to avoid the over-dense plotting in the graph. After tip 2 passing GB7/8, the interval is set to be 1000 cycles in order to show the details of the crack front advancement. The final crack is 117.4 μm long along S direction on the surface and 93.8 μm deep along T direction. This is understandable since a short crack normally grows faster in the direction parallel to the main GBs than in the direction perpendicular to the GBs in such a grain structure.   It can be seen in Figure 5.9 that the crack front, starting from the initial semi-circular shape, is evolved asymmetrically to an irregular shape, with crack tip 2 being much longer (~82.1 μm) than tip 1 (~35.3 μm), which is consistent with experimental observation on sample surface. As shown by crack profiles, the local crack front is dragged behind by those GBs that have relatively large resistance, such as GBs 1/2, 1/1', 13/15, 11/13 and 8/10. The higher the α at a GB, the farther the crack front near that GB lagged behind, leaving denser crack contour lines. Seeing from the density of the contour lines, it shows two major retardations on crack tip 1 at GB2/1 and GB1/1', and one major retardation on tip 2 at GB13/15, which is mainly responsible the asymmetric shape of the final crack contour and will be discussed later. Unlike the previously developed models which are all 2-D and typically predict that the crack growth rate

regains its original value immediately after the crack tip passes a GB on sample surface [117, 122]. In this simulation, the growth of the crack tip is still affected by the GB that it just passes because surface crack tip is still dragged by the same GB below the surface until the crack tip advances beyond the effective zone of the GB. For example, each time when the crack tip on the surface passes a high-resistance GB, the crack contour line still keep narrowly spaced until these profiles subsequently show increasingly larger spacing as crack tip grows further away from the GB. Such an effect is weakened with the increase in crack length, since the applied driving force increases with the crack growth and the GB resistance remains constant. As a result, the effective driving force is increased as the crack grows, leading to a steady increase in crack growth rate along the same GB below the surface.

5.4.2.2 Crack Growth Rate Curve

In order to compare the simulated crack growth rate with the experiment observation, the crack growth rate curve was extracted from the simulation results and plotted. For example, as shown in Figure 5.9, the growth rate of crack tip 2 is plotted against nominal driving force, ΔK. It is evident in the figure that the crack growth rate generally increases with increment in crack length and scattering as crack grows. The growth rate curve shows dips at high-resistance GBs, such as GB8/10 and GB13/15. The amount of the dip in the growth rate curve at these GBs appears to be increased with a rise in the resistance of the GB. For example, at GB 8/10, which has a resistance of 0.37 MPa√m, the growth rate dip is 0.34 nm/cycle, compared with 3.38 nm/cycle at GB11/13 where the resistance is 1.49 MPa√m. As discussed previously, the growth rate of the crack tip on the surface does not pick up its original speed immediately after passing a GB, because the GB still drags the crack beneath the surface. As a result, it increases gradually as the crack tip advances further away from the GB on the surface. At those GBs that have low resistance, such as GB7/8 and GB 10/11 whose resistance values are so low that can be ignored

(resistance≈0), the crack growth rate does not show any decrease. It is noteworthy that the growth rate curve drops at $\Delta K = \sim 1.79$ MPa√m although it is not obviously associated with any GB passed by crack tip 2. However, if tracing the crack profile to crack tip 1, it can be found that tip 1 is just beginning to interact with two high-resistance GBs simultaneously (GB1/2 and GB1/1', i.e. the GB triple junction of grain 2, 1 and 1'). As discussed previously, the growth of the short crack front is affected by all the GBs that interact with the crack, i.e. the total resistance at GB, $R_{eff,i}$, is contributed by all GBs interacting with the crack front contributed the resistance. The total resistance of these two GBs is 2.44 MPa√m, which not only dramatically slows down tip 1 but also projects 0.42 MPa√m over to tip 2, causing a dip (0.32 nm/cycle) in growth rate of tip 2. Since the majority of the crack front (tip 2 and the crack front deep beneath the surface) keeps advancing, so the effective driving force continues to rise, resulting in the tip 2 speeds up gradually. When the most part along the crack front propagates away from the effective zone dominated by the GB triple junction, the increment in the effective driving force enables tip1 to regain its original growth rate, which led to the acceleration along the whole crack front. Such acceleration continues until crack tip 2 impinges GB11/13 whose resistance equals to 0.23 MPa√m. Although the crack growth rate dip by GB11/13 (theoretically only 0.15 nm/cycle) is not apparent in the plot, due to the growth rate dip being too small to show clearly on the plot, it is still explicit that the slop of grow rate after GB11/13 is decreased significantly, which means that the GB still drags the growth of crack tip 2 on sample surface.

As shown in Figure 5.10, the experimentally measured and simulated crack growth rates of tip 2 are plotted against the number of loading cycles, respectively, with arrows indicating the location of GBs that were passed by tip 2. The simulated result has a good agreement with the experimental one in terms of the location of major peaks and valleys along the growth rate curve, although the scale and exact shape of the curves do not match those in the measured curve perfectly. The consistency of simulation and

experiment suggests that this microstructurally-based model is of capability in quantifying the growth behavior of the short fatigue crack in high strength Al alloys.

5.5 Conclusions

- A three dimensional microstructurally-based quantitative model was developed to simulate/predict the behavior of short fatigue propagation through GBs, based on the discovery that the resistance of a GB against the short fatigue crack growth increases with the twist angle of the crack plane deflection at the GB, following a two-parameter Weibull function.

- The total resistance at each GB along the crack front can subsequently be known, which allows calculation of the effective driving force at the GB.

- The growth of the entire crack front can be simulated beneath the free surface using a modified Paris Law.

- The model is able to demonstrate short crack growth behaviors commonly observed in alloys, such as crack retardation at GBs, and scattered growth rates, etc. The higher the resistance at a GB, the more significant the crack is retarded at the GB. The model also demonstrates that the relative effect of GBs on crack growth is reduced as the crack becomes a long crack.

- The model was used to simulate the growth behavior of a real short fatigue crack monitored in the fatigue test of a high strength Al alloy. The simulation results showed good agreements with the experimental observations, validating the capability of the model in quantifying short fatigue crack growth in planar slip alloys.
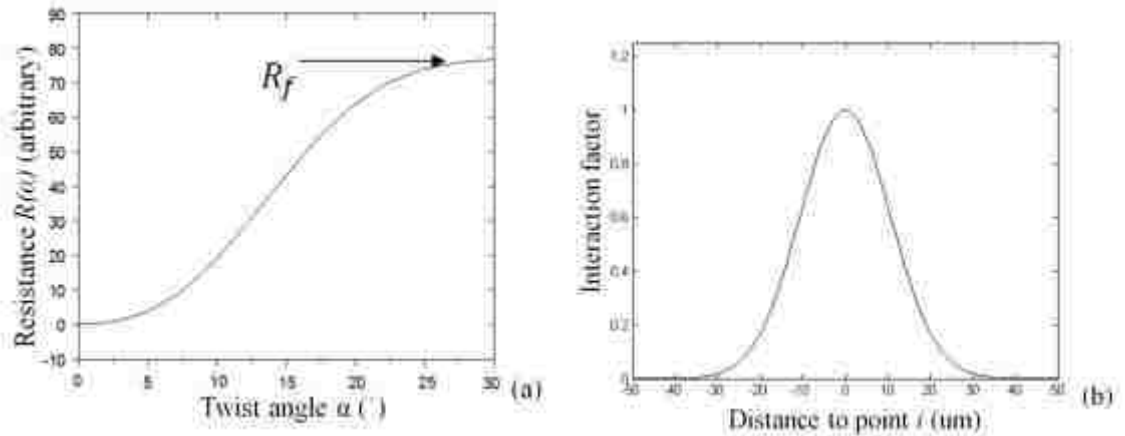
Figure 5.1 Schematic plot of (a) GB-resistance as a Weibull type function of α, (b) interaction factor P_{ij} as a Gaussian type function of distance.
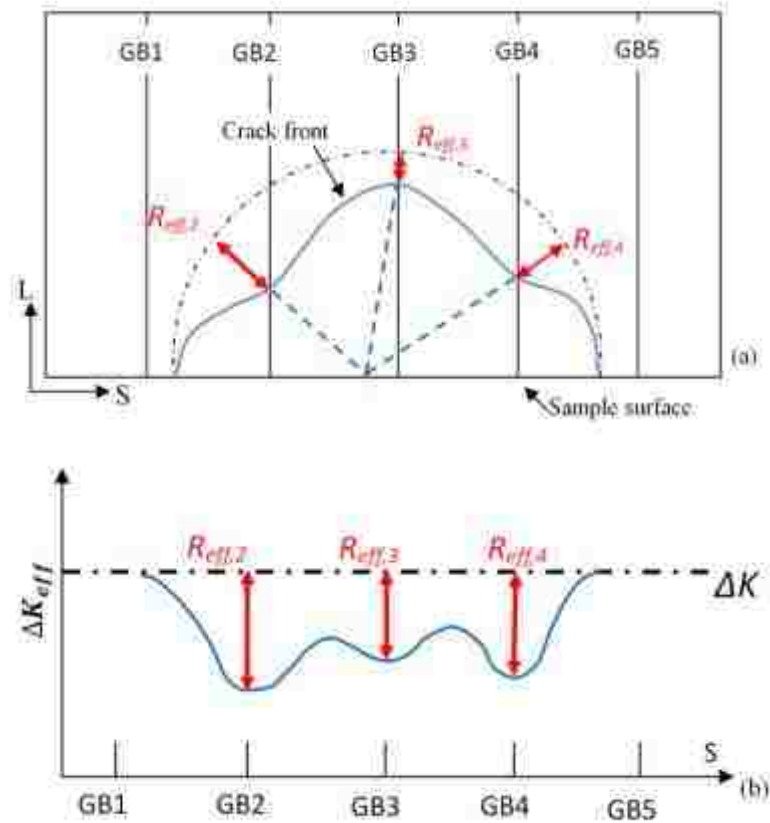
Figure 5.2 Schematic diagram demonstrating the relationship among nominal driving force ΔK, effective resistance $R_{eff,i}$ and effective driving force $\Delta K_{eff,i}$, respectively (a) the crack front projected on the plane normal to the load axis in an alloy with a layered grain structure, and (b) plot $\Delta K_{eff,i}$ along the crack front.
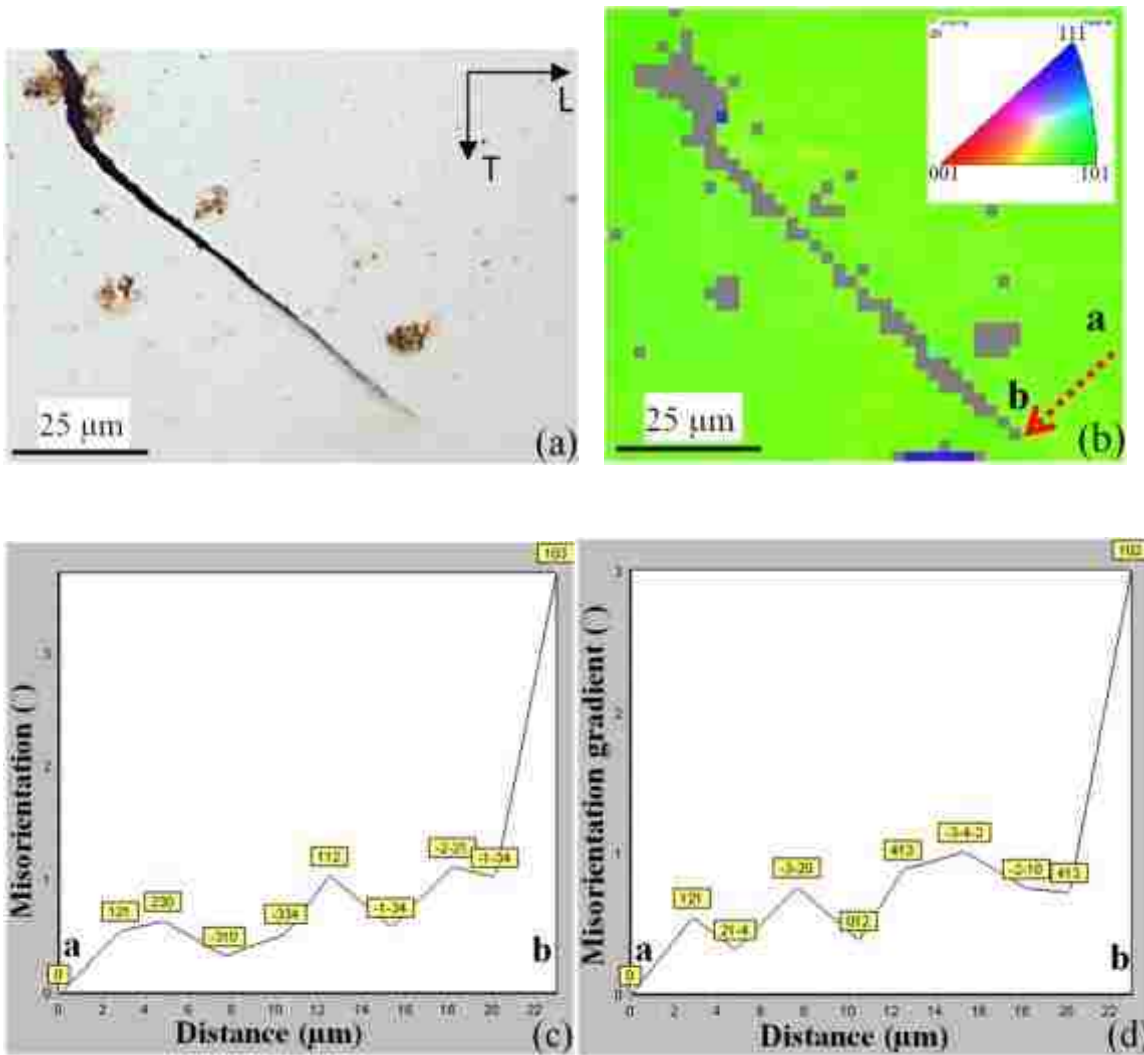
Figure 5.3 (a) one tip of a110um long crack in Al-Cu alloy AA2524 after 8.74×10^5 cycles, showing no multi slip around the crack tip, (b) EBSD measurement (shown in inverse pole figure mode) over the area shown in (a), (c) and (d) the misorientation gradient and misorientatoin from point A to point B in (b), respectively, indicating very small possible plastic zone at the tip.
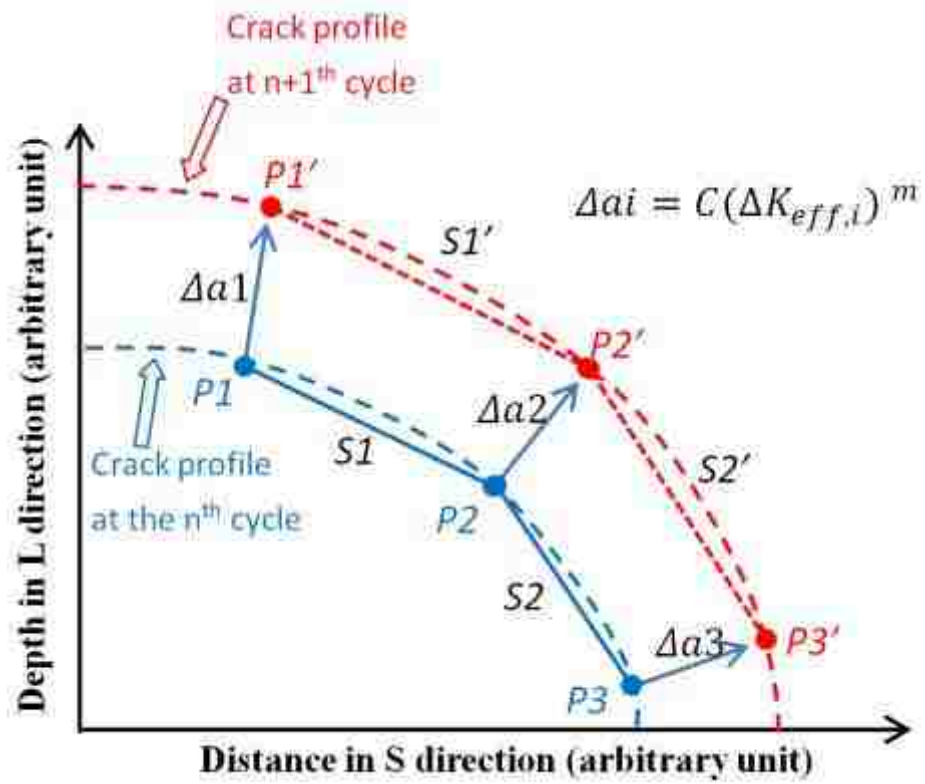
Figure 5.4 Schematic drawing the discretization of a small part of crack front and its growth in a loading cycle.
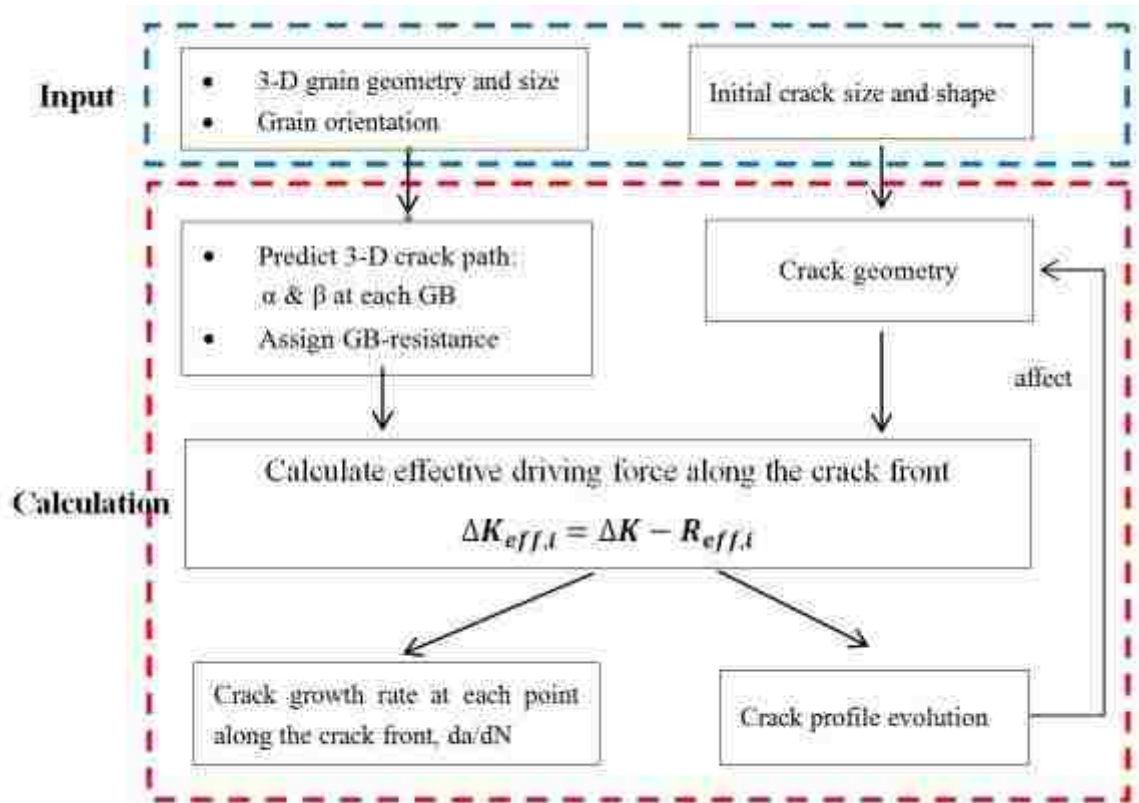
Figure 5.5 Flow chart of the procedure for calculation of short crack growth in 3-D.
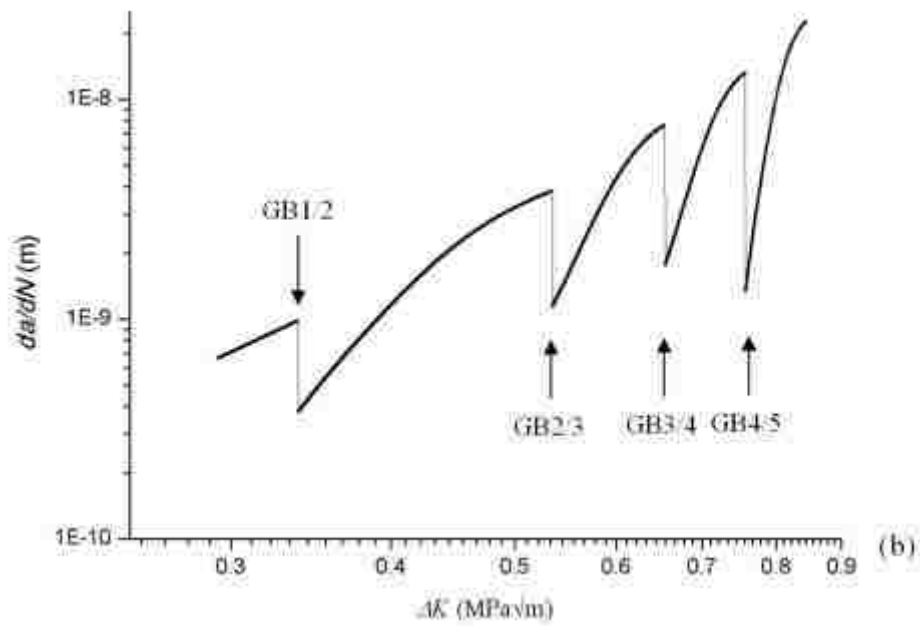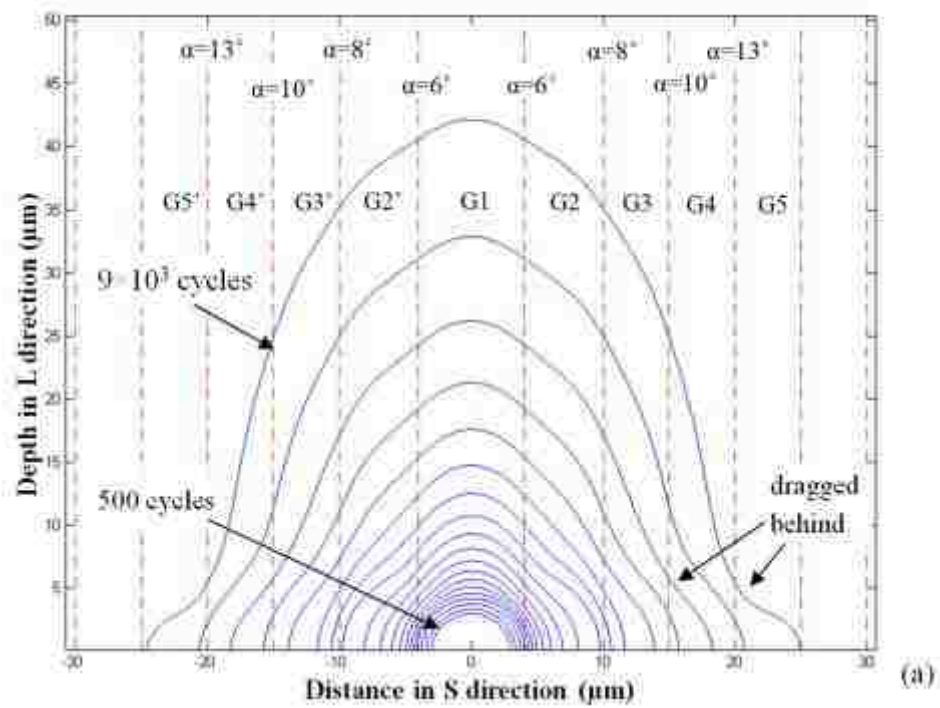
Figure 5.6 Simulation of short crack growth in a digital grain structure (a) growth of the crack front with cyclic number; (b) growth rate variation of either of crack tips (crack is symmetric with respect to *x*=0).
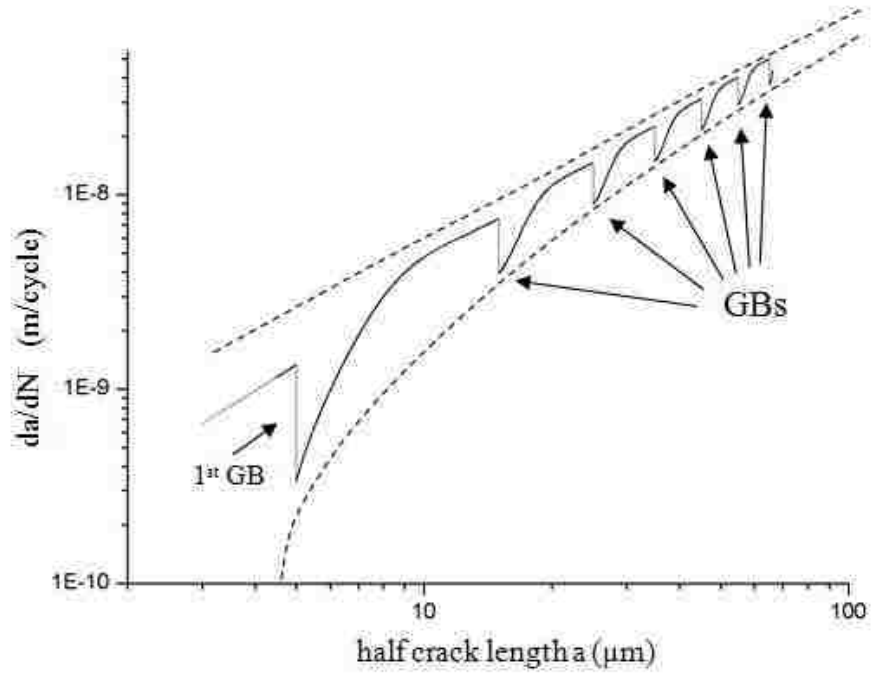
Figure 5.7 Demonstration of the effect of GB resistance as crack grows. Data of da/dN is from either of crack tips (crack is symmetric with respect to x=0).
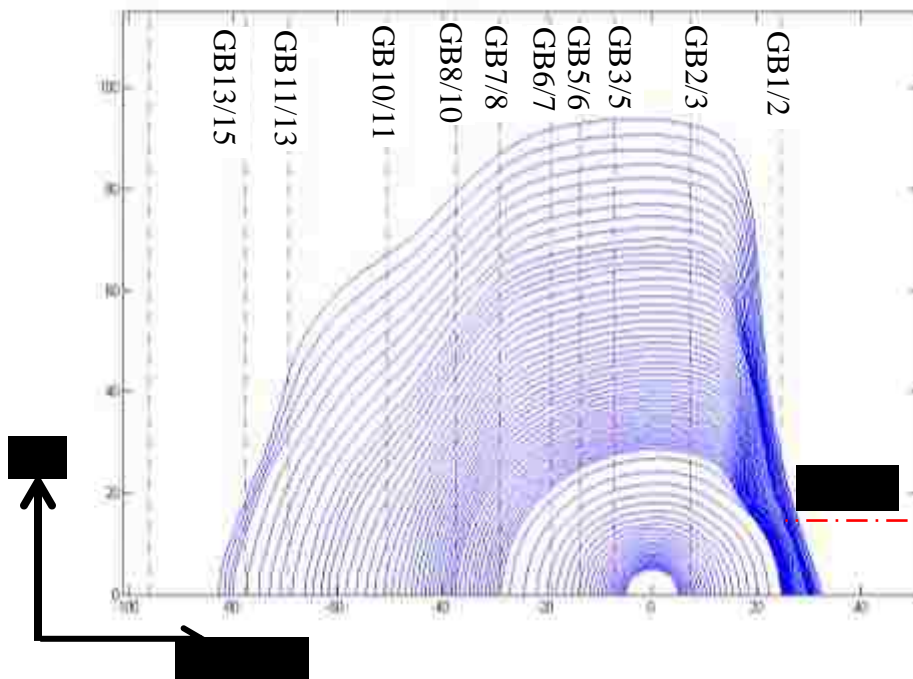
Figure 5.8 Simulated evolution of crack front progress during fatigue.
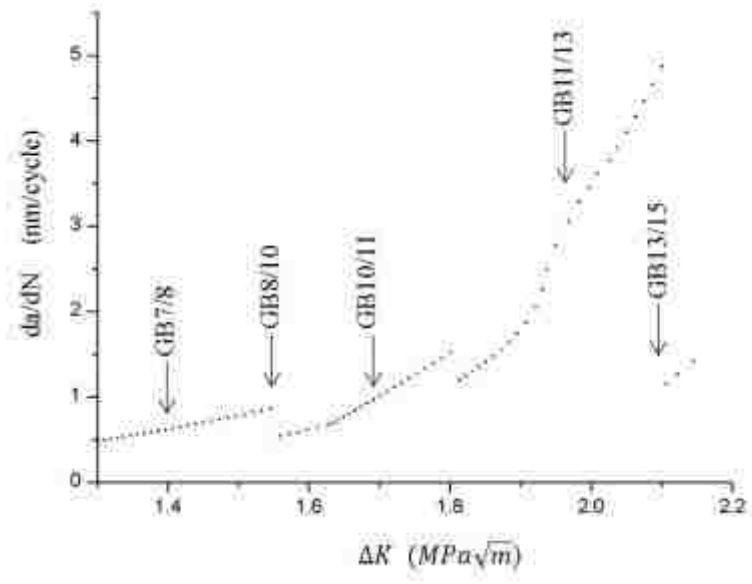
Figure 5.9 Crack growth rate curve of crack tip 2
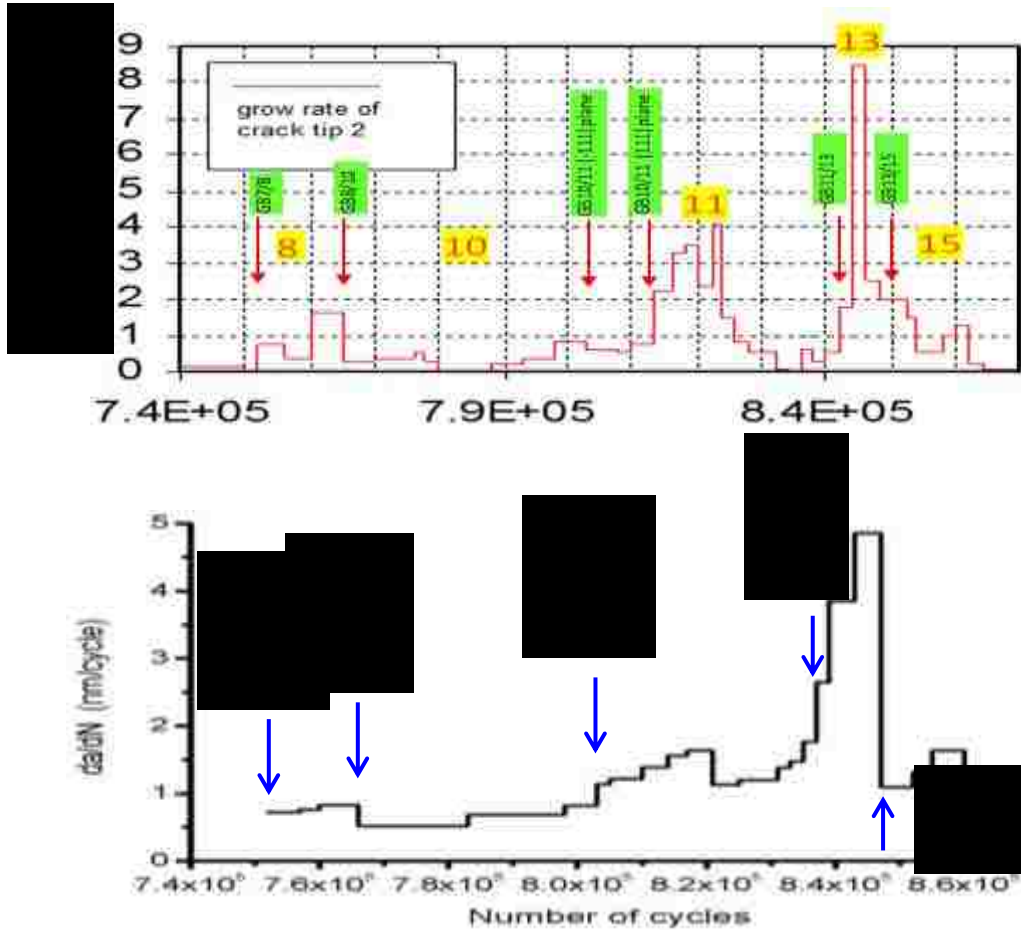
Figure 5.10 Experimentally measured growth rate curve of crack tip 2 vs. the simulated results.

Table 5.1   Parameters used in baseline simulation

Parameter	Value	Parameter	Value
R_f	1 (MPa√m)	D	25 (μm)
n	2.5	C	1.89×10^{-8} (m/cycle)
α_0	15 (°)	m	2.73
σ	150 MPa	R	0

Table 5.2   Parameters used in simulation of Short Crack in Al-Li alloy 8090

Parameter	Value	Parameter	Value
R_f	1.5 (MPa√m)	D	65 (μm)
n	3.5	C	1.43×10^{-10} (m/cycle)
α_0	10 (°)	m	2.08
σ	246 MPa	R	0.1

Table 5.3 α and corresponding R at GBs in the microstructure

GB	α (°)	R (MPa$\sqrt{m}$)
GB1/1'	10	0.948
GB1/2	14.6	1.489
GB2/3	0	0
GB3/5	2.5	0.004
GB5/6	2	0.002
GB6/7	2	0.002
GB7/8	1.7	~0.001
GB 8/10	7.4	0.369
GB10/11	0.7	~0
GB11/13	6.5	0.227
GB13/15	16.2	1.500

Chapter 6 Application of Short Crack Growth Model on Statistical Prediction of Short Crack Growth in Engineering Alloys and Texture Optimization in Alloy Design

In previous chapters, a microstructure-based model was proposed to quantitatively describe the behavior of short fatigue crack growth through GBs; and was validated with the experimental results. In this chapter, the model was used to statistically predict the crack growth in engineering alloys with different textures, showing its potential applications in life assessment and design of engineering alloys. It was demonstrated that the model could identify the optimum texture combination which provided the highest resistance against the short fatigue crack growth, showing its potential value in engineering alloy design in terms of texture optimization and grain boundary engineering.

6.1 Introduction

In short crack growth regime, fatigue cracks tend to follow particular crystallographic planes within individual grains, especially in planar slip alloys which either have high stacking fault energy or are precipitation hardened. These fatigue cracks are usually deflected at GBs, and such crack plane deflection results in higher resistance against the crack propagation across the GBs. In the past few decades, many experiments and modeling work have been carried out in attempts to quantitatively describe the short fatigue crack growth through grains. One of the representative numerical models was Navarro and de los Rios' (NR) dislocation blocking model which was based on BSC theory [117,118,121,122]. This model was later modified by Wilkinson, and used to study the effect of macro-texture on short fatigue crack growth in extruded Al-Li alloy [123]. However, the NR models are 2-D in nature. They yield a increase in growth rate immediately after the crack tip passes a GB, which contradicts to the experimental observations that crack growth may not necessarily accelerate after the crack passes a GB. As a derivative of BSC-based model, a model based on dislocation piling-up, dealing

with the discrete nature of the short crack growth, was proposed by Bjerken [179-182]. However, this model fails to take into account the local texture effect on crack path deflection. Finite element methods, especially crystal plasticity based approach, were also utilized to quantify the plastic strain in front of crack tip and crack advancement [125-128], but they are limited by the computation capability of computers. They are, therefore, unsuitable, even impractical, for statistically studying short fatigue crack growth behaviors. Based on the discovery that twist component of crack plane deflection at GBs is the key factor controlling crack path and resistance against crack growth [95, 101,174], a 3-D microstructure-based quantitative model was developed to describe the behavior of short fatigue crack growth through GBs [106,143]. Previous chapters have discussed the details of the model and its validation. This model takes into account the GB resistance, which is mainly caused by α at a GB, in simulation of short crack growth. Because α is controlled by the texture in an alloy, the model can be used to study the effects of texture on the short crack growth. In other words, it can be used to evaluate the texture that could optimize the fatigue properties of an alloy. In this chapter, the model was employed to statistically predict lives of short fatigue crack growth in engineering alloys that have different textures, to demonstrate the potential values of this model in design of engineering alloys for optimum resistance against fatigue damage.

6.2 Simulation

An idealized alloy with a grain structure consisted of pancake-shaped (i.e., layered) grains, which were all 25-µm thick, was first constructed digitally in this work. The grains were assigned to such orientations that form six different texture combinations of five typical texture orientations, such as cube, Goss, brass, S, copper textures and R-cube, as listed in Table 6.1. The first texture combination was similar as a random texture, serving as a baseline situation. The other five mainly consisted of six texture orientations commonly occurring in Al alloys, such as cube, Goss, brass, S, copper textures and R-cube, but with different volume fractions. The crystal orientation of each grain (except

the one for crack-initiation) is randomly selected within 10° deviation around the six ideal orientations in Euler space under the constraint that the volume fractions of texture components were statistically consistent with those five chosen texture combinations as listed in Table 6.1. The crystal orientations of grains were assigned symmetrically with respect to the center of the grain structure. The combinations 2-6 were selected in an attempt to represent from a deformation-type texture to an annealing-type texture, allowing evaluation the effect of each texture component on the resistance to short crack growth in the alloy.

A semi-penny shaped micro-crack of 8 μm in radius is assumed to be initiated in the grain centered in the grain structure. It is normal to the L/loading axis on the free surface. Such a micro-crack is often observed to be initiated from a coarse particle in Al-Cu and Al-Zn alloys [142,174], or on the {001} plane that is perpendicular to the L axis in a cube or Goss oriented grain in an Al-Li alloy [87,183]. The crack path is then determined by the minimum α criterion, i.e., the twist angle, α, is the minimum one at each GB. The cyclic loading condition and parameters are same as those in Table 5.1 in Chapter 5. For each texture combination, the orientation assignment as mentioned above is conducted 100 times, and the crack growth for each assignment is subsequently calculated until the crack is 500 μm long. In each orientation assignment, the location of the crack initiation remains unchanged.

6.3 Results and Discussion

6.3.1 Short Fatigue Crack Growth

Figure 6.2 shows the simulated results about crack lengths against number of loading cycles in the 6 texture combinations, respectively. In the plot for each texture combination, the black line represents the crack length on sample surface, averaged over 1000 times of simulation of crack growth, and the two blue dash lines are the corresponding standard deviation. These results illustrate that the texture has a profound

influence on the resistance to short fatigue crack growth in polycrystalline alloys. Among the six texture combinations, the combination 1 has a medium lifetime for the crack to reach 500 μm long; whereas the lifetime increases with increase in volume fraction of recrystallization type texture components (cube and R-cube) in the alloy. Two extreme examples are the growth of cracks in combinations 2 and 6 which are typical rolling-type and recrystallization-type textures respectively. On average, when the crack in combination 2 (completely consisting of deformation type texture components) reaches 500 μm long, the crack in combination 6 (almost fully consisting of recrystallized grains) is only about 250 μm long. Combination 2 shows the shortest lifetime (3.9×10^4 cycles) among all the 6 combinations, whereas combination 6 provides the longest lifetime (4.8×10^4 cycles). It is noteworthy to mention that the lifetime has a relatively wide deviation in each texture combination. The lifetime variations reach as high as 18%~30% of the average total life. This means that, even for the same alloy, the short fatigue crack life can be still significantly scattering. Also, the level of such deviation varies with texture combinations, suggesting that the life distribution for the crack to reach 500 um is influenced by the texture as well. These topics will be discussed in details in the following section.

6.3.2 Life Distribution of Short Fatigue Cracks

Life distribution of short fatigue cracks, represented by the number of loading cycles for crack to reach 500 μm, is plotted in Figure 6.3. It is evident that the life distribution varies with the texture combination, namely, texture has a marked effect on short fatigue crack growth behaviors. In addition, the life to reach 500 μm exhibits a characteristic bimodal distribution, namely, one peak appearing around 3.65×10^4 cycles (referred as the left peak in this thesis) and the other around 5.2×10^4 cycles (referred as the right peak in this thesis) in the life distribution plots of all the texture combinations, with combination 2 showing only the left peak (Figure 6.3). As shown in Figure 6.3, texture combination 6,

which contains the highest fraction of recrystallization texture, shows a ~12% probability of a short crack life within 3.5×10^4~3.75×10^4 cycles and 75% probability in the range of 5.0×10^4~5.8×10^4 cycles. With decrease in recrystallization type texture and increase in deformation type (from combination 6 to 1) in the alloy, the right peak is lowered and the left peak is enhanced gradually. In combination 3, the right peak almost disappears, whereas the short crack life exhibits a cut-off point at 5×10^4 cycles. Combination 1, due to its random texture, shows a typical bimodal distribution of short crack life.

6.3.3 Statistics of GB Resistance

The bimodal life distribution of short fatigue cracks indicates that, even if the samples are from the same batch of an alloy product and under the same loading condition, a short crack growth could likely to have one of the two characteristic lives, equivalent to the left and right peaks, as mentioned above. In order to understand why the bimodal distribution was formed, the growth behaviors of the cracks associated with the two characteristic peaks in texture combination 1 were statistically investigated. Since the GB-resistance is the main obstacle against the short crack growth, the GB-resistance along the path of those cracks associated with the two peaks is expected to account for the occurrence of the bimodal distribution of the short-fatigue life. In the analysis, the crystal orientations of the grains interacted with those cracks that have lives either $<3.8 \times 10^4$ cycles (i.e., at the short life end) or $>5.2 \times 10^4$ cycles (i.e., at the long life end) were statistically analyzed. With regard to each of the two peaks, the average α at each GB that the crack propagates through, together with the corresponding standard deviation, was analyzed, as listed in Table 6.2 and also plotted in Figure 6.4. It can be seen that there is a marked difference in α at the first GB between the short and long life cracks. α at the first GB is on average 5.8° for the short life and 34.6° for the longer life. At the 2nd to the 10th GBs, the average values of α are very close to each other, ranging from 11.5° to 18.8°, irrelevant to which peak the crack is associated with. As experimentally observed and discussed earlier   in

Chapter 4, the first few GBs, especially the very first GB, is critical for short fatigue crack growth, because the driving force of the crack at this early stage is very small thus the GB-resistance dominates the growth behaviors of the short crack.

The resistance from the 1st GB can significantly retard the crack growth and prolong the total short crack life. To demonstrate this effect, the evolution of the crack fronts associated with the short and long lives were simulated, respectively. In the simulation, α angles at GBs were assigned to be the average α as listed in Table 6.2 for short and long life cases, respectively, with the other parameters been kept the same as those used in simulating crack. Figure 6.5 shows the crack front evolutions simulated with regard to short and long lives respectively, in which the interval between two neighboring lines is 1000 cycles. The crack with a longer life (Figure 6.5(a)) spent a longer time at the first GB, as the density of crack front lines inside the 1st pair of GBs, in contrast to that in the case of short life (Figure 6.5(b)). The crack with a longer life spends much more time ($\sim 2 \times 10^4$ loading cycles) at the very first GB where α is large, 34.6° on average, than that with a shorter life. Moreover, the final profile of the longer life crack is shallower (with maximum depth of ~170 μm) and more flat-shaped than that of the shorter life (with maximum depth of ~199 μm). This is because that the resistance of the 1st GBs in grain structure R is very large, so that they pull the crack front back during the crack propagation. The resistance of the 2nd pair of GBs in grain structure L is slightly larger than that in grain structure R, causing relatively narrowly spaced crack profile at the GBs in grain structure L. However, the crack does not spend too much longer time at these GBs, because the difference in GB-resistance is not substantial. After passing the first two pairs of GBs, the GB-resistance in two grain structures are similar, thus the spacing of crack profiles in two grain structure become at the same magnitude, i.e. the lives (loading cycles) spent on crack growth after the 2nd pair of GBs until the crack being 500 μm long are similar in two grain structure. In summary, the crack retardation by the 1st pair of GBs significantly prolongs the short crack life. The formation of the bimodal life

distribution is probably account for by that a large portion of cracks encounter the high-resistance GBs at the very beginning of the growth, while many others grow through a path with relatively low-resistance at the beginning.

In order to understand why average crack lives vary among six texture combinations, the α of the first three pairs of GBs were statistically analyzed. As plotted in Figure 6.6 is the average α at the first three GBs vs. texture combination. The α of the 1st GB increases with the fraction of recrystallization type texture, although the α of the 2nd and 3rd GBs rise with recrystallization type texture and peak when it reaches 40%, followed by a decrease afterwards. The trend of α at the first GB though the six combinations is consistent with the short fatigue crack life, suggesting the significant effect of the first GB on the short fatigue crack life.

The results above demonstrate that the texture significantly influence the short fatigue crack growth in engineering alloys. The higher the fraction of recrystallization type texture in the alloy, the more probably the short crack will be severely retarded at the very beginning of the growth, leading to a prolonged fatigue life. The proposed model is capable not only able to predict the average life for short fatigue crack growth, but also estimate the boundaries of the fatigue life variation, which is of potential merit in engineering design. The results also suggest that a moderate high fraction of recrystallized grains in an alloy is beneficial to reduce the short fatigue crack growth rate, thus improve the fatigue limit of the alloy. This shows that the model can also identify the texture combinations that maximize the resistance to short fatigue crack growth in an engineering alloy. With the optimized texture combination as obtained from the simulation, the grain boundaries engineering [184,185] could be implemented through thermomechanical processing of an engineering alloy, to achieve the desired textures for the maximum resistance against fatigue damage.

These results demonstrate that the 3-D model developed in this work is able to predict the life of short fatigue crack growth from an initial size to a size that is equivalent to a long

crack in different textures in planar slip alloys. Meanwhile, the model can also be used for texture design by identifying the combination of textures that optimizes the resistance to short fatigue crack growth in an alloy. However, other factors, such as size and geometry of grains, grain size-grain orientation correlation, tilt angle and Schmidt factor, effect of texture on crack initiation and monotonic tensile properties, may need to be incorporated into the model, in addition to the twist angle. This will allow the study of the growth behaviors of a specific short fatigue crack in more complicated grain structure, statistical prediction of the average lifetime in engineering alloys, and alloy design in terms of optimization of grain size and geometry, and texture in the alloys. Also the values of the coefficients in the model need to be refined with experimental measurements which would be the future work for this technique.

6.4 Conclusion

The 3-D microstructurally based quantitative model was used to simulate the short fatigue crack growth in engineering alloys with different textures. The results showed that the alloy consisting of more recrystallized grains has more resistance against the short fatigue crack growth. This is because that in such as grain structure, the crack is more probable to encounter a high-resistance GB at the very beginning of the crack growth, which prolong the lifetime for the short fatigue crack growth. The model shows potential application in short fatigue crack life prediction and engineering alloy design by identifying the optimum texture and grain structure that possess the maximum resistance to crack growth.

Table 6.1 Volume fraction of texture components

TC	Volume fraction of components							Representing for
	Cube	Goss	Brass	S	Copper	R-cube	Random	
1	--	--	--	--	--	--	100%	random orientation
2	--	45%	45%	5%	5%	--	--	α- fiber
3	10%	10%	30%	25%	25%	--	--	β-fiber + weak recrystallization
4	30%	10%	30%	10%	10%	10%	--	β-fiber + recrystallization
5	40%	10%	10%	10%	10%	20%	--	weak β-fiber + recrystallization
6	50%	5%	5%	5%	5%	30%	--	recrystallization

- TC represents Texture Combination.

Table 6.2 Average α and standard deviation at GBs

GB	Short life crack		Long life crack	
	Average α (˚)	STDV	Average α (˚)	STDV
1	5.8	3.4	34.6	3.4
2	16.0	10.6	12.4	7.6
3	15.8	11.5	16.0	9.9
4	16.2	10.7	18.0	9.2
5	11.6	10.5	14.8	9.4
6	16.1	11.0	13.7	9.5
7	13.1	10.3	12.7	10.4
8	13.9	11.0	15.6	8.3
9	13.2	10.3	13.7	9.6
10	11.2	8.4	18.8	9.4
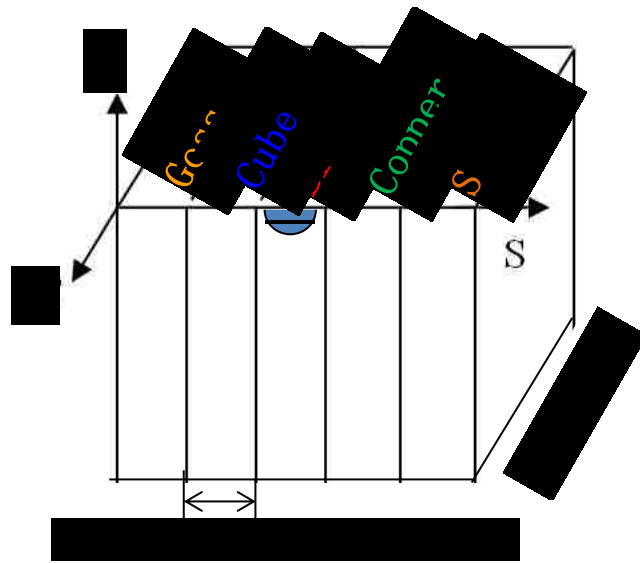
Figure 6.1 Sketch of grain structure used in the simulation.
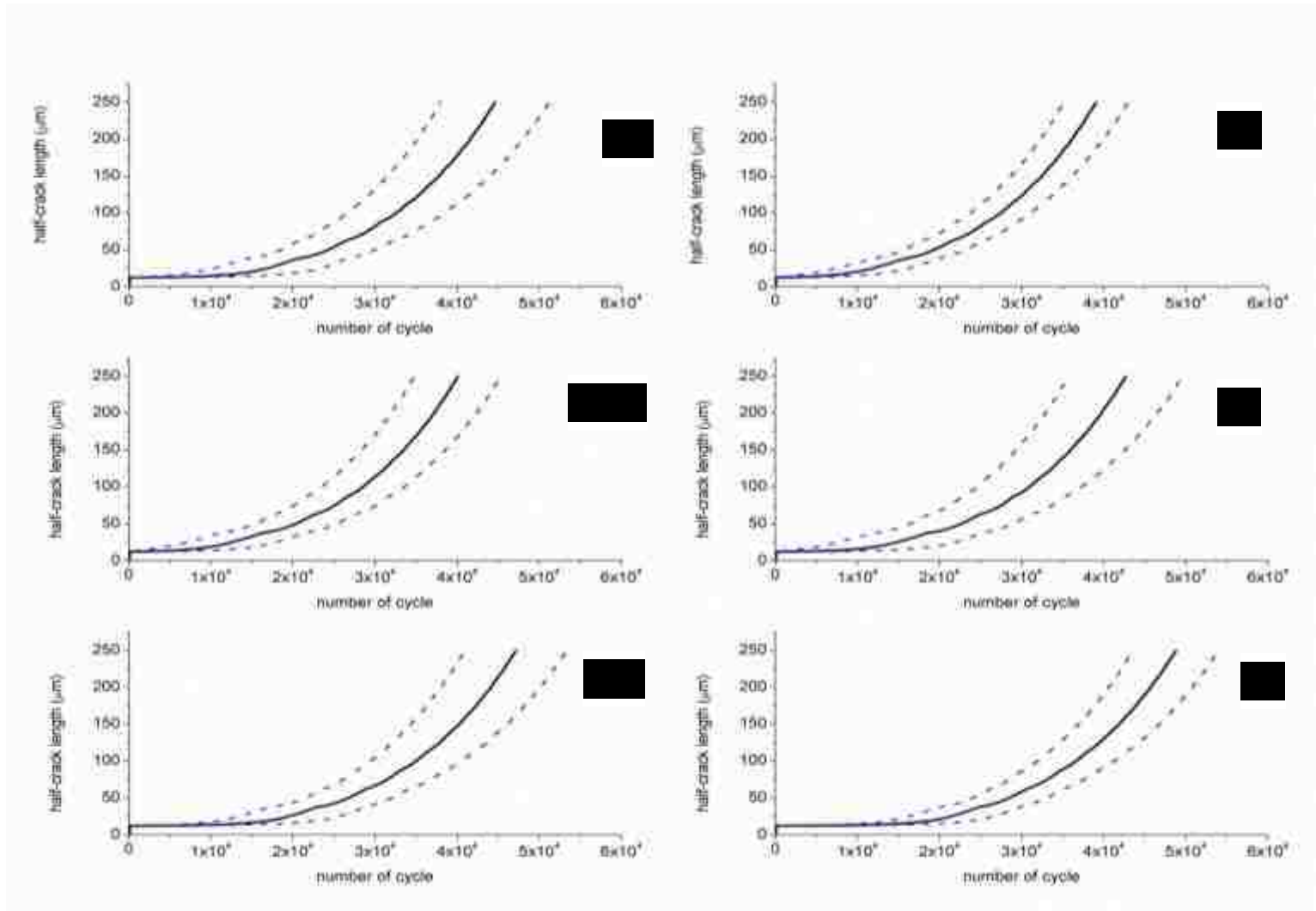
Figure 6.2 Simulated surface crack half-length vs. number of cycles for six texture combinations.
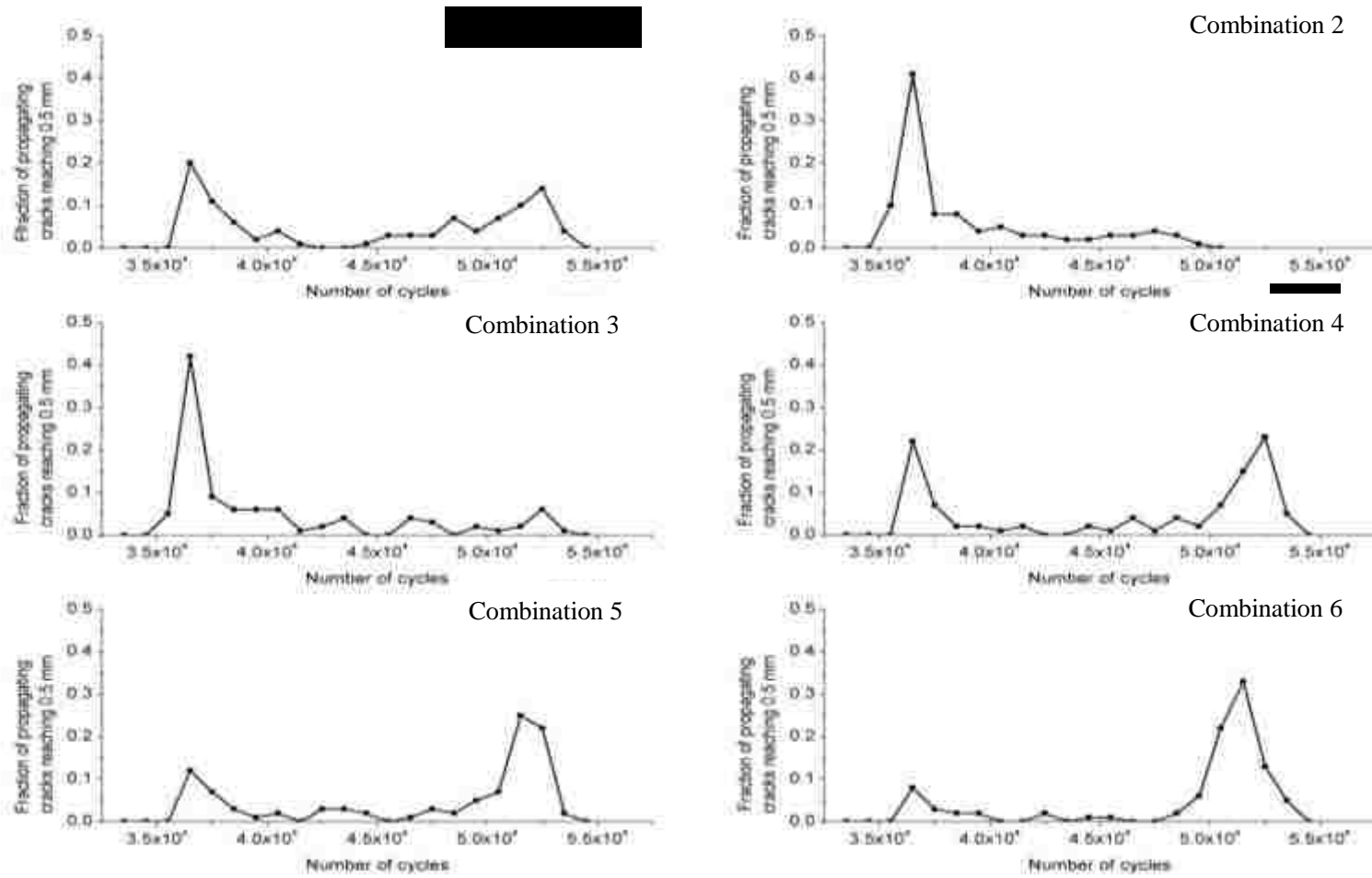
Figure 6.3 Life distribution of short crack propagation in six texture combinations.
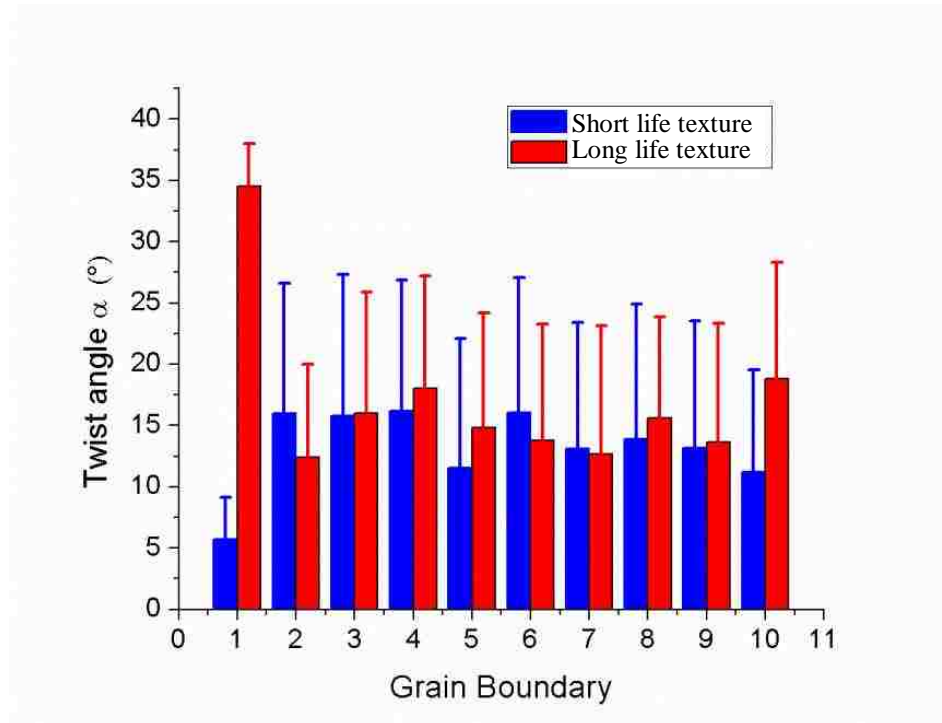
Figure 6.4 Statistics of α at each GB in texture combination 1.

(a)

(b)
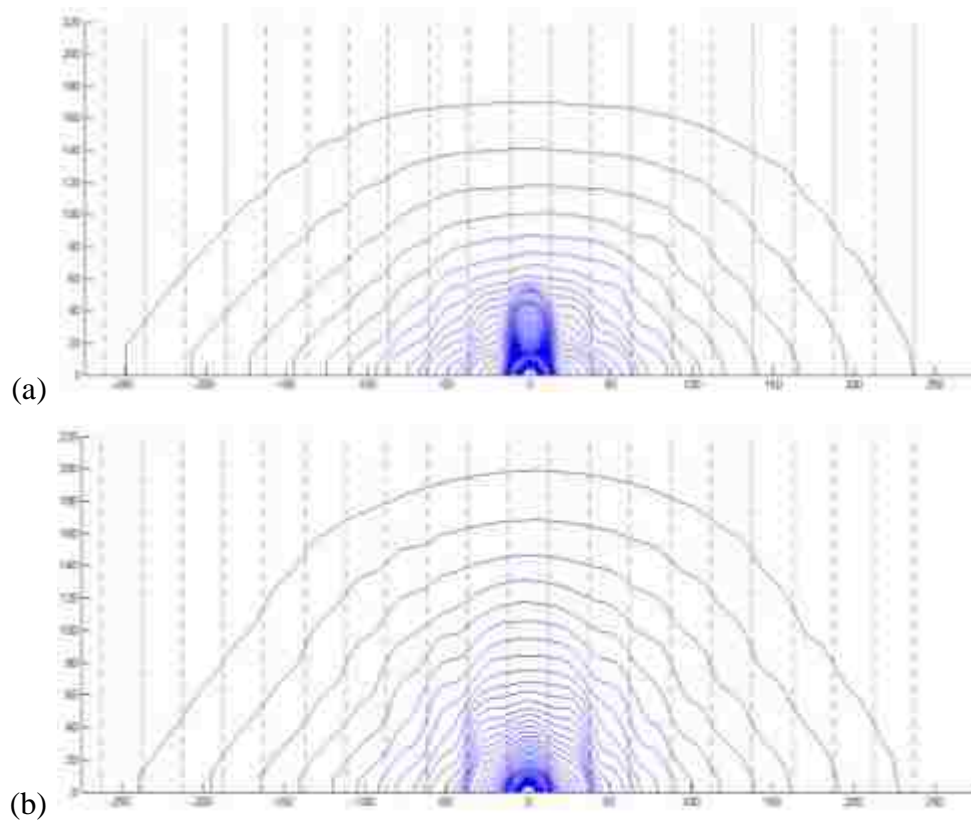
Figure 6.5 Crack front evolution associated with (a) long life and (b) short life.
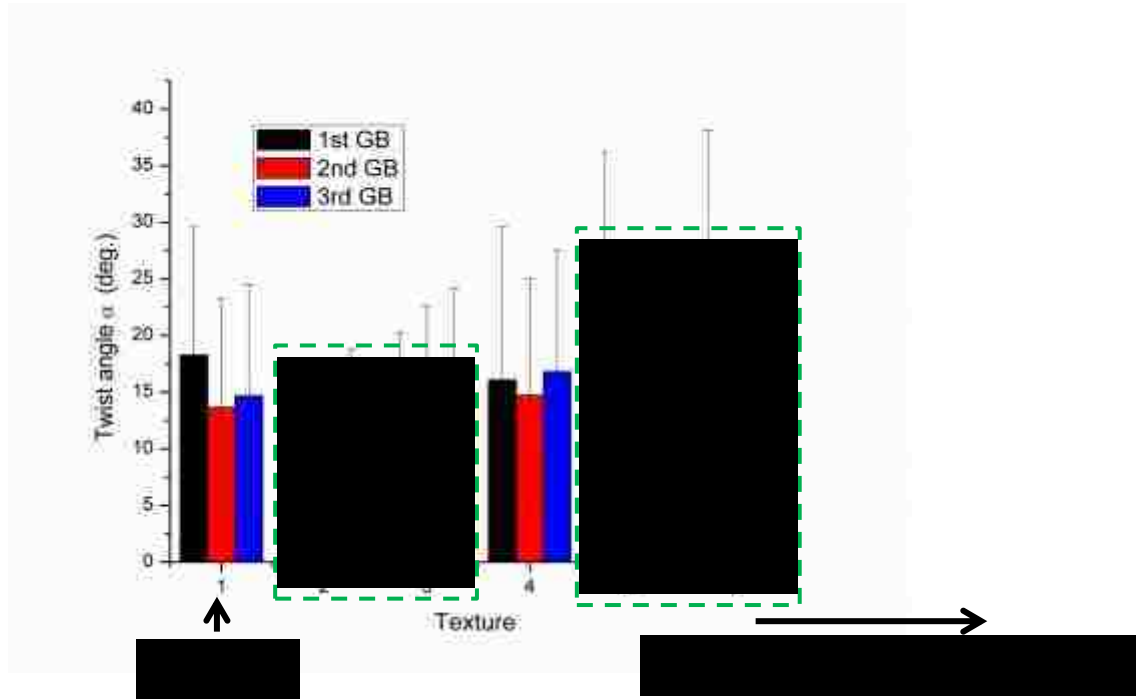
Figure 6.6 Statistics of α at first three pairs of GBs in six texture combinations.

Chapter 7 A 3-D Understanding of Fatigue Crack Initiation at Constituent Particle in High Strength Al Alloys

A part of the ultimate goal of this research work was to develop a microstructure-based quantitative model for more reliable life prediction of engineering alloys. It is expected to cover the crack initiation regime and short fatigue crack regime. The latter has been experimentally investigated and numerically modeled in previous chapters. The present chapter initializes a preliminary study on fatigue crack initiation behavior at constituent particles in high strength Al alloys, from a 3-D perspective with the aid of dedicated FIB and EBSD techniques. The newly discovered 3-D mechanism of the fatigue crack initiation may provide a clearer understanding for improving existing models of fatigue crack initiation.

7.1 Introduction

Al-Cu alloys, due to their high specific strength, are widely used for load frame applications in aerospace industry [186]. In these applications, accurate life prediction of the Al-Cu alloy components becomes critical for both the safety and weight savings of aircrafts. Since the early stage of fatigue damage (including crack initiation and growth of short fatigue crack) takes 50~90% of the total fatigue life [1, 125], the behaviors of crack initiation and early growth need to be thoroughly and quantitatively understood in these alloys. In Al alloys, such as 2000 and 7000 series, the fatigue cracks are often initiated at Fe-containing constituent particles (β-phase, Al_7Cu_2Fe). Due to the brittleness of these particles, some of them could be fractured under cyclic loading, leading to initiation of micro-cracks which may subsequently turn into long cracks. The behavior of fatigue crack initiation at the β-phase particles has been studied for decades. Most of these studies, however, mainly focused on the effects of particle size, aspect ratio and density as measured on the sample surface on the crack initiation behaviors [73, 74, 129, 187, 188]. Little work has been done on the effects of 3-D geometry of the particles and

micro-texture on crack initiation in high strength Al alloys. It was traditionally believed that coarse particles are prone to initiate critical cracks because they could generate higher strain/stress concentration under loading [129]. With the aid of EBSD, the effects of the crystal orientation of the particle's parent grain have recently been studied on fracture of the particles and subsequently on crack propagation from these fractured particles into the matrix using a finite element method in Al alloys AA7075-T651 [73, 74]. The recent establishment of the focus ion beam (FIB) technique makes it possible to reveal 3-D geometry of a particle of interest in alloys. With FIB, Weiland et al. [78] made an attempt to study how the crack initiation was influenced by the synergies of particle size, 3-D geometry and availability of slip system in the matrix adjacent to the particle. However, no concrete understanding was obtained in this work, due to the lack of systematical experiments and analysis in depth so far. In the present work, fatigue crack initiation and early growth at constituent particles were studied in an Al alloy AA2024-T3 using FIB and EBSD. It was revealed that the 3-D geometry of the particles and local texture were the key factors controlling fatigue crack initiation and early growth from these particles.

7.2 Experiments

The Al-Cu alloy AA2024-T351 used in this work was in the form of sheet, 7 mm thick. The chemical composition of the alloy is shown in Table 1.1. The average grain size was about $361 \times 97 \times 37$ μm^3. Samples ($36 \times 10 \times 4.6$ mm^3) for four point bend fatigue were cut with the plane under the tension loading being parallel to the L-T plane (L-the rolling direction and T-the transverse direction) and the loading axis being along the rolling direction. The sample surface under the maximum tensile stress in four-point bend was ground and mechanically polished before the fatigue tests which were conducted using a self-aligning four-point bend rig [145] under a constant maximum stress (342 MPa), equivalent to 90% the yield stress (380 MPa), at frequency of 20 Hz, stress ratio R=0.1 and room temperature in air. The fatigue strength of the alloy in the L direction was

between 266~285 MPa. After a sample failed, namely, the maximum sample deflection exceeded a critical value, the cracks initiated at particles on the surface were studied with an optical microscope and SEM. The length (dimension in L direction), width (dimension in T direction) and area of the cracked particles were also measured. The crystal orientations of the corresponding parent grains of 41 cracked particles were measured with an Oxford Instrument EBSD system. Subsequently, 20 of these particles were serial cross-sectioned in a dual beam SEM/FIB system, FEI Quanta 200 3D, to reveal the 3D geometry of the particles underneath the sample surface. The thickness of these particles, referred to as the distance between the sample surface and the deepest point along the particle contour beneath the surface, and their surface area were measured.

7.3 Results and Discussion

Multiple crack initiation was observed in each of the fatigued samples. As shown in Figure 7.1 (a-c), three types of fatigue cracks initiated at the β-phase particles were found in this alloy. Type-I cracks were those which could never extend into the matrix (Figure 7.1(a)). These cracks might be formed either during fatigue test or hot rolling. Type-II cracks were those that could just propagate into the matrix before fully arrested (Figure 7.1(b)). Type-III cracks could successfully grow into the matrix and became long cracks (Figure 7.1(c)). Only the particles which were associated with these type-III cracks could be detrimental to the material integrity. As shown in Figure 7.2(a), the surface areas of the particles initiating type-I, II and III cracks ranged from 40~382 μm^2, 61~202 μm^2 and 10~340 μm^2, respectively, indicating that there was no statistical correlation between particle area and crack initiation in this alloy. The critical cracks were not necessarily initiated from the large particles on the surface, and they could also be nucleated from those particles with smaller surface areas. This does not support the earlier studies [129, 188] which reported that only large Fe-containing constituent particles (as measured on the sample surface) could contribute to the nucleation of critical fatigue cracks in Al-Cu

alloys. There must be other factors that controlled fatigue crack initiation and early growth from particles on the surface in high strength Al alloys.

Recently, the stresses inside particles have been analyzed as a function of particle aspect ratio using FEA simulation [73, 74], indicating that higher internal stress can be generated inside the particles with a larger aspect ratio (length/thickness ratio, L/S) under cyclic loading. In other words, these particles are prone to fracture. However, as plotted in Figure 7.2(b), the type-III particles did not appear to possess larger aspect ratios, unlike those type-I particles which mostly had relatively larger aspect ratios (Figure 7.2(b)). This might mean that the particles with a large aspect ratio could hardly result in long cracks, though they were prone to fracture, and that the 3-D geometry of particles needs to be considered in order to understand the crack initiation and early growth behaviors at particles.

About 6-7 particles from each type were cross-sectioned using FIB in this work. Figs. 1(d-f) show the cross-sections of the typical type-I, -II and –III particles, respectively. The measured thickness of all these particles using the FIB technique were also plotted against the surface area and aspect ratio of the particles in Figure 7.2(a) and (b), respectively. It was found that the type-I particles studied were usually thin in the S direction, less than 3 μm thick, while the type-III particles were thicker, usually greater than 5 μm. The type-II particles were in the range of 3~5 μm in thickness. As shown in Figure 7.2(a), although the area of all cracked particles studied varied from 10 μm^2 to 382 μm^2, they could generally be grouped into three types in thickness, i.e., type-I: 0~3 μm, type-II: 3~5 μm and type-III: >5 μm, respectively. Similarly, the plot of aspect ratio vs. particle thickness in Figure 7.2(b) also revealed the same three groups of particles with only one exception of a type-I particle which fell into the 3-5 μm thick category instead of 0~3 μm one. These results implied that the particle thickness was an important factor controlling fatigue crack initiation and early growth at particles. Only the fractured

thicker particles could become detrimental to the fatigue properties of the alloy, since they were more likely to result in long cracks.

This might be understood by considering the driving force for crack growth from the fractured particles. The driving force increases with the crack size, i.e. the size of the fractured area in the particle. Due to the brittleness of the β-phase particles, the initial micro-crack from such a particle should just be in the shape of the cross-section of the particle, i.e., it is vertical to the load direction and through the whole cross section of the particle in the first few cycles [74]. The driving force for the micro-crack growth should be related to the thickness of the particle, rather than its surface length, just similar as the case of a through-notch where the stress intensity factor, K, is associated with the notch depth (i.e., particle thickness). Therefore, the driving force, ΔK, of the micro-crack inside the particle could be estimated using the equation (Equation 7.1) for quantifying the driving force for a semi-circular surface crack in an infinite matrix [189],

$$\Delta K = \frac{2}{\pi}\sigma_a\sqrt{\pi a}\left(1.211 - 0.186\sqrt{\sin\theta}\right) \qquad (7.1)$$

where a is the particle thickness; σ_a the far-field applied stress amplitude, and θ the angle between the sample surface and the radius from the crack center to an arbitrary point along the crack front (in this work, θ was assigned to 90˚ to calculate ΔK at the bottom of the crack). ΔK of all the particles studied in this work was then calculated, and the average value for type-I was 0.30 MPa√m (standard deviation (stdv) =0.09 MPa√m), type-II 0.42 MPa√m (stdv=0.04 MPa√m) and type-III 0.58 MPa√m (stdv=0.12 MPa√m). Indeed, the driving force for the type-III cracks was twice that for the type-I cracks. This could explain why the fractured type-III particles were more likely to be developed into long cracks, because of the higher driving forces for the micro-cracks in the particles.

Combined with FIB, EBSD was also used to analyze the 3-D geometry of micro-crack deflection across the particle/matrix interface, in order to understand the reason why most of the cracks initiated at type-I and II particles were fully arrested either at the particle/matrix interface or soon after the crack propagated into the matrix in this alloy. Figure 7.3 is an example of a particle associated with a mixed type I and II crack in a single grain. The micro-crack tip 1 (on side A) propagated into matrix for only about 5 μm and became non-propagating; whereas the tip 2 (on side B) was arrested at the particle/matrix interface. The crystal orientation of the parent grain of the particle in Figure 7.3(a) was measured with EBSD (Figure 7.3 (c)) to have Euler angles of φ_1=168.15˚, Φ=44.84˚ and φ_2=2.28˚. The trace of the crack plane of tip 1 matched that of slip plane $(1\bar{1}\bar{1})$ on the surface in the grain. From the cross-section of the particle by FIB (Figure 7.3 (d), the side face of the particle on side B was revealed to be straight and tilted by about -60˚. On side A, the side face was almost vertical to the sample surface (Figure 7.3(d)). Assuming that the micro-crack was perpendicular to the load axis (i.e., L direction) inside the particle, and that the crack deflection at the particle/matrix interface followed the minimum twist criterion which requires the crack to follow the slip plane that forms the minimum twist angle with the crack plane across a grain boundary or particle/matrix interface [95], the twist angle, α, of the two crack planes across the grain boundary presents a major resistance to crack growth across the boundary [95, 106, 143]. The larger the twist, the higher the resistance will be to crack growth across the boundary. α on the both sides of the particle in Figure 7.3(a) was then calculated by α=arccos([E]×[N$_1$]•[E]×[N$_2$]) [95], where [E], [N$_1$] and [N$_2$] are the unit vectors of the normals of the particle/matrix interface plane, crack plane in the particle and the favorite slip plane for crack growth in the matrix [95, 143].

The effect of interface tilting on α was also quantified, as shown in Figure 7.3(e)). It can be seen in Figure 7.3(e) that all the slip planes present large twist angles α

($\alpha_{(1\bar{1}\bar{1})} = 41.3°, \alpha_{(\bar{1}11)} = 26.4°, \alpha_{(111)} = 61.2°$ and $\alpha_{(11\bar{1})} = 45.4°$) , when the interface is tilted by -60˚, like the case on side B of the particle in Figure 7.3(d). When the interface is vertical to the sample surface, i.e., its tile =0°, just as side A of the particle, slip plane $(11\bar{1})$ and $(1\bar{1}\bar{1})$ offer very small twist angles ($\alpha_{(11\bar{1})} = 2.0°$, $\alpha_{(1\bar{1}\bar{1})} = 1.1°$) while (111) and ($\bar{1}$11) provide large twist angles ($\alpha_{(111)} = 26.7°, \alpha_{(\bar{1}11)} = 23.6°$). As suggested in the previous work [106, 143] that the resistance to crack growth is a Weibull function of α, large α results in high resistance to crack growth across the particle/matrix interface. As a result, the arrest of the micro-crack at the particle/matrix interface on side B of the particle in Figure 7.3(d) could well be attributed to the large twist angles associated with all the slip planes, because the resistance due to the large twist might well exceed the driving force for crack growth across the interface. In the case of side A of the particle, since slip plane crack could propagate onto either plane $(1\bar{1}\bar{1})$ or $(11\bar{1})$ in the matrix, as they both could offer very small twist, i.e., low resistance, for crack growth at the interface. Since the Schmidt factor of plane $(1\bar{1}\bar{1})$ (m=0.455) was slightly higher than that of $(11\bar{1})$ (m=0.442), the crack actually propagated onto $(1\bar{1}\bar{1})$ in the matrix on side A, as revealed by matching the crack line to the trace of plane $(1\bar{1}\bar{1})$ on the sample surface. Therefore, the crack was able to propagate into the matrix on side A, because of the low resistance from slip plane $(1\bar{1}\bar{1})$. As the crack grew further down on side A, it encountered the bottom side of the particle. Since the bottom interface plane was either tilted in the range between -45˚ and -60˚, or between 30˚ and 45˚, the crack front had to be twisted by an angle between 26° and 36°, in order to pass the interface at the bottom. This could present a high enough resistance to arrest the crack on side A, as shown in Figure 7.3(b). In other words, the crack became non-propagating on side A, due to the driving force being smaller than the resistance at the bottom interface of the particle. This crystallographic model for short fatigue crack growth, supported also by the

work from other researchers [107, 112], has recently been used to explain crack retardation at grain boundaries [106, 143]. More quantitative results about the behaviors of micro-crack growth across the particle/matrix interface in this alloy will be discussed in more details in a separate paper.

7.4 Summary

With the aid of EBSD and FIB, the thickness of the fractured Fe-containing particle was found to be a dominant factor, rather than particle area and aspect ratio measured on sample surface, that controlled the growth behaviors of the micro-crack initiated from the particle in Al-Cu alloys. The resistance due to crack plane twist at the particle/matrix interface, which was influenced by crystal orientation of parent grain and particle 3-D geometry, could significantly retard and even arrest crack growth at the interface.
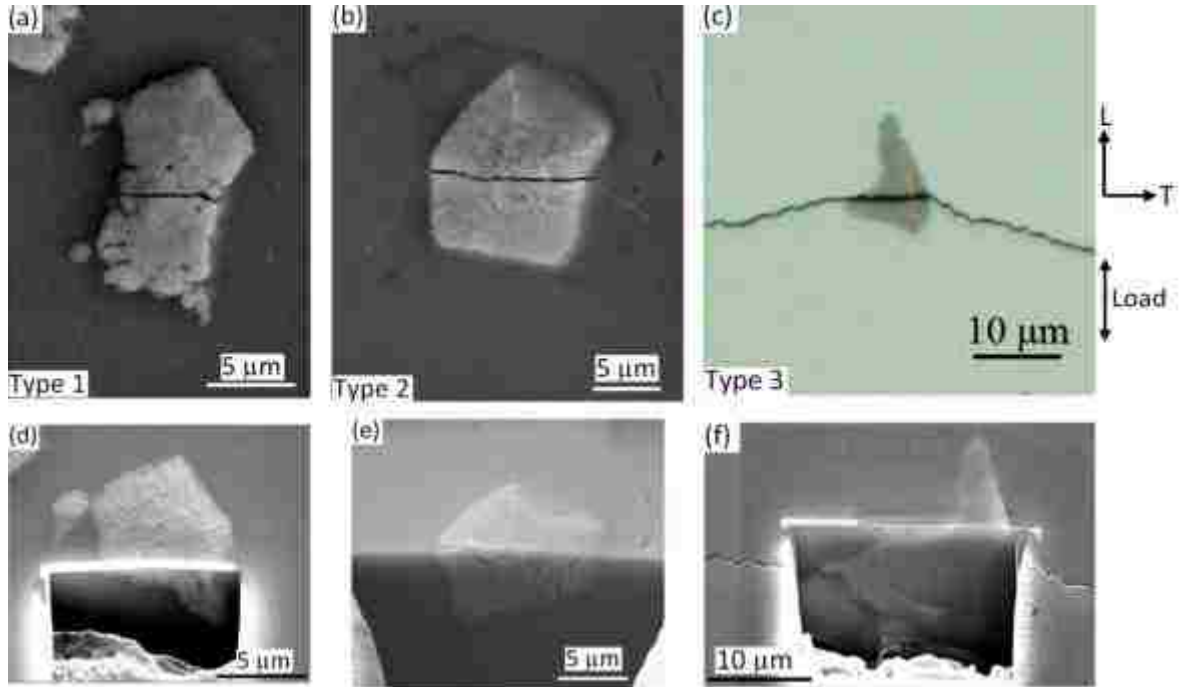
Figure 7.1 Fatigue cracks initiated from particles: (a) a type-I crack, (b) a type-II crack, (c) a type-III crack. (d-f) cross-sections of the particles in (a), (b) and (c), respectively.
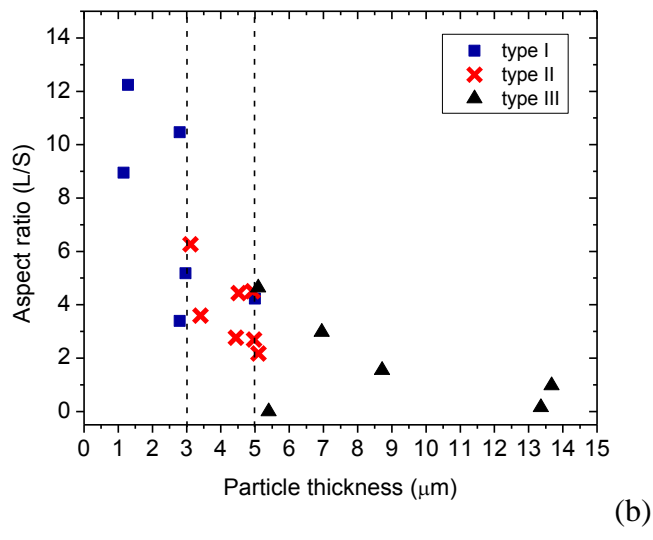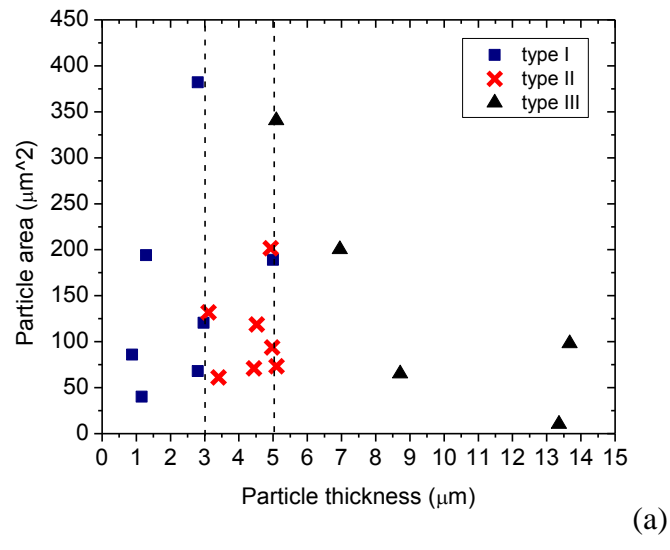
Figure 7.2 (a) The area of the fractured particles as measured on the surface and (b) the aspect ratios (L/S) of the particles are plotted against particle thickness.
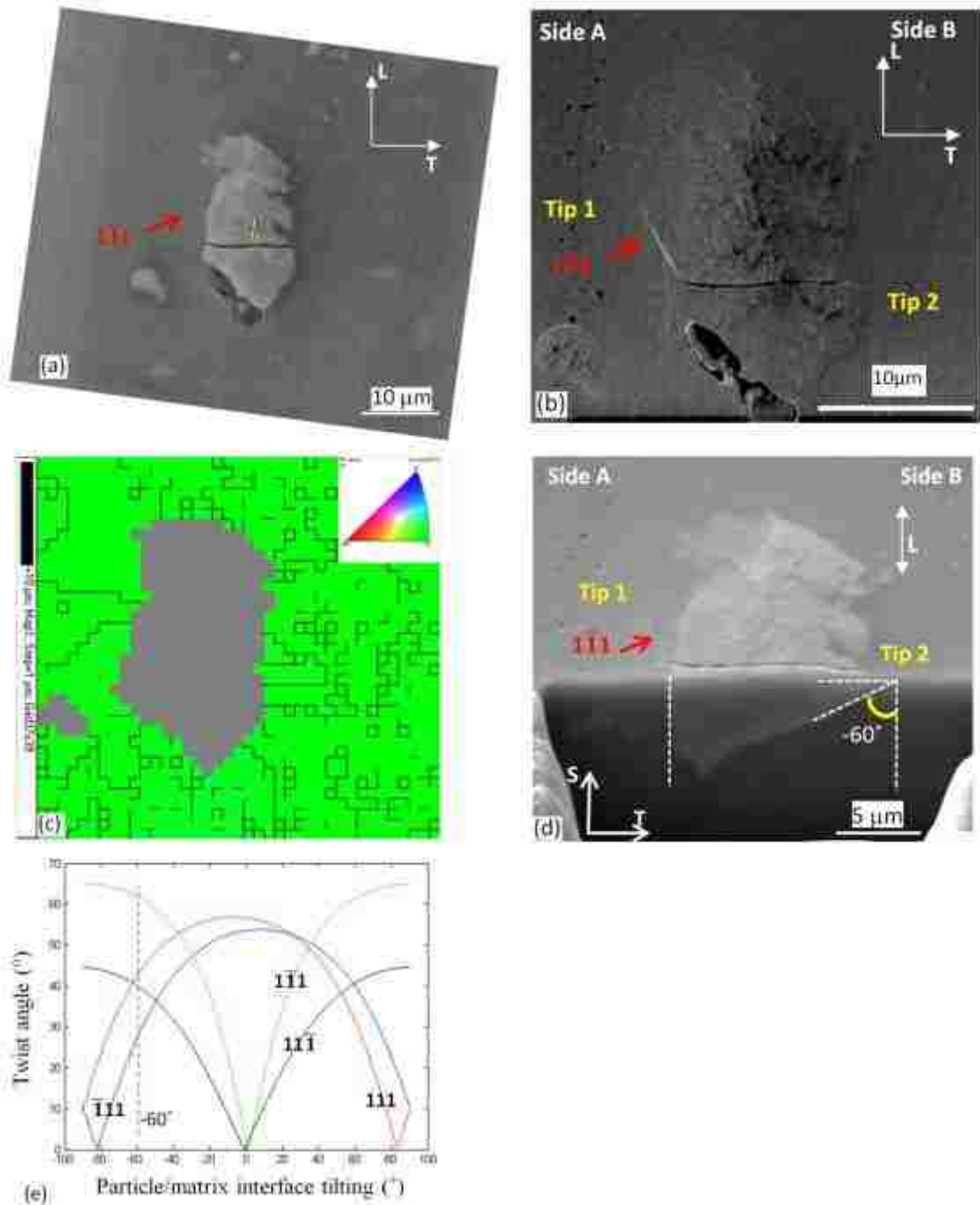
Figure 7.3 A mixed type (types-I and II) crack initiated from a particle was imaged in a dual beam SEM/FIB using (a) SEM mode and (b) ion beam imaging mode in which the short crack is more evident in the matrix. (c) Inverse pole figure with respect to the rolling plane normal; (d) cross-section of the particle by FIB; and (e) calculated twist angles for {111} planes as a function of the tilt of particle/matrix interface.

155

Chapter 8 Conclusions

8.1 Concluding remarks

The early stage of fatigue damage in precipitation hardened high strength Aluminum alloys, such as Al-Li alloy AA8090 and Al-Cu alloy AA2024, were studied in the present research work. It was mainly focused on the effects of microstructure and texture on short fatigue crack initiation and growth, since these effects are far from being well and quantitatively understood, but significant in both application and design of these materials. The crack growth deflection at GBs, the effect of GB titling on crack plane twist, and the resistance of GB against short crack growth were experimentally quantified, followed by the development of a microstructurally-based 3-D model in an attempt to predict and simulate the short crack growth through grains in planar slip engineering alloys. The simulation results about the crack growth rate on surface yielded a good agreement with the experimentally measured ones, validating the capability of the model. The model also showed potential applications in prediction of the crack length vs. loading cycles in textured alloys and alloy design. The behaviors of extension of micro-cracks from constituent particles into the surrounding matrix were also experimentally investigated with a 3-D perspective, offering a new understanding of the mechanism for crack initiation in high strength Al alloys. The main conclusions about the present research work are drawn as follows:

1. The fatigue cracks in an AA8090 alloy were initiated along (001) planes being closely vertical to the loading axis. The short cracks propagated crystallographically along a slip plane within each grain and deflected at the GBs that the cracks interacted with (i.e., the crack plane being twisted and tilted at each GB). This further confirmed Zhai's criterion that a short fatigue crack propagated onto the slip plane that had the minimum twist at the GB, since the crack plane twist presented a resistance (GB-resistance) against the short crack growth, retarding crack growth at GBs. The GB-resistance was qualitatively found to increase with α in the fatigue experiments of AA8090 alloy.

2. The grain geometry, i.e. tilting of GBs, showed a strong influence on the value of α at a GB and thus GB-resistance, because it affected α at the GB, in addition to the orientations of the two adjacent grains.

3. As the crack grew deeper, the effect of GB 3-D effect started to take place when the crack front encountered the secondary GBs being buried shallowly beneath the sample surface, which could effectively alter the crack path on the sample surface. The crack growth in the 8090 alloy obeyed the minimum-α criterion until about 20 grains long, beyond which the GB 3-D effect played more part in influencing the crack growth path.

4. The map of the minimum α for a vertical micro-crack to cross the first GB was calculated as a function of the orientation of the neighboring grain, to evaluate qualitatively the resistance to crack growth into the neighboring grain. It was found that Brass, S, Copper and Goss textures provided low resistance, while cube and R-cube textures showed high resistance to the crack growth. Such an α-map is of value for alloy design against fatigue damage by optimizing texture components in the alloys.

5. In the alloy AA2024-T351, the cracks were initiated from the artificially made micro-notches in the selected grains. The cracks were initiated only at notches in the "soft" orientated grains which had relatively high Schmid factors.

6. Retardation of short crack growth varied at different GBs due to the variation in resistance at the GBs.

7. An experimental method was developed to quantify the GB-resistance, by which the GB-resistance was found to increase with α, following a two-parameter Weibull function. By the method proposed in this study, the GB-resistance vs. α was experimentally quantified for the first time.

8. Based the established relation of GB-resistance with α, a 3-D model incorporating GB-resistance and effective driving force along the crack front in 3-D was

developed and a Matlab code was subsequently built to quantify the fatigue crack front evolution and crack tip growth in engineering alloys. The model demonstrated its capabilities in predicting the evolution of irregular crack front and the scattering crack growth rate, and was validated by the good agreement between the so-simulated and experimental results about the crack growth rate on surface in an AA8090 Al-Li alloy.

9. The model was used to statistically predict the short crack growth in Al alloys with different textures. The prediction results showed that, for the typical cracks initiated vertical to loading axis as in most high strength Al alloys, the grain structures with more volume fraction of recrystallization type textures had higher resistance against the short crack growth than the ones with more deformation type textures. The model showed the potential for practical use in more reliable life prediction and alloy design in terms of texture optimization.

10. As part of fatigue crack initiation, the extension of micro-cracks in Fe-containing particles into the surrounding matrix was preliminarily investigated in 3-D. The thickness of particle was found to be a dominant factor that controlled the growth behaviors of the micro-crack initiated from the particles in Al-Cu alloys, rather than the particle cross-section area and aspect ratio measured on sample surface, as conventionally believed. The resistance due to crack plane twist at the particle/matrix interface, which was influenced by crystal orientation of parent grain and particle 3-D geometry, could significantly retard and even arrest crack growth at the interface.

8.2 Suggestions for Future Work

With the recent development of characterization and modeling techniques, the early stage of fatigue crack growth has recently drawn increasing interests from materials scientist and engineers globally. Although highly intensive research has been performed, it is still a great challenge to fully and quantitatively understand the physical mechanisms for the

early stage fatigue behaviors, in order to perform reliable life prediction and development of new generation engineering alloys. Further research work still needs to be done to further reveal quantitative relationships between microstructure and fatigue damage, develop microstructure-based models and apply the models in life assessment and guidance for alloy development.

In particular, it would be desirable to (1) future verify the proposed method of GB-resistance quantification in other planar slip materials, (2) extend the method to determine GB resistance in non-planar slip materials, with necessary modifications on crack propagation mechanism and modeling, (3) further improve the 3-D short crack growth as proposed in the present work , for example, by incorporating it with commercial crystal plasticity FEM software, (4) further expand the model to fulfill a full-scale life prediction, by covering statistical prediction of micro-crack incubation rate at constituent particles in texture grain structure, probability of micro-crack extension into matrix, short crack growth in grains structure with different grain geometry and orientation, and transition to long fatigue crack region.

References

[1]   S.Suresh, Fatigue of Materials, 2nd ed., Cambridge University Press, Cambridge, 2001.

[2]   V.V. Bolotin, Mechanics of fatigue, CRC Press, Boca Raton, 1999.

[3]   G.H. Koch, M. P.H., Brongers, N.G. Thompson, in. 'Corrosion Costs and Preventive Strategies in the United States,' Report FHWA-RD-01-156

[4]   R.L. Norton, Machine Design: An Integrated Approach, Prentice-Hall, Upper Saddle River, New Jersey. , 2000.

[5]   Internet source http://www.g2mtlabs.com/2011/06/nace-cost-of-corrosion-study-update/

[6]   J. Schijve, Materials Science, 39 (2003) 307-332.

[7]   A. Wöhler, Zeitschrift für Bauwesen, 10 (1860) 160-161.

[8]   S. Suresh, R.O. Ritchie, International Metals Reviews, 29 (1984) 445-476.

[9]   J.A. Ewing, J.C.W. Humfrey, Phil. Trans. Roy. Soc., A200 (1903) 241-250.

[10]   G.R. Irwin, J.   Appl. Mech., 24 (1957) 361-364.

[11]   P.C. Paris, M.P. Gomez, a.W.P. Anderson, The Trend in Engineering, 13 (1961) 9-14.

[12]   W. Elber, Eng. Fract. Mech., 2 (1970) 37-45.

[13]   W. Elber, The significance of fatigue crack closure., in: American Society for Testing and Materials, Philadelphia, 1971.

[14]   P.C. Paris, R.J. Bucci, E.T. Wessel, in: Stress Analysis and Grwoth of Cracks, Special Technial Publication 513, Philadelphia:Amercan Society for Testing and Materials 1972, pp. 141-176.

[15]   D.A. Ryder, S.P. Lynch, in: The Influence of Environments on Fatigue, London: The Institue of Mechanical Engineers, 1977, pp. 21-26.

[16]   H. Nowack, K.H. Trautmann, K. Schulte, G. Lutjering, in: Fracture Mechanics, Special Technical Publication 677, Philagelphia: Amercan Society for Testing and Materials, 1979.

[17]   N. Pugno, M. Ciavarella, P. Cornetti, A. Carpinteri, Journal of the Mechanics and Physics of Solids, 54 (2006) 1333-1349.

[18] G. Maymon, International Journal of Fatigue, 27 (2005) 629-638.

[19] D. Kujawski, F. Ellyin, Fatigue & Fracture of Engineering Materials & Structures, 16 (1993) 743-752.

[20] D. Kujawski, International Journal of Fatigue, 23 (2001) S239-S246.

[21] S. Stoychev, D. Kujawski, International Journal of Fatigue, 27 (2005) 1425-1431.

[22] K. Sadananda, S. Sarkar, D. Kujawski, A.K. Vasudevan, International Journal of Fatigue, 31 (2009) 1648-1659.

[23] D. Kujawski, International Journal of Fatigue, 23 (2001) 733-740.

[24] S. Pearson, Eng. Fract. Mech., 7 (1975) 235-247.

[25] A.S.f.T.a. Materials, in: ASTM Standards E466-E468, Philadelphia.

[26] J. Schijve, Fatigue of Structures and Materials, Kluwer Academic Publisher, Dordrecht, the Netherlands, 2001.

[27] P.J.E. Forsyth, Proceedings of the Royal Society of London Series a-Mathematical and Physical Sciences, 242 (1957) 198-&.

[28] C.S. Barrett, Structure of Metals (Crystallographic methods, principles and data), McGRAW-Hill book

company, Inc. , New York, 1952.

[29] H. Mughrabi, R. Wang, K. Differt, U. Essmann, Fatigue Mechanisms, ASTM, Philadelphia, 1983.

[30] U. Essmann, U. Gosele, H. Mughrabi, Philosophical Magazine a-Physics of Condensed Matter Structure Defects and Mechanical Properties, 44 (1981) 405-426.

[31] C. Scheerder, in, Delft University of Technology, 1992.

[32] K.K. Sankaran, R. Perez, K.V. Jata, Advanced Materials & Processes, 158 (2000) 53-54.

[33] A. Hunsche, P. Neumann, Acta Metallurgica, 34 (1986) 207-217.

[34] W.A. Wood, Philosophical Magazine a-Physics of Condensed Matter Structure Defects and Mechanical Properties, 3 (1958) 692-699.

[35] P.J.E. Forsyth, Nature, 171 (1953) 172-173.

[36] A.S. Cheng, C. Laird, Materials Science and Engineering, 51 (1981) 111-121.

[37] D. Sigler, M.C. Montpetit, W.L. Haworth, Metallurgical Transactions a-Physical Metallurgy and Materials Science, 14 (1983) 931-938.

[38] W.L. Haworth, A.F. Hieber, R.K. Mueller, Metall. Trans. A, 8(A) (1977) 1597-1604.

[39] B.L. Boyce, J.R. Michael, P.G. Kotula, Acta Materialia, 52 (2004) 1609-1619.

[40] C. Laird, J.M. Finney, D. Kuhlmannwilsdorf, Materials Science and Engineering, 50 (1981) 127-136.

[41] C.Y. Kung, M.E. Fine, Metallurgical Transactions a-Physical Metallurgy and Materials Science, 10 (1979) 603-610.

[42] B.T. Ma, C. Laird, Acta Metallurgica, 37 (1989) 325-336.

[43] S.E. Axter, W.B. Jones, D.H. Polonis, Metallography, 8 (1975).

[44] E.A. Debartolo, B.M. Hillberry, Int. J. Fatigue, 20 (1998) 727-735.

[45] I. Sinclair, P.J. Gregson, in: ICAA-6, Toyohashi, Japan, 1998.

[46] T.S. Srivatsan, D. Kolar, P. Magnusen, Materials and Design, 23 (2002) 129-139.

[47] A.V.d. Forest, J. of Applied Mechanics, 3 (1936) A23-25.

[48] P.C. Paris, F. Erdogan, J. Basic Engng, 85 (1963) 528-534.

[49] C. Kaynak, A. Ankara, Engineering Fracture Mechanics, 43 (1992) 769-778.

[50] R.P. Gangloff, R.S. Piascik, D.L. Dicus, J.C. Newman, Journal of Aircraft, 31 (1994) 720-729.

[51] R.O. Ritchie, Int. Met. Rev., 24 (1979) 205-230.

[52] H.H. Johnson, P.C. Paris, Eng. Fract. Mech., 1 (1968) 3.

[53] F. Soniak, L. Remy, The Behavior of Short Fatigue Cracks, Mechanical Engineering Publications, London, 1986.

[54] W.L. Morris, M.R. James, O. Buck, Eng. Fract. Mech., 18 (1983) 871-877.

[55] D. Taylor, J.F. Knott, Fatigue Eng. Mater. Struct., 4 (1981) 147.

[56] C.W. Brown, M.A. Hicks, Fatigue of Engineering Materials and Structures, 6 (1983) 67-76.

[57] D. Taylor, Computational Materials Science, 25 (2002) 228-236.

[58] S.J. Hudak, J. Eng. Mater. Technol. (Trans ASME H), 103 (1981) 26-35.

[59] M.H.E. Haddad, T.H. Topper, B. Mukherjee, J. Test. Eval., (1981) 65-81.

[60] J.C. Newman, P.R. Edwards, in, Neuilly sur Seine, France, 1988, pp. 104.

[61] P.J.E. Forsyth, in: Proc. of Crack Propagation Symposium, The College of Aeronautics, Cranfield, UK, pp. 76-94.

[62] S. Gungor, L. Edwards, Materials Science and Engineering a-Structural Materials Properties

Microstructure and Processing, 160 (1993) 17-24.

[63] W.L. Morris, Metallurgical Transactions a-Physical Metallurgy and Materials Science, 11 (1980) 1117-1123.

[64] W.L. Morris, Metall. A., 11A (1980) 1117.

[65] K.J. Miller, Proceedings of the Institution of Mechanical Engineers Part C-Journal of Mechanical Engineering Science, 205 (1991) 291-304.

[66] R.R. Suresh S, Int Met Rev, 29 (1984) 5.

[67] C. Blochwitz, R. Richter, Materials Science and Engineering a-Structural Materials Properties Microstructure and Processing, 267 (1999) 120-129.

[68] J.C. Newman, Fatigue & Fracture of Engineering Materials & Structures, 17 (1994) 429-439.

[69] K.S. Ravichandran, J.M. Larsen, Metallurgical and Materials Transactions a-Physical Metallurgy and Materials Science, 28 (1997) 157-169.

[70] S.T. Taira, K.; Hoshina, M. , in: Symp on Fatigue Mech, ASTM, Philadelphia, Pa, Kansas City, MO, USA, 1979, pp. 135-173.

[71] J.C.W.V.D. Kasteele, D. Broek, Eng. Fract. Mech., 9 (1977) 625-635.

[72] C.B. Fuller, A.R. Krause, D.C. Dunand, D.N. Seidman, Mater. Sci. Eng., A338 (2002) 8-16.

[73] J.D. Hochhalter, D.J. Littlewood, R.J. Christ, M.G. Veilleux, J.E. Bozek, A.R. Ingraffea, A.M. Maniatty, Modelling and Simulation in Materials Science and Engineering, 18 (2010).

[74] J.E. Bozek, J.D. Hochhalter, M.G. Veilleux, M. Liu, G. Heber, S.D. Sintay, A.D. Rollett, D.J. Littlewood, A.M. Maniatty, H. Weiland, R.J. Christ, J. Payne, G. Welsh, D.G. Harlow, P.A. Wawrzynek, A.R. Ingraffea, Modelling and Simulation in Materials Science and Engineering, 16 (2008).

[75] J.N. Goodier, J. Appl. Mech. Trans. ASME, 55 (1933) 39-44.

[76] G. Patton, C. Rinaldi, Y. Bréchet, G. Lormand, R. Fougères, Mater. Sci. Eng., A254 (1998) 207-218.

[77] P. Lamagnère, D. Girodin, P. meynaud, F. vergne, A. Vincent, Mater. Sci. Eng., A215 (1996) 134-142.

[78] H. Weiland, J. Nardiello, S. Zaefferer, S. Cheong, J. Papazian, D. Raabe, Engineering Fracture Mechanics, 76 (2009) 709-714.

[79] U. Zerbst, M. Madia, D. Hellmann, Engineering Fracture Mechanics, 82 (2012) 115-134.

[80] B.J. Connolly, J.R. Scully, Corrosion, 61 (2005) 1145-1166.

[81] R. Sunder, W.J. Porter, N. E. Ashbaugh, Fatigue Fract. Engng. Mater. Struct., 25 (2002) 1015-1024.

[82] Z.Q. Xu, W. Wen, T.G. Zhai, Metallurgical and Materials Transactions a-Physical Metallurgy and Materials Science, 43A (2012) 2763-2770.

[83] P. Mulvihill, C.J. Beevers, Mechanical Engineering Publications, eds. K. J. Miller and E. R. de los Rios, (1986) 203-213.

[84] H.C. Burghard, Metall. Trans. A, 5 (1974) 2083-2094.

[85] F. Sarioğlu, F.Ő. Orhaner, Mater. Sci. Eng., A248 (1998) 115-119.

[86] A.K. Vasudevan, R.D. Doherty, Acta Materialia, 35 (1987) 1193-1219.

[87] C.J. Taylor, T. Zhai, A.J. Wilkinson, J.W. Martin, Journal of Microscopy-Oxford, 195 (1999) 239-247.

[88] M. Mineur, P. Villechaise, J. Mendez, Mater. Sci. Eng., A286 (2000) 257-268.

[89] M.D. Sangid, H. Sehitoglu, H.J. Maier, T. Niendorf, Materials Science and Engineering a-Structural Materials Properties Microstructure and Processing, 527 (2010) 7115-7125.

[90]   M.D. Sangid, H.J. Maier, H. Sehitoglu, International Journal of Plasticity, 27 (2011) 801-821.

[91]   M.D. Sangid, H.J. Maier, H. Sehitoglu, Acta Materialia, 59 (2011) 328-341.

[92]   M.D. Sangid, G.J. Pataky, H. Sehitoglu, R.G. Rateick, T. Niendorf, H.J. Maier, Acta Materialia, 59 (2011) 7340-7355.

[93] K.S. Chan, International Journal of Fatigue, 32 (2010) 1428-1447.

[94] J. Lankford, Fatigue of Engineering Materials and Structures, 5 (1982) 233-248.

[95] T. Zhai, A.J. Wilkinson, J.W. Martin, Acta Materialia, 48 (2000) 4917-4927.

[96] R.N. Wilson, R.W. Gardiner, D.M. Turley, Mech E Conference Publications (Institution of Mechanical Engineers), 2 (1986) 407-416.

[97] J. Polak, P. Liskutin, V. Ocenasek, K. Sperlink, Materials Science Forum, 217 (1996) 1429-1434.

[98] A. Plumtree, S. Schäfer, The Behavior of Short Fatigue Cracks, Mechanical

Engineering Publications, eds. K. J. Miller and E. R. de los Rios, (1986) 215-217.

[99] A.K. Zurek, M.R. James, W.L. Morris, Metallurgical Transactions a-Physical Metallurgy and Materials Science, 14 (1983) 1697-1705.

[100] Z.Q. Zheng, B. Cai, T. Zhai, S.C. Li, Materials Science and Engineering a-Structural Materials Properties Microstructure and Processing, 528 (2011) 2017-2022.

[101] T. Zhai, A.J. Wilkinson, J.W. Martin, The effects of micro-texture and beta ' particle distribution on short fatigue crack growth in an Al-Li 8090 alloy, in: E.A. Starke, T.H. Sanders, W.A. Cassada (Eds.) Aluminium Alloys: Their Physical and Mechanical Properties, Pts 1-3, Trans Tech Publications Ltd, Zurich-Uetikon, 2000, pp. 1549-1554.

[102] Y. Takahashi, T. Shikama, S. Yoshihara, T. Aiura, H. Noguchi, Acta Materialia, 60 (2012) 2554-2567.

[103] X.J. Wu, W. Wallace, M.D. Raizenne, A.K. Koul, Metallurgical and Materials Transactions a-Physical Metallurgy and Materials Science, 25 (1994) 575-588.

[104] K.S. Chan, J. Lankford, Scripta Metallurgica, 17 (1983) 529-532.

[105] W. Wen, T. Zhai, Philosophical Magazine, (2011).

[106] W. Wen, T.G. Zhai, Metallurgical and Materials Transactions a-Physical Metallurgy and Materials Science, 43A (2012) 2743-2752.

[107] W. Schaef, M. Marx, H. Vehoff, A. Heckl, P. Randelzhofer, Acta Materialia, 59 (2011) 1849-1861.

[108] W. Schaef, M. Marx, Acta Materialia, 60 (2012) 2425-2436.

[109] C. Holzapfel, W. Schaf, M. Marx, H. Vehoff, F. Mucklich, Scripta Materialia, 56 (2007) 697-700.

[110] W. Ludwig, J.Y. Buffiere, S. Savelli, P. Cloetens, Acta Materialia, 51 (2003) 585-598.

[111] A. King, W. Ludwig, M. Herbig, J.Y. Buffiere, A.A. Khan, N. Stevens, T.J. Marrow, Acta Materialia, 59 (2011) 6761-6771.

[112] M. Herbig, A. King, P. Reischig, H. Proudhon, E.M. Lauridsen, J. Marrow, J.Y. Buffiere, W. Ludwig, Acta Materialia, 59 (2011) 590-601.

[113] D. Catoor, K.S. Kumar, Philosophical Magazine, 88 (2008) 1437-1460.

[114] W. Wen, A.A. Luo, T. Zhai, Y. Jin, Y.-T. Cheng, I. Hoffmann, Scripta Materialia, (2012) In press.

[115] J.L. Gimple, D.S. Wilkinson, J.D. Embury, J.J. Lewandowski, Aluminum 2001- Proc. of the TMS 2001, Aluminum Automotive and Joining sessions, eds, S. K. Das, J.

G. Kaufman and T. J. Lienert, TMS (2001).

[116] T. Shuji, T. Keisuke, N. Yoshikazu, Mech. Res. Commun, 5 (1978) 375.

[117] A. Navarro, E.R. Delosrios, Proceedings of the Royal Society of London Series a-Mathematical Physical and Engineering Sciences, 437 (1992) 375-390.

[118] E.R. Delosrios, A. Navarro, Philosophical Magazine a-Physics of Condensed Matter Structure Defects and Mechanical Properties, 61 (1990) 435-449.

[119] B.A. Bilby, A.H. Cottrell, K.H. Swinden, Proc. Roy. Soc., A272 (1963) 304.

[120] W.L. Morris, Metallurgical Transactions a-Physical Metallurgy and Materials Science, 10 (1979) 5-11.

[121] C. Vallellano, A. Navarro, F.J. Garcia-Lomas, J. Dominguez, Journal of Strain Analysis for Engineering Design, 43 (2008) 337-347.

[122] C. Vallellano, A. Navarro, J. Dominguez, Engineering Failure Analysis, 16 (2009) 2646-2657.

[123] A.J. Wilkinson, Philosophical Magazine a-Physics of Condensed Matter Structure Defects and Mechanical Properties, 81 (2001) 841-855.

[124] K.S. Ravichandran, X.D. Li, Acta Materialia, 48 (2000) 525-540.

[125] J.H. Fan, D.L. McDowell, M.F. Horstemeyer, K. Gall, Engineering Fracture Mechanics, 68 (2001) 1687-1706.

[126] M.F. Horstemeyer, N. Yang, K. Gall, D. McDowell, J. Fan, P. Gullett, Fatigue & Fracture of Engineering Materials & Structures, 25 (2002) 1045-1056.

[127] D.L. McDowell, Materials Science and Engineering a-Structural Materials Properties Microstructure and Processing, 468 (2007) 4-14.

[128] V.S. Deshpande, A. Needleman, E. Van der Giessen, Acta Materialia, 51 (2003) 1-15.

[129] A. Merati, International Journal of Fatigue, 27 (2005) 33-44.

[130] I.J. Polmear, MATERIALS FORUM 28 (2004) 1-14.

[131] B. Chalmers, Physical Metallurgy, John Wiley & Sons, Inc., New York, 1959.

[132] R.E. Reed-Hill, D. Van Nostrand Company, New York, 1973.

[133] R.W. Cahn, American Elsevier Publishing Company Inc., New York, 1970.

[134] R.E. Smallman, R.J. Bishop, Butterworth-Heinemann, Oxford, 1999.

[135] M. Tomura, T. Mori, T. Nakamura, Trans. Japan Inst. Metals, 14 (1973) 355.

[136] T.H. Sanders, E.A. Ludwiczak, R.R. Sawtell, Mater. Sci. Eng., 43 (1980) 247-260.

[137] M.J. Marcinkowski, R.M. Fisher, J. Appl. Phys., 31 (1960) 1303.

[138] K.T.V. Rao, R.O. Ritchie, Int. Materials Reviews, 37 (1992) 153-185.

[139] K.T.V. Rao, W. Yu, R.O. Ritchie, Metall. Trans. , 19A (1988) 549-561.

[140] A.K. Vasudévan, P.E. Bretz, A.C. Miller, S. Suresh, Mater. Sci. Eng., 64 (1984) 113-122.

[141] S. Suresh, A.K. Vasudévan, P.E. Bretz, Metall. Trans., 15A (1984) 369-379.

[142] W. Wen, A.H.W. Ngan, Y. Zhang, Materials Science and Engineering a-Structural Materials Properties Microstructure and Processing, 564 (2013) 97-101.

[143] W. Wen, T. Zhai, Philosophical Magazine, 91 (2011) 3557-3577.

[144] Annual book of ASTM standards 2000.

[145] T. Zhai, Y.G. Xu, J.W. Martin, A.J. Wilkinson, G.A.D. Briggs, International Journal of Fatigue, 21 (1999) 889-894.

[146] O. CW, N. WC, P. RFW, Adv Electronics Electron Phys, 21 (1965) 181-247.

[147] D. McMullan, Scanning, 17 (1995) 175-185.

[148] C.A. Volkert, A.M. Minor, Mrs Bulletin, 32 (2007) 389-395.

[149] L.A. Giannuzzi, F.A. Stevie, Micron, 30 (1999) 197-204.

[150] L. Bischoff, Nuclear Instruments & Methods in Physics Research Section B-Beam Interactions with Materials and Atoms, 266 (2008) 1846-1851.

[151] S. Reyntjens, R. Puers, Journal of Micromechanics and Microengineering, 11 (2001) 287-300.

[152] J. Gierak, Semiconductor Science and Technology, 24 (2009).

[153] O. Engler, V. Randle, Introduction to Texture Analysis Macrotexture, Microtexture, and Orientation Mapping, CRC Press, 2010.

[154] U.F. Kocks, C.N. Tomé, H.-R. Wenk, Texture and Anisotropy: Preferred Orientations in Polycrystals and Their Effect on Materials Properties, Cambridge University Press, London, 2000.

[155] J. Hansen, Pospiech, J., and Lücke, K.,, Tables for Texture Analysis of Cubic Crystals,, Springer-Verlag, Berlin, 1978.

[156] H.J. Bunge, Texture Analysis in Material Science, Butterworths, London, 1982.

[157] H.-J. Bunge, Z. Metallkd., 56 (1965) 872.

[158] H.-J. Bunge, Texture Analysis in Materials Science: Mathematical Methods Butterworths, London 1982.

[159] B.F. Decker, E.T. Asp, D. Harper, J., Appl. Phys., 19 (1948) 388.

[160] S. Kikuchi, J. Appl. Phys., 5 (1928) 83.

[161] D.J. Dingley, Baba-Kishi, K., and Randle, V., , An Atlas of Backscatter Kikuchi

Diffraction Patterns, Institute of Physics Publishing, Bristol 1994.

[162] G. Gottstein, O. Engler, J. de Physique IVColl., C7 3 (1993) 2137.

[163] P.D. Hobson, Fatigue of Engineering Materials and Structures, 5 (1982) 323-327.

[164] K. Hussain, Engineering Fracture Mechanics, 58 (1997) 327-354.

[165] M.R. James, Scripta Metallurgica, 21 (1987) 783-788.

[166] K.T.V. Rao, W. Yu, R.O. Ritchie, Metallurgical Transactions a-Physical Metallurgy and Materials Science, 19 (1988) 563-569.

[167] J.X. Li, T. Zhai, M.D. Garratt, G.H. Bray, Metallurgical and Materials Transactions a-Physical Metallurgy and Materials Science, 36A (2005) 2529-2539.

[168] D.N. Fager, M.V. Hyatt, H.T. Diep, Scripta Metallurgica, 20 (1986) 1159-1164.

[169] W.S. Miller, J. White, D.J. Lloyd, Journal De Physique, 48 (1987) 139-149.

[170] S.P. Lynch, B.C. Muddle, T. Pasang, Acta Materialia, 49 (2001) 2863-2874.

[171] A. Turnbull, E.R.D. Rios, Fatigue & Fracture of Engineering Materials & Structures, 18 (1995) 1355-1366.

[172] K. Tokaji, T. Ogawa, K. Ohya, International Journal of Fatigue, 16 (1994) 571-578.

[173] V. Gerold, H.P. Karnthaler, Acta Metallurgica, 37 (1989) 2177-2183.

[174] T. Zhai, X.P. Jiang, J.X. Li, M.D. Garratt, G.H. Bray, International Journal of Fatigue, 27 (2005) 1202-1209.

[175] F. Bergner, G. Zouhar, International Journal of Fatigue, 22 (2000) 229-239.

[176] W. Wen, T. Zhai, Acta Materialia, (2012, to be submitted).

[177] H.T. Pang, P.A.S. Reed, International Journal of Fatigue, 25 (2003) 1089-1099.

[178] X.J. Wu, W. Wallace, A.K. Koul, M.D. Raizenne, Metallurgical and Materials Transactions

165

a-Physical Metallurgy and Materials Science, 26 (1995) 2973-2982.

[179] C. Bjerken, S. Melin, International Journal of Solids and Structures, 46 (2009) 1196-1204.

[180] C. Bjerken, International Journal of Fatigue, 27 (2005) 21-32.

[181] C. Bjerken, S. Melin, Engineering Fracture Mechanics, 71 (2004) 2215-2227.

[182] C. Bjerken, S. Melin, International Journal of Fatigue, 25 (2003) 559-566.

[183] T.G. Zhai, A.J. Wilkinson, J.W. Martin, Orientation dependence of the high cycle fatigue properties in a hot-cross rolled Al-Li 8090 alloy plate, in: P.J. Gregson, S.J. Harris (Eds.) Aluminum Alloys 2002: Their Physical and Mechanical Properties Pts 1-3, 2002, pp. 1279-1284.

[184] T. Watanabe, Journal of Materials Science, 46 (2011) 4095-4115.

[185] G. Palumbo, E.M. Lehockey, P. Lin, Jom-Journal of the Minerals Metals & Materials Society, 50 (1998) 40-43.

[186] E.A. Starke, J.T. Staley, Progress in Aerospace Sciences, 32 (1996) 131-172.

[187] E.A. DeBartolo, B.M. Hillberry, International Journal of Fatigue, 23 (2001) S79-S86.

[188] M. Liao, Engineering Fracture Mechanics, 76 (2009) 668-680.

[189] D. Gross, T. Seelig, Fracture Mechanics with an Introduction to Micromechanics, Spinger, Verlag Berlin Heidelberg, 2006.

VITA

Place of Birth: Guiyang, Guizhou, China

Education:

- University of Kentucky, Lexington, Kentucky

  8/2008-present   Ph.D. candidate (Materials Science and Engineering)

- University of Science and Technology Beijing, Beijing, China

  8/2007-8/2008   Master program (Materials Science)

- University of Science and Technology Beijing, Beijing, China

  9/2001-7/2005   B.E. (Materials Science)

Employment:

- Materials Engineer, internship, Secat, Inc, Lexington, Kentucky, 11/2012-present

- Research Assistant, University of Kentucky, Lexington, Kentucky, 8/2008-11/2012

- Secretary, University of Science and Technology Beijing, Beijing, China, 7/2005-8/2007

Research:

- Fatigue behavior in Al alloys and modeling

- Mechanical and corrosion properties of Mg alloys

- Phase transformation dynamics and mechanical properties of low-alloying steels

Professional Service:

- Key Reader and Reviewer of *Metallurgical and Materials Transactions A*

- Reviewer of *Materials Science and Engineering A*, *Modern Physics Letters B*, S*urface Review and Letters*

Awards Received:

- Best Overall Award Poster of Distinction in Graduate Student Poster Competition, University of Kentucky, 9/2012

- Student Choice Award Poster of Distinction in Graduate Student Poster Competition, University of Kentucky, 9/2012

- Visiting Scientist Grant, The University of Hong Kong, 7/2011

- Outstanding Thesis and Graduate Award, 7/2005

Publications:

1. **W. Wen** and T. Zhai, "A Study of the Effects of Particle 3-D Geometry and Micro-texture on Fatigue Crack Initiation Behavior in an Aluminum Alloy 2024-T3 using FIB and EBSD", *Materials Science and Engineering-A*, vol. 564, pp.97-101, 2013.
2. **W. Wen**, A. Luo and T. Zhai, "Improvement of Mechanical and Corrosion Properties of Skin Layer in Mg-Al-Mn Alloy by Super Vacuum Die Casting", *Scripta Materialia*, 2012, pp. 879-882, 2012
3. **W. Wen** and T. Zhai, "A 3-D Quantitative Crystallographic Model for Fatigue Crack Propagation through Grain Boundaries in High Strength Al Alloys", *Metallurgical and Materials Transactions A*, vol. 43, pp. 2743-2752, 2012.
4. **W. Wen** and T. Zhai, "3-D Effects of Microstructures on Short Fatigue Crack Growth in an Al-Li 8090 Alloy", *Philosophical Magazine*, vol. 91, pp. 3557-3577, 2011.
5. Z. Xu, **W. Wen**, and T. Zhai, "Effects of Pore Position in Depth on Stress Concentration and Fatigue Crack Initiation", *Metallurgical and Materials Transactions A*, vol. 43, pp. 2763-2770, 2012.
6. X. Jiang, T. Zhai, J. Xu, Q, Zeng, **W. Wen**, "Misorientation Gradients by EBSD in Hot and Cold Deformed Alloys", *Microscopy and Microanalysis*, vol. 15, Supplement S2, 2009, pp. 1072-1073.
7. Y. Song, G. Liu, S. Wang, **W. Wen**, "Prediction and Experimental Verification of Phase Transformation Critical Temperature and Cooling Velocity of Low-Alloying Steel," *Proceedings of the National Academic Conference on Calculation, Simulation and Image Analysis in Materials Science*, Qinhuangdao, China, 2005
8. **W. Wen** and T. Zhai, "A FIB Study of the Resistance of Grain Boundaries to Short Fatigue Crack Propagation in Three-dimensions in High Strength Al Alloys", *Acta Materialia*, to be submitted.
9. Y. Liu, J. Jiang, X. Xue, Y. Wu, **W. Wen**, T. Zhai, "Corrosion Behavior of Die Cast AM60B Mg Alloy in a Complex Salt Solution", *Metallurgical and Materials Transactions A*, in preparation.
10. **W. Wen** and T. Zhai, "A Microstructurally Based Model of Crack Initiation at Second Phase Particles in High Strength Al Alloys", *Acta Materialia*, in preparation.

Conference Oral Presentations:

1. **W. Wen**, A. Ngan, and T. Zhai, "The Quantification of Resistance of Grain Boundaries to Short Fatigue Crack Propagation in Three-dimensions in High Strength Al Alloys," in *TMS 2013 Annual Meeting*, San Antonio, TX, 3/2013, (**invited**).
2. **W. Wen** and T. Zhai, "A FIB Study of the Resistance of Grain Boundaries to Short Fatigue Crack Propagation in Three-Dimensions in High Strength Al Alloys," in *TMS 2012 Annual Meeting*, Orlando, FL, 3/2012, (**invited**).
3. **W. Wen**, X. Zang, T. Zhai, Z. Xu, and A. Ngan, "Identification of Fatigue Crack Initiation from Surface Particles in High Strength Al Alloys," in *TMS 2013 Annual Meeting*, Orlando, FL, 3/2012, (**invited**).
4. **W. Wen** and T. Zhai, "A Three-dimensional Quantitative Crystallographic Model for Fatigue Crack Propagation through Grain Boundaries," in *TMS 2011 Annual Meeting*, San Diego, CA, 3/2011, (**invited**).
5. Z. Xu, **W. Wen**, and T. Zhai, "The Effect of Pore Position in Depth on Stress Field around the Pore on Sample Surface," in *TMS 2011 Annual Meeting*, San Diego, CA, 3/2011, (**invited**).
6. **W. Wen**, Y. Jin, A. Luo, and T. Zhai, "Improved Environmental Bending Fatigue Strength of Mg-Al-Mn Alloy by Super Vacuum Die Cast," in *TMS 2013 Annual Meeting*, San Antonio, TX, 3/2013.
7. L. Chen, **W. Wen**, Y. Han, H. Zhang, and T. Zhai, "A Study of Precipitates Formed during Homogenization in Modified AA6061 Aluminum Alloy," in *TMS 2013 Annual Meeting*, San Antonio, TX, 3/2013.
8. **W. Wen** and T. Zhai, "A Microstructure-Based Model for Simulation of Short Fatigue Crack Growth in 3-D," in *24th AeroMat Conference and Exposition*, Bellevue, WA, 4/2013.
9. Y. Jin, **W. Wen**, T. Zhai, "The Anisotropy of Fatigue Weaklink Density and Strength Distribution in an AA7075-T651 Al Alloy Plate," in *24th AeroMat Conference and Exposition*, Bellevue, WA, 4/2013.
10. T. Zhai, Y. Zhang, B. Xu, A. Ngan, Z. Xu, X. Zang, **W. Wen**, and L. Yang, "The Behaviors of Fatigue Crack Initiation in Metallic Materials," in *Materials Science & Technology 2012*, Pittsburgh, PA, 10/2012.
11. **W. Wen** and T. Zhai, "A 3-D Quantitative Crystallographic Model for Short Fatigue Crack Propagation through Grain Boundaries in High Strength Al Alloys," in *13th International Conference on Aluminum Alloys (ICAA13)*, Pittsburgh, PA, 6/2012.
12. T. Zhai, Q. Zeng, **W. Wen**, and X. Wen, "Formation of P ($\{011\}<566>$) and $\{113\}<110>$ Textures by Precipitation Pinning in Continuous Cast Al Alloys during Annealing," in *13th International Conference on Aluminum Alloys (ICAA13)*, Pittsburgh, PA, 6/2012.

13. **W. Wen**, A. Luo, and T. Zhai, "Fatigue and Corrosion Properties of Mg-Al-Mn Alloy by Super Vacuum Die Cast," in *TMS 2013 Annual Meeting*, Orlando, FL, 3/2012

14. **W. Wen** and T. Zhai, "A 3-D Quantitative Crystallographic Model for Short Fatigue Crack Propagation through Grain Boundaries in High Strength Al Alloys," in *Materials Science & Technology 2011*, Columbus, OH, 10/2011.

15. **W. Wen**, A. Luo, and T. Zhai, "Fatigue and Corrosion Properties of Mg-Al-Mn Alloy by Super Vacuum Die Cast," in *Materials Science & Technology 2011*, Columbus, OH, 10/2011.

16. T. Zhai and **W. Wen**, "Failure of a Surgical Rod," in *Materials Science & Technology 2011*, Columbus, OH, 10/2011.

17. X. Zang, **W. Wen**, A. Ngan, and T. Zhai, "Factors Controlling Fatigue Crack Initiation at Particles in High Strength Al Alloys," in *Materials Science & Technology 2011*, Columbus, OH, 10/2011.

18. **W. Wen** and T. Zhai, "Quantitative 3-D Crystallographic Model for Fatigue Crack Propagation in High Strength Al Alloys," in *1st World Congress on Integrated Computational Materials Engineering*, Seven Springs, PA, 7/2011.

19. X. Jiang. T.Zhai, J. Xu, Q, Zeng, **W. Wen**, "Misorientation Gradients by EBSD in Hot and Cold Deformed Alloys," in *Microsc Microanal*, Richmond, VA, 7/2009.

Wei Wen

5/01/2013